Czech Technical University in Prague

Faculty of Electrical Engineering
Department *of Measurement*

STRUCTURAL HEALTH MONITORING OF AEROSPACE COMPOSITE STRUCTURES USING ULTRASONIC GUIDED WAVES

Doctoral Thesis

Ing. Lenka Šedková

Prague, *June 2022*

Ph.D. Programme: (P 2612) Electrical Engineering and Information Technology
Branch of study: (3708V017) *Air Traffic Control*

Supervisor: *prof. Ing. Radislav Šmíd, Ph.D.*

Declaration of authorship

I hereby declare I have written this thesis independently and have quoted all the sources of information used in accordance with the methodological instructions on ethical principles for writing an academic thesis. Moreover, I state that this thesis has neither been submitted nor accepted for any other degree.

In Prague   …………………………………..

Acknowledgment

First, I would like to thank my supervisor, professor Radislav Šmíd for his professional guidance, support, and help. I am also thankful to my supervisor at VZLU Dr. Růžek, who enabled and supported my studies, and for sharing his experience and knowledge. Also, I would like to thank my colleague Ondřej Vích, who joined my Lamb-wave research with patience and passion.

My thanks belong to my family, especially to my parents who thought me that everything is possible and let me do whatever I wanted. My husband Jakub deserves special thanks. He provided me motivation and driving force to complete my Ph.D. studies by doing his first. And finally, I am grateful for my son who let me finish this thesis by sleeping whole nights.

Abstract

Structural health monitoring (SHM) became a part of the modern approach for aircraft design – damage tolerance. This thesis deals with one of the leading SHM methods – ultrasonic guided wave (UGW) testing. The research is focused on the applicability of damage detection in typical composite aircraft structures. Fast determination of the phase velocity dispersion curve is proposed to contribute to the propagating mode identification. Concurrently, the specific phase velocity is used as an input for the precise delamination length calculation. An improved data pre-processing for the probabilistic algorithm is utilized for damage imaging as impact damage or debonding in simple and complex structures. Finally, the influence of operational and environmental conditions is addressed. Unique data within the wide temperature range corresponding to operational conditions of an aircraft are obtained and moreover, measurements during the real flights are conducted. Qualitative evaluation was proposed to distinguish temperature-affected and damage-affected signals. It has been proved that regarding impact damage using the proper signal pre-processing small temperature variations does not have to be compensated.

Keywords: Aircraft structures; Composites; Damage detection; Lamb waves; Structural health monitoring

Abstrakt

Monitorování stavu konstrukce (SHM) se stalo součástí moderního přístupu konstrukce letadel, a to konstrukce s přípustným poškozením. Tato práce se zabývá jednou z předních metod SHM – zkoušení pomocí ultrazvukových deskovýh vln (UGW). Výzkum je zaměřen na aplikovatelnost detekce poškození v typických kompozitních leteckých konstrukcích. Rychlé stanovení disperzní křivky fázové rychlosti je navrženo k identifikaci šířícího se módu. Současně je konkrétní fázová rychlost použita jako vstup pro přesný výpočet délky delaminace. Vylepšené předzpracování dat pro pravděpodobností algoritmus umožnilo detekci a zobrazení typických poškození typu impakt a rozlepení v jednoduchých i komplexnějších konstručních částí. Dále byl řešen vliv provozních podmínek a podmínek prostředí. Byly získány unikátní data v širokém teplotním rozsahu odpovídajícím provozním podmínkám letadla, a navíc byla provedena měření při skutečných letech. Bylo prokázáno, že pokud se jedná o hodnocení impaktového poškození, není nutné určitým zpracováním signálu malé teplotní výkyvy kompenzovat.

Klíčová slova: Lambovy vlny, monitorvání stavu konstrukcí, detekce poškození, kompozity, letecké konstrukce

Content

List of abbreviations

AE	Acoustic emission
A0	Fundamental antisymmetric mode
BSS	Baseline signal stretch
BVID	Barely visible impact damage
CAN	Contact acoustic nonlinearity
CFRP	Carbon fibre reinforced polymer
CVM	Comparative vacuum monitoring
DCB	Double cantilever beam
DI	Damage index
DT	Damage tolerance
FBG	Fibre Bragg Gratings
FEM	Finite element method
FFT	Fast Fourier transform
FOS	Fibre optic sensors
GMM	Global matrix method
ISA	International standard atmosphere
LHS	Left hand side
LS	Laser shearography
L	Longitudinal wave
MIA	Mechanical impedance analysis
NDI	Non-destructive inspection
NDT	Non-destructive testing
OBS	Optimal baseline selection

PA	Phased array
PC	Pitch-catch
PE	Pulse-echo
POD	Probability of detection
PWAS	Piezoelectric wafer active sensors
PZT	Lead zirconate titanate
RAPID	Reconstruction algorithm for the probabilistic inspection of damage
RHS	Right hand side
S	Shear wave
S0	Fundamental symmetric mode
SAFE	Semi-analytical finite element
SG	Strain gauges
SH	Shear horizontal wave
SHM	Structural health monitoring
SLDV	Scanning laser Doppler vibrometer
SMM	Stiffness matrix method
SSM	Scaling subtraction method
SV	Shear vertical wave
SW	Software
T	Transversal wave
ToF	Time of flight
TOFD	Time of flight diffraction
TR	Time reversal
TMM	Transfer matrix method
TRL	Technical readiness level

TT	Through-transmission
UGW	Ultrasonic guided waves
UL	Ultralight
UT	Ultrasonic testing
VID	Visible impact damage
WT	Wavelet transform
VZLU	Czech aerospace research centre/Výzkumný a zkušební letecký ústav

List of quantities

A Amplitude

c_L Longitudinal velocity

c_T Transversal velocity

c_P Phase velocity

c_g Group velocity

G_{IC} Fracture toughness in mode I

Γ Period

f Frequency

λ Wavelength

φ Phase

Δt Time difference

T Temperature

k Wavenumber

λ, μ Lamé constants

E Young modulus

G Shear modulus

ν Poisson´s ration

ρ Density

T_R Transmission coefficient

R_R Reflection coefficient

Z Acoustic impedance

d_{min} Minimum detectable defect size

u Displacement

∇	Nabla operator
∇^2	Laplace operator
ω	Circular frequency
σ	Stress
C	Stiffness matrix
C_{ij}	Elastic constants
φ	Scalar potential
ψ	Vector potential
d	Half thickness of the plate
P_i	Probability of damage
R_i	Location parameter
β	Scaling factor
a_n	Delamination length

1 Introduction

1.1 Motivation

The human desire to make things better has always resulted in innovations. Since Otto Lilienthal's first hill glide, the aeronautical industry has gone a long way and become one of the former leaders of research and development in engineering. However, not only new inventions and products should be of interest, but also the aging of operating aircraft and systems must be covered.

In the past decades, the service life of most operating aircraft was determined via the safe-life approaches. Aircraft are excluded from operation after the exact number of flight hours and take-offs regardless of the structural condition. The safe-life philosophy does not exploit full potential of used materials and does not cover increasing requirements for structure lifetime. That's why the current airworthiness requirements (CS, FAR, etc.) prefer design and operation structure according to the damage tolerance philosophy. For some structures, especially for composite structures, the damage tolerance (DT) philosophy is strictly required. Therefore, advanced airframe structures are currently designed and operated according to the DT philosophy to extend the airframe service life [1]. Non-destructive testing (NDT) and structural health monitoring (SHM) play an essential role in DT design by increasing safety by monitoring/inspection of structural parts. NDT is performed at regular time-based intervals during aircraft maintenance, whereas structural health monitoring (SHM) is considered a condition-based approach and should be adopted as alarms for conventional NDT. This process leads to a reduction in maintenance costs and an increase in aircraft availability. Some NDT and SHM methods use similar physical principles, but the different approach makes SHM online and condition-based monitoring with sensors permanently attached or embedded into the structure [2,3,4].

Not only the design approach has changed – damage tolerance instead of the safe life but also the base of the materials. Ambitions for lightweight aircraft led to replacing aluminium alloy components with carbon composites. Total weight attributed to composites has increased up to more than 50% (which is 80% by volume) in the case of the Boeing 787 Dreamliner [3]. This percentage includes the highest carbon fibre reinforced polymers (CFRP) rate, including skins of sandwich structures and fiberglass composites. Thermoplastic composites experience increased interest due to high-performance, profitable, and sustainable manufacturing processes. Other materials include common aluminium alloys, titanium, and steel. The design

of lighter aircraft is one of the major ways to reduce fuel consumption. The percentage of composites is still increasing, especially for the primary structures.

In-service aircraft shall be in acceptable technical conditions. Therefore, regular system inspections and structural parts maintenance have become an integral part of an aircraft operation. Possible damages regarding the integrity of aircraft structures can be caused by single or multiple impacts either during the flight or on the ground, by operational loads, or by their combination. These damages shall be revealed employing conventional NDT. Structural defects caused by manufacturing processes above a given defect size extent shall be discarded through the standard quality control NDT processes. However, DT approach tolerates manufacturing defects below a given size limit [5] and existence of defects in general is assumed from the beginning of operation. Fracture mechanisms at the microstructure level include matrix cracking, fibre breakage, fibre-matrix debonding, and delamination. Delamination is the most common, and one of the most serious damages in fibre reinforced composites and occurs as a result of an impact, compression, tension, or bending loadings [6]. In composites, internal damage can occur much earlier than is detectable by methods used in a common service. Therefore, a critical flaw that significantly decreases the strength of a structure should be within a detectable limit of the particular NDT technique [7]. The aim of NDT and SHM is to detect and monitor flaws earlier, than the critical size is reached.

During operation, aerospace composite structures must withstand all kinds of damages and no damage must reduce the strength of the structure below the defined limit. According to the literature [8], more than 50% of all damages detected in 10 years of composite wing monitoring of two types of aircraft fleet were caused by impacts. Impacts can be caused by bird strikes, hails, tool drops, area debris, etc., and among other parts are highly concentrated in door-surround areas [9]. Special attention has been paid particularly to barely visible impact damages (BVID) caused by low-velocity impacts (dropped tools, runway debris). While impacts in metallic structures cause a visible dent, BVID in composites is difficult to be inspected visually and, due to loss of compressive strength, may lead to catastrophic failures [10]. Typical dent depth is considered 0.25-0.5 mm [11]. Total damage area is dependent on impact energy, impactor diameter [12] and structural stiffness. The stiffer the structure, the more extensive the damage.

Current developments regarding the structural design also focus on adhesively bonded composite joints, which represent mostly a typical fuselage horizontal joint or fuselage/wing skin-stringer joint. Adhesive bonding alone is still not accepted by authorities for primary structures, so fasteners such as rivets are used in combination for bonding the composite substructures [13]. To use adhesively bonded joints alone and ensure their reliability is a great challenge that could achieve another significant decrease in the weight of an aircraft.

Therefore, pure bonding technology using adhesives and proper SHM method and proved evaluation technique could contribute to the final certification.

Nevertheless, the decrease in aircraft production in the Czech Republic (except for ultralight aviation) caused a research and development slowdown. SHM is one of the topics worth keeping up with the leading countries. Current worldwide research in SHM is mostly focused on Fibre Bragg Grating (FBG) sensors and active ultrasonic guided wave (UGW) testing using PZT sensors. The field of FBG sensors is in the Czech Republic well covered by commercial companies as well as academics [14, 15]. However, there is a significant opportunity for advancement since not many researchers deal with ultrasonic guided waves testing compared to those abroad. Therefore, the topic of this thesis was chosen to be SHM of composite aircraft structures exploiting the UGW method, mainly due to the worldwide significance and lack of research in the Czech Republic. However, the field of UGWs is a very broad topic. This thesis is limited especially to experimental studies performed on several typical composite aircraft structures from the point of view of damage detection and evaluation.

1.2   The structure of the thesis

The thesis is divided into 11 chapters and covers the theoretical part, state-of-the-art, and experimental part with the corresponding conclusions. Chapter 1 outlines the motivation for the research and general background to connect the dots between aviation, materials, and damage detection. The first chapter naturally leads to the selection of the scientific field of Lamb waves as a topic for the thesis. The thesis structure is also presented in Chapter 1. Chapter 2 provides the basic knowledge of the distinction and behaviour of elastic waves in solids. The exploitation of elastic waves in NDT is covered in chapter 3. Chapter 4 provides fundamentals and the basic features of Lamb waves. Mathematical derivation resulting in the Rayleigh-Lamb dispersion equation is introduced. Lamb wave generation and detection are outlined within the subchapters, focusing on piezoelectric wafer active sensors (PWAS). The difference in propagation in isotropic and anisotropic structures is explained, and the concept of dispersion, distinguishing phase and group velocity, is addressed. Finally, the temperature dependency and nonlinear behaviour of Lamb waves are briefly mentioned. Chapter 5 begins with state-of-the-art. First, dispersion curve determination methods are outlined, and then damage detection approaches that correspond to those in the experimental part are pointed out. In Chapter 6, the objectives of the thesis are clearly stated. The experimental part begins with Chapter 7. A methodology for phase velocity determination is proposed, and results are compared to calculations obtained using GUIGUW SW or Rayleigh-Lamb equation. Chapter 8 concentrates on the experimental investigation of different aerospace structures. The

structures were tested, and relevant damages were evaluated. Subchapters examine delamination propagation in DCB specimens, then impact damage detection in various structures, and finally delamination/debonding propagation in adhesively bonded joints. In Chapter 9 the temperature effect on Lamb wave propagation is investigated in a wide temperature range and real operational conditions. A comparison of the temperature-influenced and damage-influenced wave packets is demonstrated. In Chapter 10 the thesis is summarized, and the results are discussed including the limitations. Within the final Chapter 11, the key conclusions are highlighted, and the contribution of the thesis is pointed out.

1.3   SHM background in aerospace

Structural health monitoring (SHM) is defined, for example, as the process of implementing a damage identification strategy for aerospace, civil, and mechanical engineering infrastructure [8]. SHM system comprises hardware, transducers and associated instrumentation, and software elements for damage detection, optionally for modelling and other analyses [16]. SHM, in general, is a very complex process and interdisciplinary research field dealing with various scientific branches such as physical principles of the methods, experimental testing, wired/wireless sensing technologies, signal processing methods, detection and localization algorithms including machine learning, visualization techniques, data acquisition unit architectures, FEM (finite element method) simulations, etc. Basic physical principles may be identic for some NDT and SHM methods. However, the main differences are summarized in Table 1.

Table 1 NDT versus SHM approach [17]

NDT	SHM
Off-line monitoring	On –line monitoring
Time-based monitoring	Condition-based monitoring
Baseline not available, calibration required	Baseline required
More cost and labor	Less cost and labor
Hot spot monitoring	Large area monitoring
Find existing damage	Environmental data compensation required

In the field of aircraft structures, SHM approach as an upgrade of standard NDT is going to be an integral part of damage tolerance philosophy and certification processes. However, many requirements need to be met. Verification of SHM methods starts, of course, on the

baseline of the building block approach (coupons → elements → components → full-scale testing) and requires the assessment of the reliability of the methods themselves and the durability of the sensors, measuring devices algorithms, etc. Environmental conditions such as temperature and humidity affect the mechanical properties of monitored structures and may lead to false alarms. Therefore, verification also includes the corresponding environmental conditions. Enough tests must be performed to evaluate Probability of detection (POD) curves [4].

The purpose of both NDT and SHM is similar and can be historically categorized into four levels [18]:

1) damage detection,

2) damage localization,

3) damage quantification,

4) remaining life prediction

The first three levels are typical for both SHM and NDT. Prediction of the remaining life is considered an integral part of the SHM approach. Some sources state that the SHM system should also determine the specific type of damage [19].

Based on the literature, it is possible to sort out SHM methods in many ways. For example, on the concept of passive and active SHM, large scale and hot spot monitoring (global/local), according to the sensing technology, etc. The following methods are considered as the main SHM methods [20]:

- Vibration-based testing
- Acoustic emission testing
- Ultrasonic guided wave testing
- Fibre optics technology
- Strain Gauges
- Comparative vacuum monitoring

The methods are competing in some aspects; however, each one of them has its unique features and advantages and is suitable for different purposes. Yet, there are currently two leading SHM streams – fibre optics with FBG sensors and ultrasonic guided wave testing (UGW). FBG sensors are mainly intended for stress/strain measurements and are considered a good alternative to strain gauges (SG), especially due to their immunity to electromagnetic interferences [21]. Innovations in higher sampling rates of data acquisition units and other

methodologies in signal processing enabled monitoring of dynamic processes as impact detection and even localization [22, 23, 24].

Sensing technology of optical fibres lies in either interferometric systems, distributed systems exploiting linear (Rayleigh scattering) or nonlinear effects (Raman or Brillouin scattering), or in sensing technology using gratings. Fibre-Bragg grating sensors became of great interest. Gratings are in a fibre created as a periodical change of refractive index. Reflected wavelength is related to the gratings distance. Since the fibre is embedded or tightly attached to the tested structure with compression or tension, the wavelength shift is measured [25].

The method of comparative vacuum monitoring (CVM) is a very interesting method developed in 90' primarily used for fatigue crack detection and monitoring. Differential pressure between alternating galleries of low vacuum and atmospheric pressure is measured. If a crack is initiated, air flows into the vacuum galleries [26].

Acoustic emission (AE) testing is also a powerful tool for damage detection, localization, and even for characterization, especially in early stages. AE method utilizes AE phenomenon – a sudden release of mechanical energy in the form of elastic waves. Elastic wave generation, usually in the frequency range of 100 kHz-1MHz, is caused by irreversible structural changes. Crack initiation and propagation, corrosion and even the plastic deformation in metals or delamination, fibre breakage and matrix cracking in composites are possible to detect usually using PZT transducers. The main limitation of AE is the noisy environment. However, there are postprocessing tools to eliminate such useless data. Yet, it is a perfect method for leakage detection in pressure vessels and for mechanical tests in low-noise environments with the objective to detect damage initiation stages [27]. Modern concepts of data pre-processing/post-processing tools may be applied to improve results obtained by AE [28].

Strain measurements using strain gauges (SG) have become the basis of various mechanical tests [21]. SGs are exploited within real-time measurements regarding the estimation of the remaining service life. The use of this method is very wide. From laboratory tests to measurements using a few sensors performed on specific structural parts up to the multi-channel wireless sensing technologies.

Vibration-based testing may be exploited in various modifications. The information about the monitored object is mostly evaluated based on comparing the baseline measurement and measurement in the damaged state. Since any damage influences the overall object stiffness, modal characteristics naturally change [29].

UGW testing is suitable for relatively thin structures. Such structures include especially plate-like aircraft structures and pipelines. The significance of this method lies in the characteristics of the guided waves, which excel especially in low attenuation and the ability to interrogate

large structures with a few sensors. Guided waves are actuated into the host structure, mostly using the PZT transducers serving as both actuators and sensors. UGW testing gained success in pipeline inspection and even became a certified NDT method [30]. However, in the field of SHM for aircraft structural parts is this method still in the phase of research, development, testing, and verification. The research groups around Rose, Giurgiutiu, Lowe, and many others significantly contributed to the area of UGW. Acellent technologies developed various devices to use this method in service, including damage detection SW and the sensing technology – the SmartLayers© sensors. In the Czech Republic, some research has been done, especially theoretically by Hora [31], Šofer [32, 33], and experimentally by Hedl in Honeywell [34, 35].

In addition to methods mentioned above, there are many more under detail research with so far lower technical readiness levels (TRL). Particularly Electrical Resistance Tomography is worth mentioning since the author participated in the verification of this method for impact damage detection [a].

2   Elastic waves in solid media

Necessary basics regarding elastic waves propagation and behaviour in solids are introduced in this chapter. Two basic types of vibration are described, and by introducing different boundary conditions, other kinds of waves are distinguished. Important characteristics are outlined. This chapter is followed by Chapter 3, addressing elastic waves in NDT, and Chapter 4, focusing specifically on Lamb waves.

2.1   Overview

Materials are composed of atoms and forced vibrations and time-varying deformations of these atoms and molecules form mechanical waves. Nevertheless, we speak of elastic waves as macroscopic phenomena, and detailed atomic structure is unimportant. Lengths characterizing the microscopic structure of most materials are generally much smaller than any lengths arising in the deformation of the medium. Transmission of mechanical motion is essentially enabled by deformability and inertia of a medium. Elastic waves can propagate in two fundamental ways – longitudinal and transversal. All other ways are superpositions of these primary motions. Mechanical and geometrical properties define the way of vibrations [36, 37].

Different aspects may be used to sort out the elastic waves. Oscillations varying in time and space indicate traveling waves, whereas only in-time oscillations reflect standing waves. Particle motion defines the way of vibration. Geometrical boundary conditions divide waves into bulk waves in an infinite space, surface waves in a half-space, and guided waves in waveguides. The frequency parameter can divide the whole spectra into infrasound, sound, ultrasound, and hyper sound.
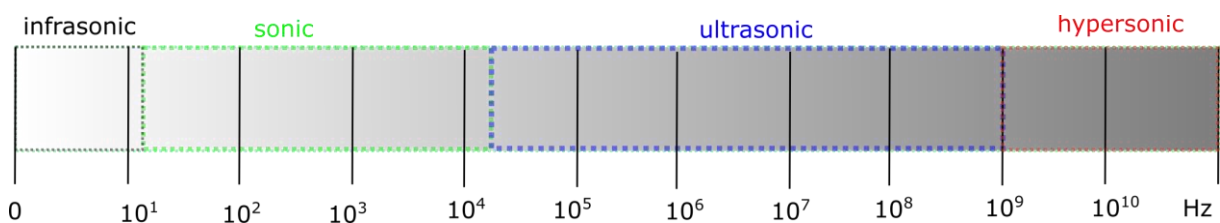
Figure 1 Elastic waves frequency spectra

Traveling waves described by harmonic functions are of interest in this work; therefore, relations of basic features need to be defined. A wave traveling in space and time (Figure 2) has the following mathematical description:

$$y(x,t) = Asin(kx - \omega t + \varphi), \qquad (1)$$

and the following characteristics and basic relations:

frequency f, phase φ, wavelength λ, wavenumber k, angular frequency ω, period Γ and velocity c, where:

$$f = \frac{1}{\Gamma} \qquad (2)$$

$$\omega = 2\pi f \qquad (3)$$

$$\lambda = \frac{c}{f} \qquad (4)$$

$$k = \frac{2\pi}{\lambda} \qquad (5)$$

a)

b)
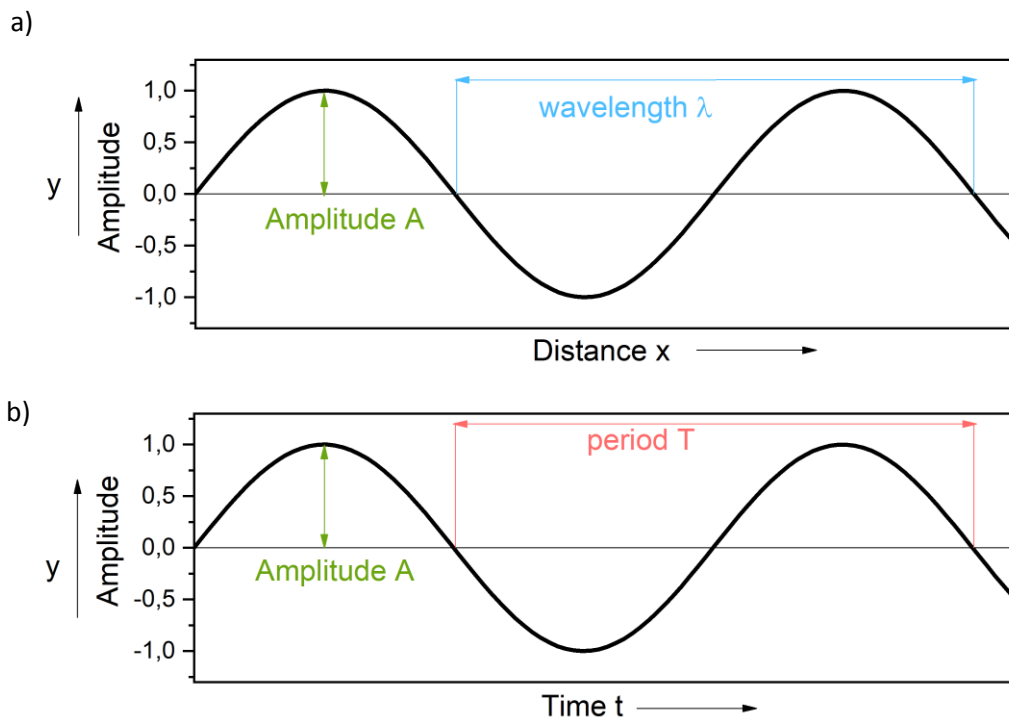
Figure 2 Wave definition in a) space and b) time

Longitudinal and transversal waves

Basically, there are only two ways of vibrations – longitudinal and transversal. In infinite media, these vibrations propagate as longitudinal and transversal bulk waves. In a longitudinal wave, the direction of motion is parallel to the direction of wave propagation (Figure 3a). In a transverse wave, the displacement is perpendicular to the direction of wave propagation, which leads to two possibilities of transversal motions – vertically (shear vertical SV) or horizontally (shear horizontal SH) polarized motions (Figure 3b, c). In general, transverse waves may have both vertical and horizontal polarizations combined [38]. All other waves are combinations of these basic motions.

Note: Longitudinal (L) waves are also designated as pressure, compressional, irrotational, dilatational, and P-waves (primary, pressure). Transversal (T) waves are also designated as shear, distortional, rotational, and S-waves (shear, secondary) [38]. Terms P and S waves are used mainly in the field of geophysics [39].

Longitudinal c_L and transversal c_T velocities are constant (except for the high-frequency range where the wavelength is comparable with the particle size [40]) for the given material and are specifically dependent on the material density ρ and elastic constants as follows:

$$c_L = \sqrt{\frac{\lambda + 2\mu}{\rho}} \tag{6}$$

$$c_T = \sqrt{\frac{\mu}{\rho}} \tag{7}$$

Symbols λ and μ are denoted as Lamé constants defined for isotropic material as:

$$\lambda = \frac{\nu E}{(1 + \nu)(1 - 2\nu)} \tag{8}$$

$$\mu = \frac{E}{2(1 + \nu)} \tag{9}$$

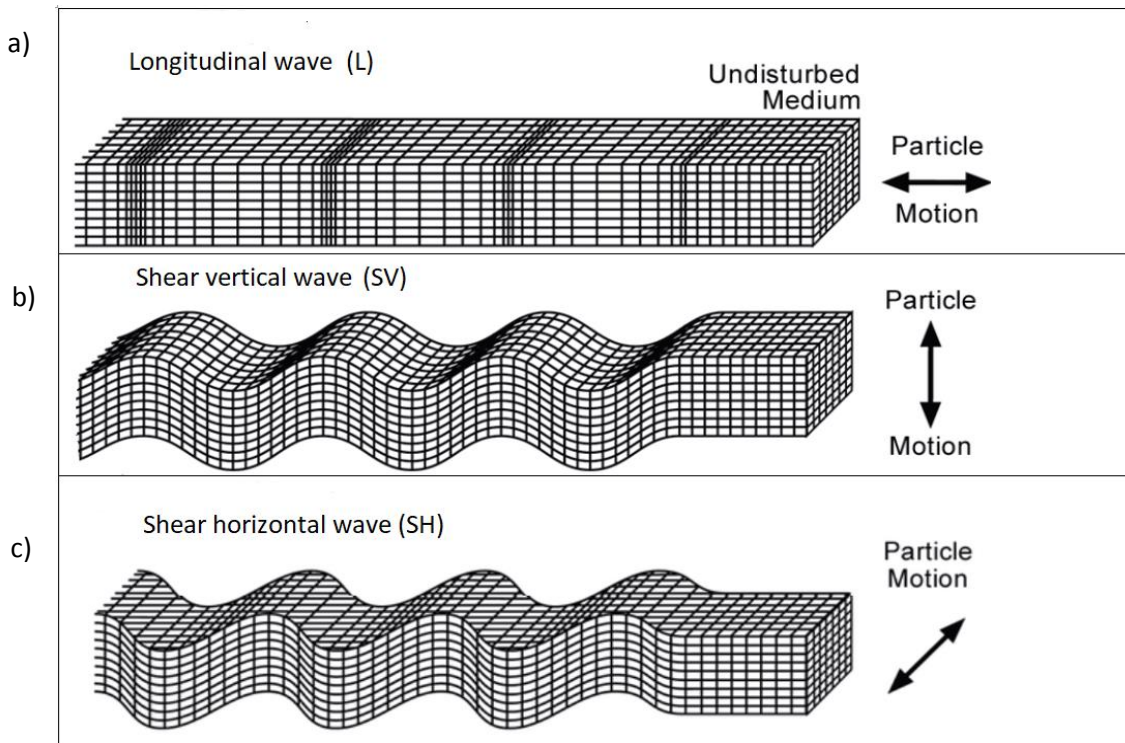where ν is Poisson´s ratio and E is Young modulus.

Figure 3 Particle motion of the a) longitudinal wave, b) shear vertical wave and c) shear horizontal wave [41]

Surface waves

Surface waves travel along the free surface or the boundary of two dissimilar media. There are two types of surface waves to be distinguished – Rayleigh and Love waves. In the case of Rayleigh waves, particle motion is a combination of longitudinal and shear vertical vibrations resulting in an elliptical retrograde motion (Figure 4a). Rayleigh waves reach up the depth of approximately one wavelength since the amplitude decreases fast. Love waves propagate as reflections of shear horizontal waves (Figure 4b) in a surface layer with different material properties than the rest of the infinite half-medium. Therefore, Love waves cannot propagate in semi-infinite homogeneous medium and can also be considered as waves propagating in layers. Rayleigh wave travels with constant velocity in homogeneous media but is dispersive in non-homogeneous media. Love waves are dispersive with velocities ranging between the shear velocity of the layer and the half space [39].
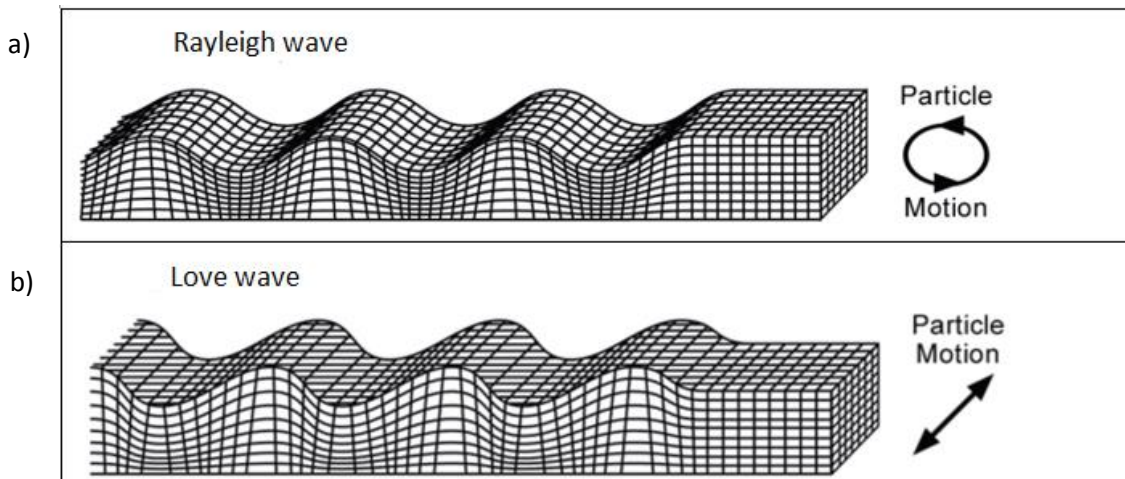
Figure 4 Particle motion of the a) Rayleigh wave, b) Love wave [41]

Guided waves

There are structures which for wavelengths comparable to or greater than the structure thickness, create such boundary conditions that the wave is guided by the two surfaces of that structure. Such waveguide-like structures include especially thin plates, rods, tubes, shells, and multi-layered structures [17]. Various guided wave modes may form in the waveguide based on the actuation frequency, geometrical and material properties, and on the way of actuator excitation (vibration mode).

In thin plate-like structures, guided waves propagate as Lamb waves (comprised of the L and SV waves) and shear horizontal (SH) waves. The motion is in the pure form either symmetrical or asymmetrical with respect to the midplane of the structure across the thickness. Guided waves are generally dispersive except the fundamental SH0 mode, which propagates with constant velocity across the whole frequency-thickness range. The fundamental zero-order modes (A0, S0, SH0) exist within the whole frequency spectra. With increasing frequency, the number of propagating modes (higher order modes) increases. The number and type of Lamb wave modes for a given frequency correspond to the number of solutions (real roots) of the Rayleigh – Lamb equation [42, 43].

The concept of Lamb waves was initially valid for isotropic materials. However, composite structures may satisfy certain conditions, and Lamb waves may propagate as well. However, a strict distinction of displacement components for the corresponding modes is no longer possible. Therefore, the term "quasi" - Lamb waves is often used as a more appropriate designation [43].

12

Special cases

Along the solid-solid interface may propagate Stoneley waves and the solid-liquid interface Scholte waves. There are also special cases of waves called feature guided waves. These waves propagate under certain conditions in structures as welds or bends [44]. For instance, if the wave propagation velocity in a weld is smaller than in the rest of a plate, the wave gets trapped into a weld and propagates there [45].

2.2   Wave behaviour at the interface

Since all natural structures have boundaries separating two media, wave behaviour at these boundaries or interfaces is key to understanding. The waves at the interface behave based on the characteristics of the corresponding media. Basically, reflection and transmission/refraction occur. Complete reflection occurs only if an elastic body is adjacent to a vacuum. The perpendicular incident wave causes transmission and reflection in the same perpendicular direction. Snell´s law and the law of reflection describe the behaviour for oblique incidence. Refraction angle is dependent on the incident angle and corresponding wave velocities in both media (materials) as follows [46, 47]:

$$c_2 sin\beta_1 = c_1 sin\beta_2 \quad \text{(Snell´s law)} \tag{10}$$

Where v_1, v_2, are corresponding velocities in both environments, β_1 and β_2 are angles of incident and refracted wave, respectively.

$$\beta_1 = \beta_1^{'} \text{ (Law of reflection)} \tag{11}$$

Where β_1 is incident and $\beta_1^{'}$ reflected angle.
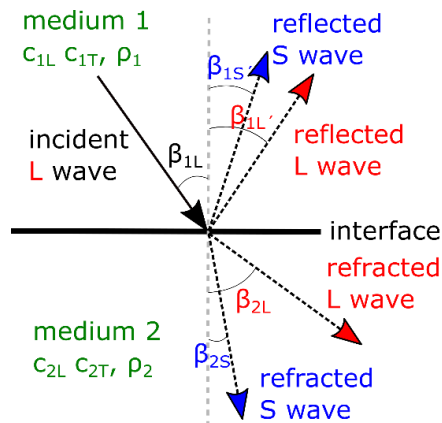

Figure 5 Wave behaviour at the interface

So-called critical angles are also derived from the Snell´s law. Basically, for the incident longitudinal wave, there are three ranges of incident angles:

1. The longitudinal and transversal waves are refracted up to the first critical angle.
2. The longitudinal wave disappears at the first critical angle, and subsurface longitudinal and shear waves propagate.

$$\beta_{1critical} \rightarrow \beta_{2L} = 90° \tag{12}$$

3. Only the shear wave is refracted between the first and the second critical angle.
4. The shear wave disappears at the second critical angle, and the subsurface shear wave propagates.

$$\beta_{2critical} \rightarrow \beta_{2S} = 90° \tag{13}$$

5. Increasing incident angle above the second critical angle Rayleigh wave propagates.

The shear forces in the media enable the conversion of an incident longitudinal wave into the refracted shear wave. Therefore, in media without shear forces (e. g. air), shear waves do not propagate. The propagation direction of the corresponding wave is given by Snell´s law, while energy distribution by means of transmission and reflection is given by the acoustic impedance:

$$Z = \rho c \tag{14}$$

Where Z is acoustic impedance, ρ is the density of the media, and c is the corresponding wave velocity.

$$R = \frac{Z_2 - Z_1}{Z_2 + Z_1} \tag{15}$$

$$T_R = \frac{2Z_1}{Z_2 + Z_1} \tag{16}$$

Where R is the reflection coefficient and T_R is the transmission coefficient. According to the energy conservation, their sum is 1.

2.3   Superposition principle

Propagating waves in space and time behave according to the superposition principle – the resulting wave is a superposition of all waves present [38]. Waves interfere with each other. A special case of superposition is constructive or destructive interference based on waves being in phase or out of phase. Then, the combined waveform is either enhanced or suppressed. Unique interference patterns of vibrations called modal shapes exist for every structure at resonant frequencies. Patterns are physically standing waves (the shape of the mode does not travel) and are described by frequency and shape [37].

Regarding the Lamb waves, the superposition principle is applied in two ways. In the way of superposition of all waves present and their reflections and in the way of superposition of waves of slightly different frequencies into a wave packet. Frequency components in waves of multiple frequencies are distinguished using the Fourier analysis [37].

3   Elastic waves in NDT

Elastic waves described in Chapter 2 are exploited in NDT in many ways. The flaw is considered as an interface for the propagated elastic wave. Therefore, in the simplest case, wave reflections by the flaw can be measured using a simple probe and oscilloscope. Other phenomena such as wave scattering, mode conversions, higher harmonics generation, etc., can be observed when appropriate wave interacts with the flaw. Then, more complex equipment and signal analysis are conditional.

Elastic waves, particularly in the ultrasonic range (above 20 kHz), have become important in the field of NDT and SHM. Besides damage detection (manufacturing/operational defects), material characteristics can be evaluated using ultrasonic waves.

Table 2 Overview of the elastic wave-based NDT methods

Method	Frequency range	Damage type	Wave types
UT – PE, TT	1-25 MHz	Impact damage detection, voids, delamination, debonding	Bulk waves, Rayleigh waves
UT – Phased Array	1-25 MHz	Impact damage detection, voids, delamination, debonding	Bulk waves
UT - TOFD	5-10 MHz	Cracks	Bulk waves
Air coupled low frequency UT	50 – 400 kHz	Damages in sandwich structures	Bulk waves
Acoustic emission	Up to 1 MHz	Actual dynamical state: Crack growth Fibre breaking, matrix cracking, etc.	Bulk waves, Rayleigh waves, Lamb waves
Pitch - Catch	5-100 kHz	Damages in sandwich structures	Lamb waves
Tap test	20 Hz - 20 kHz	Structural defects in general	Bulk waves
MIA	2-10 kHz	Debonding (in sandwich structures)	Bulk waves
Resonant method	25 – 500 kHz	Voids, delamination, adhesive assessment	Bulk waves

Ultrasonic methods exploited in NDT are summarized in Elastic waves described in Chapter 2 are exploited in NDT in many ways. The flaw is considered as an interface for the propagated elastic wave. Therefore, in the simplest case, wave reflections by the flaw can be measured using a simple probe and oscilloscope. Other phenomena such as wave scattering, mode conversions, higher harmonics generation, etc., can be observed when appropriate wave interacts with the flaw. Then, more complex equipment and signal analysis are conditional.

Elastic waves, particularly in the ultrasonic range (above 20 kHz), have become important in the field of NDT and SHM. Besides damage detection (manufacturing/operational defects), material characteristics can be evaluated using ultrasonic waves.

Table 2. Although the methods are designated as ultrasonic, some of them also work in the audible range. Longitudinal and shear bulk waves are utilized in the conventional ultrasonic pulse-echo (PE)/through-transmission (TT) testing, regardless of the type of structure. PE technique exploits wave reflection utilizing a probe as a transmitter and a receiver. TT technique requires two probes on both surfaces of the tested object, the first as a transmitter and the second as a receiver, and naturally measure the wave transmission. Pitch-catch (PC) configuration uses one probe with transmitting and receiving elements placed on one surface. When testing structures with multiple interfaces, R and T coefficients can be used to determine which substructure is still possible to test. Single element probes give the result corresponding to one tested spot, while multi element phased array probes produce scans of the certain segments. The method of TOFD (Time of flight diffraction) exploits the wave scattering phenomena. In the case of a crack, the wave is scattered by the upper and lower tip of the crack. Then, ToF is measured to determine the location and size of the flaw. This method is always applied with imaging methods. [20, 47, 48].

Apart from the conventional UT methods, special cases require unconventional approaches such as the water squirt-technique or air-coupled low-frequency method. From a large-scale point, flaws may also reflect changes in the structure resonance, and then, resonance-based analyses are utilized [49]. On the other hand, mechanical impedance is influenced by local changes, and mechanical impedance analysis (MIA) is utilized [50].

Except for the bulk waves, surface Rayleigh waves can be utilized in the NDT to detect surface and subsurface defects [51]. In addition, acoustic emission phenomenon produces elastic waves, and when reaching the surface, conversion to Rayleigh or Lamb waves occur. Acoustic emission method is the only passive method with the advantage of reflecting the actual state of the structure.

Inspection of relatively thin structures can be performed using Lamb waves which are guided by two mostly parallel surfaces and will be discussed later. Lamb waves influence the whole thickness, and possible flaws disturb in some way the particular wave mode. Therefore, they show excellent flaw sensitivity [52]. Lamb waves can interrogate the whole structure, unlike conventional UT methods, which affect only a limited area in the vicinity of the probe. The fundamental difference is depicted in Figure 6. However, within the concept of NDT, bond quality is successfully tested using Lamb waves exploiting UT probes [53]. Amplitude increase is linked with the debonded region.

Methods used for inspections are chosen based on the type of the structure (simple plates, sandwich structures, adhesively bonded structures, etc.), expected defects (welds, cracks, VID, BVID, debonding, delamination, voids etc.), or other conditions (environmental, operational).
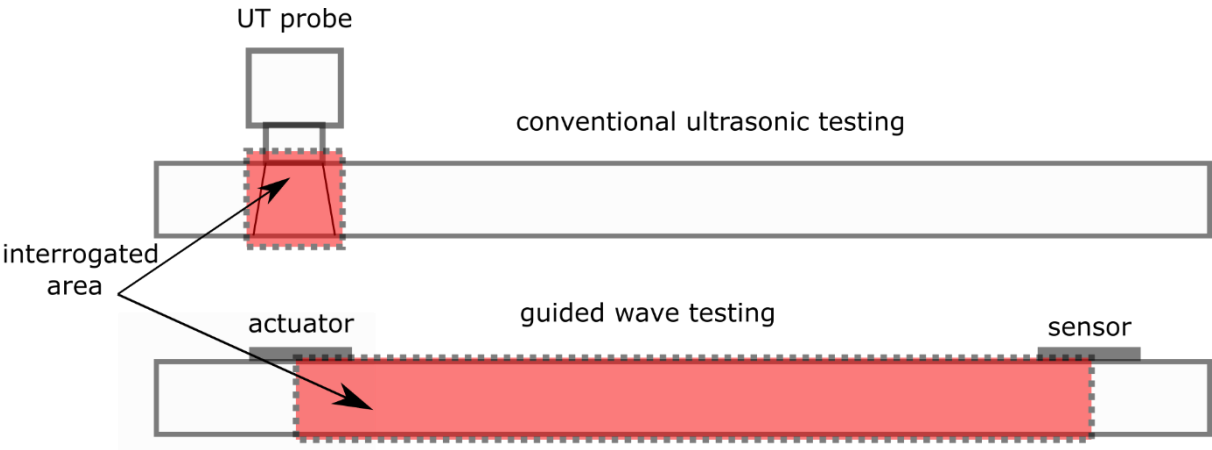
Figure 6 Difference in interrogated area using conventional ultrasonics and guided wave method

Attention to the proper selection of the UT probe frequency shall also be paid. Higher frequency waves exhibit higher attenuation than lower frequency waves. Therefore, materials with significant attenuation or thicker structures are inspected using low-frequency probes. However, inspections using higher frequencies enable better size resolution of the defect due to the shorter wavelength. Theoretically, one-half the wavelength corresponds to the minimum defect size that can be detected [46]. The frequency (mainly in the range of 1-20 MHz) is chosen according to the following relation:

$$f = \frac{c}{\lambda} \tag{17}$$

$$d_{min} = \frac{\lambda}{2} \tag{18}$$

Where d_{min} is the minimum detectable defect size. The frequency selection is based on the requirements of the minimum detectable flaw and geometrical and material properties of the tested structure.

The main objectives of the structure inspection can be stated as:

1. Damage detection
2. Damage localization
3. Damage quantification

Defects are evaluated mainly using two parameters – time of flight (ToF) and amplitude. In the conventional PE technique, ToF reflects the location of the defect (and thickness in general) while the amplitude is exploited for the flaw sizing. The precise knowledge of the wave velocity in the given material/structural part plays a key role, primarily in correctly localizing the damage. However, other UT methods may evaluate defects by means of different indicators (damping, amplitude increase for disbond detection, phase change). A very important requirement for all methods is calibration. Reference calibration blocks are mostly used to calibrate the sensitivity; nevertheless, some techniques exploit calibration on the "good" part of the tested structure to distinguish the "bad" part.

Apart from the NDT, ultrasonic waves are exploited for material characterization [54]. Velocity and attenuation are the important parameters related to material characteristics. Ultrasonic velocity corresponds with elastic constants and density. Attenuation reflects different mechanisms like thermal loss, scattering, absorption, etc. Both parameters correlate several physical properties such as elastic constants, microstructure, discontinuity, and mechanical properties [55].

4   Lamb waves

This chapter is focused on the Lamb wave key characteristics in relation to the experimental part. PZT discs are used within the experimental part; therefore, generation and detection using PWAS are addressed. The dispersion concept is introduced, which is then reflected in velocity dispersion curves. A mathematical description of Lamb wave propagation resulting in the Rayleigh-Lamb equation is derived. This equation is considered a basic equation for Lamb-wave propagation in isotropic structures and is later exploited for phase velocity calculations. Propagation in anisotropic structures is outlined to understand the comparison with the isotropic structures since the thesis is focused on the composites. Finally, some other features such as environmental dependency and nonlinear behaviour are mentioned.

4.1   Introduction

In thin-walled structures propagate special cases of guided waves – Lamb waves, existing in two mode shapes: symmetrical and asymmetrical. As stated before, two conditions must be satisfied for pure Lamb waves to propagate:

1. The wavelength is comparable to or greater than the structure thickness.
    Waves with much smaller wavelengths may propagate as Rayleigh waves or bulk waves.
2. The structure is symmetrical, which is naturally satisfied for isotropic materials such as metals.
    Anisotropic and even layered anisotropic structures enable propagation of Lamb-type waves as well. However, the perfect symmetric or asymmetric shape with respect to the midplane of the waveguide is lost.

Generally, the investigation of Lamb waves leads to the introduction of several new concepts such as multimodal wave propagation, dispersion, and group velocity [37, 56]. Lamb-type waves are uncoupled into symmetric and antisymmetric modes with respect to the midplane. The system forms a standing wave across the thickness of the structure so that the propagation is essentially in the direction of the plate. The key feature of Lamb waves is geometrical dispersion resulting in the velocity dependency on the structure thickness and actuated frequency. The number, type, and velocity of the propagating modes are described by dispersion curves. The fundamental symmetric (S0) and fundamental antisymmetric (A0) modes propagate over the entire frequency–thickness range, and by increasing the frequency–thickness product, the number of propagating modes (called higher-order modes) increases.

The complexity of the mode shapes increases with the increasing mode number [17, 42, 57]. The schema of the first three modes is shown in Figure 7.

a)
Symmetric mode

b)
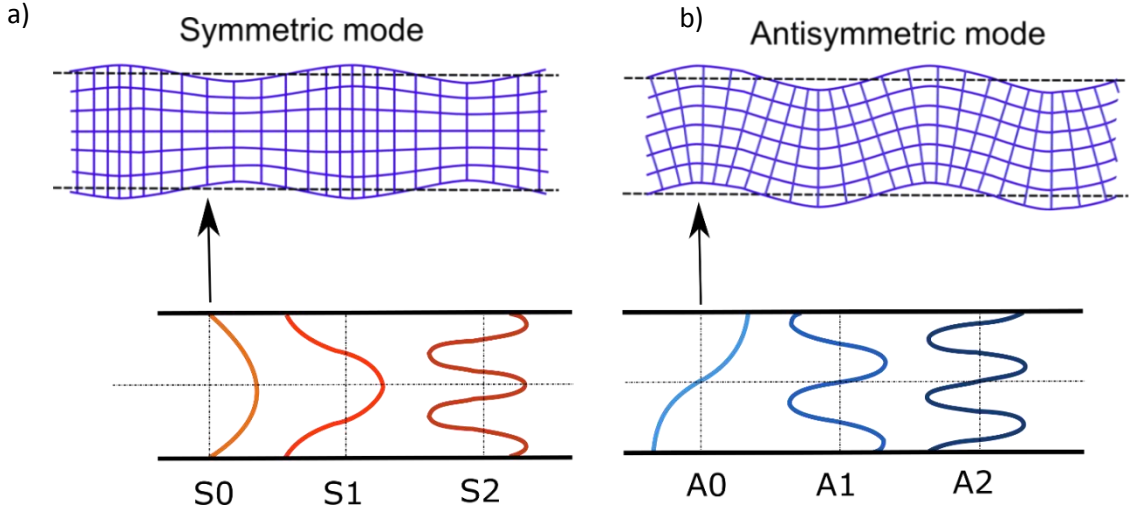Antisymmetric mode

S0   S1   S2

A0   A1   A2

Figure 7 A schema of displacement fields for the first three Lamb wave modes a) symmetric, b) asymmetric

Lamb wave behaviour depends on material characteristics. Propagation in isotropic metals and anisotropic/quasi-isotropic composites will be addressed. In isotropic materials, pure Lamb wave modes exist, and their velocity is dependent only on the frequency – thickness product. Calculation of the dispersion equation (Rayleigh – Lamb equation) provides a graphical representation in the form of dispersion curves, as seen in Figure 8.
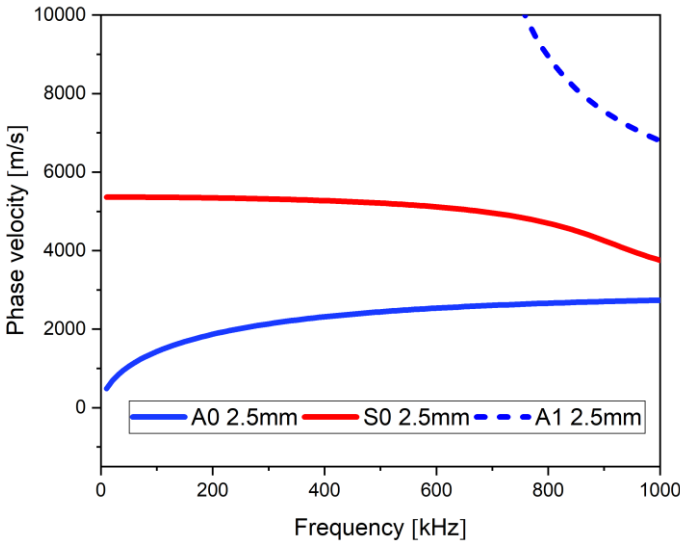
Figure 8 Example of the phase velocity dispersion curves for 2.5 mm aluminium alloy plate

The loss of pure Lamb wave modes is characteristic for composites. Therefore, they are often designated as quasi-symmetrical and quasi-asymmetrical modes. Velocity is dependent not only on the frequency-thickness product but also on the direction. Rayleigh – Lamb equation is not eligible for anisotropic materials; therefore, other methods such as the transfer matrix method (TMM), global matrix method (GMM), etc., are utilized to determine dispersion curves. Despite the anisotropic nature of composites and the necessity to use different approaches to evaluate Lamb wave propagation in composites, the overall characteristics are very similar [43].

4.2   Lamb wave generation and detection

The formation of Lamb waves has often been described using the concept of interference of back-and-forth surface reflections. This concept is based on using the ultrasonic angle beam probe, and the wave propagation behaves according to Snell's law. Incident L wave hits the interface (upper surface) at a proper angle (less than the first critical angle), and mode conversion occurs. The L wave is converted partly into the L wave and partly into the SV wave. The secondary L and SV waves are transmitted to the host structure. When the waves reach the lower surface, they refract again. An interference of reflected L and SV waves occurs, resulting in Lamb wave propagation (Figure 9). The relationship between phase velocity and the incident angle is covered in Snell's law. Therefore, the frequency can be plotted against phase velocity or incident angle [17].
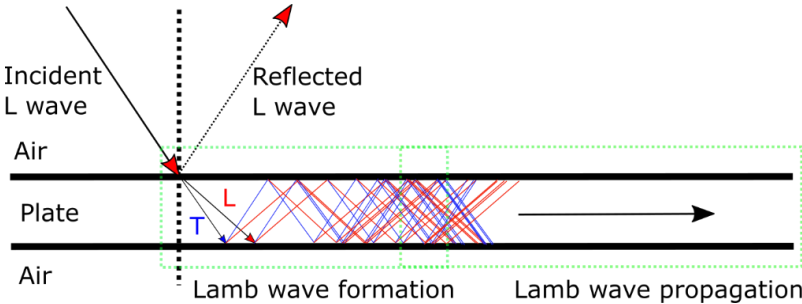
Figure 9 Lamb wave generation using angle beam ultrasonic probe

Other physical principles have been proved to work regarding Lamb wave generation and detection. Short laser pulse has been used to generate Lamb waves through the thermoelastic event. Scanning laser Doppler vibrometer (SLDV) has been exploited for Lamb wave detection, mainly by the whole wavefield imaging [59]. Other non-contact device exploiting a laser induced plasma shock was utilized to generate Lamb waves [60]. Laser shearography

(LS) has also been utilized, and even the interaction with delamination has been imaged [61]. Nevertheless, SHM principles imply permanently attached actuator/sensors to the structure. Piezoelectric wafer active sensors (PWAS) are small, lightweight, non-invasive, and perfectly satisfy SHM conditions to generate and sense Lamb waves. PWAS are usually made of conventional lead zirconate titanate (PZT); however, piezopolymers with certain limitations (temperature) were also developed and used. Variability also stands in shapes and sizes. Square and circular PWAS show identical omnidirectional wavefields at far enough distances; however, square PWAS (high ratio of length/width) may excite unidirectional patterns. The electrode placement and material characteristics (piezoelectric coefficients) indicate the vibration mode. There are two ways of using PWAS for Lamb wave generation. PZT disc with a wrap-around electrode, which enables the soldering of both contacts on the top transducer surface is a simple and useful variant. Another option is embedded technology as SMART Layer® system (Acellent) or DuraAct (PI), which consists of the extremely thin dielectric film with an array of durable, networked piezoelectric sensors [67].

4.3 Piezoelectric wafer active sensors (PWAS)

Much research on this topic has been done by Giurgiutiu [2, 64, 65, 66]. The way of elastic wave excitation is fundamentally different from that of using standard ultrasonic transducers. Ultrasonic probes apply vibrational pressure to the surface through surface tapping. Generally, the PWAS are strain coupled with the structure by the surface pinching. Expansion and contraction of the PWAS induced by the applied voltage are transmitted to the structure through the bonding layer, which acts predominantly in shear. The shear-lag analysis indicated that as the bonding layer thickness decreases, the shear transfer becomes concentrated at the ends of the PWAS. PWAS ends are stress-free; therefore, the build-up of strain takes place at the edges of the actuator. An ideal bonding is considered a bonding layer of 1μm, where maximum shear stress is transmitted to the host structure [65]. The concept of ideal bonding leads to the pin force model, which considers that all the load transfer takes place at the edges of the actuator [66].
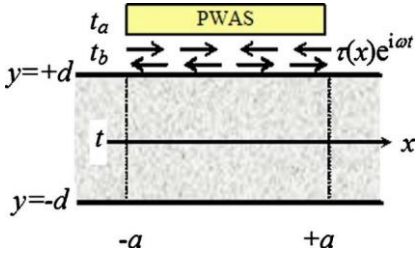

Figure 10 Model of a shear layer interaction between the sensor and the structure [64]

Complex wave propagation makes Lamb wave evaluation difficult. Selective generation of either symmetric or asymmetric mode using PWAS is of great interest. One way is to exploit Lamb wave tuning using PWAS. Interaction of PWAS and the host structure showed that the amplitude of both the fundamental modes changes with frequency. At some frequencies (actually, wavelengths), S0 and A0 are enhanced or suppressed. The strain and displacement wave solutions under PWAS excitation for ideal bonding conditions were derived by Giurgiutiu. Theoretically, maximum excitation and detection are achieved when the PWAS length (diameter) is an odd multiple of the half wavelength of a particular Lamb wave mode. Even multiples of the wavelength compared to the PWAS length cause mode minima [66]. The PWAS length is crucial for the wavelength tuning as well as the tested structure. The example of the amplitude tuning of the 7mm PWAS disc is illustrated in Figure 11. The maximum amplitude of A0 mode is at 90 kHz. Based on dispersion curves, the group velocity is around 1250 m/s which corresponds to the wavelength of 13.8 mm. The first odd multiple of the half wavelength 1×6.9 mm corresponds to the PWAS diameter (7 mm). In fact, the mode cannot be suppressed completely up to the zero amplitude, due to the signal bandwidth [63].
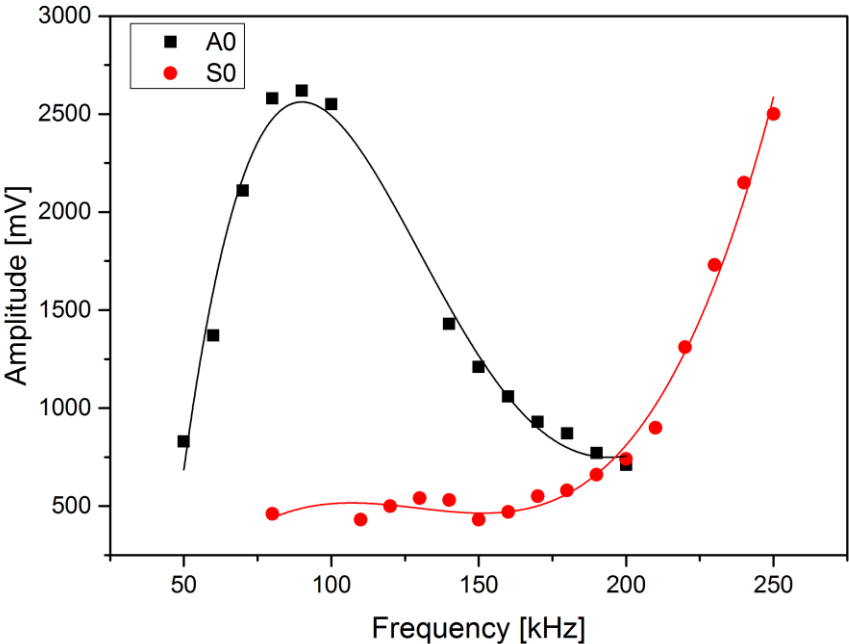
Figure 11 Relation of the frequency and the corresponding amplitude of the A0 and S0 mode

Another way is to use two symmetrically placed transducers on both parallel surfaces. In-phase actuation generates symmetrical mode only, while out of phase actuation generates asymmetrical mode. However, access to both monitored surfaces must be ensured, and the equipment must be adequately adapted for simultaneous excitation.

The structure flaws may influence the symmetry/asymmetry of the given mode. It is desirable to choose the frequency when the amplitude of one mode (sensitive to the flaw) is enhanced and the other suppressed. However, there are more factors to choose the proper frequency and mode apart from the amplitude ratios. The important aspect is the type of the considered flaw, which is sensitive to different wave mode characteristics. Therefore, the knowledge of the wave structure and dispersion curves combined with PWAS tuning might be helpful to choose the suitable frequency for testing. In general practice, the fundamental S0 and A0 modes are used. S0 mode is much less dispersive and sensitive to flaws anywhere within the thickness. On the other hand, the A0 mode shows great sensitivity to surface cracks and corrosion [105]. The shorter wavelength of the A0 mode also enables smaller defects detection.

4.4   Mathematical description of Lamb wave propagation in isotropic media

Two approaches have often been used to solve a free plate problem—the method of potentials or partial wave technique. The first one can be used only to solve isotropic plates, while the partial wave technique obtains solutions also for anisotropic structures. The method of potentials eventually leads to the Rayleigh – Lamb dispersion relation, which serves as the fundamental equation for Lamb wave propagation in isotropic media. Therefore, significant parts of the procedure of equation derivation are shown to demonstrate the characteristic features [61, 66].

Vector notation of displacement equation of motion for continuum mechanics:

$$\mu\nabla^2 u + (\lambda + \mu)\nabla\nabla u = \rho\ddot{u} \tag{19}$$

Where u denotes displacement, λ and μ are Lame constants, ϱ is density, ∇ and ∇^2 are Nabla and Laplace operators, respectively.

Lamé constants can be expressed based on the Young modulus E and Poisson's ratio ν:

$$\lambda = \frac{E - \nu}{(1 + \nu)(1 - 2\nu)} \tag{20}$$

$$\mu = \frac{E}{2(1 + \nu)} \tag{21}$$

According to the theorem of vector calculus – Helmholtz decomposition – a vector field can be decomposed into two parts. Displacement u is decomposed into scalar and vector potentials φ and ψ, respectively:

$$u = \nabla\varphi + \nabla \times \psi \tag{22}$$

Where $\nabla\varphi$ is divergence and $\nabla \times \psi$ is the rotation of a vector field. In other words, one displacement field does not rotate, and the other has zero divergence. Therefore, one is linked to the longitudinal and the other to the transversal displacements.

The problem is under the condition of plain strain (independent on x_2); therefore, derivatives ∂x_2 vanish. Decomposed equation (22) is in the following form:

$$u_1 = \frac{\partial\varphi}{\partial x_1} + \frac{\partial\psi_3}{\partial x_2} - \frac{\partial\psi_2}{\partial x_3} \quad \rightarrow \quad u_1 = \frac{\partial\varphi}{\partial x_1} - \frac{\partial\psi_2}{\partial x_3} \tag{23}$$

$$u_2 = \frac{\partial\varphi}{\partial x_2} + \frac{\partial\psi_1}{\partial x_3} - \frac{\partial\psi_3}{\partial x_1} \quad \rightarrow \quad u_2 = \frac{\partial\psi_1}{\partial x_3} - \frac{\partial\psi_3}{\partial x_1} \tag{24}$$

$$u_3 = \frac{\partial\varphi}{\partial x_3} + \frac{\partial\psi_2}{\partial x_1} - \frac{\partial\psi_1}{\partial x_2} \quad \rightarrow \quad u_3 = \frac{\partial\varphi}{\partial x_3} + \frac{\partial\psi_2}{\partial x_1} \tag{25}$$

In plane displacements u_1 and out of plane displacement u_3 are based on the potentials φ and ψ_2, which are linked to the longitudinal and shear vertical waves (forming Lamb modes), respectively. Potentials ψ_1 and ψ_3 in u_2 indicate shear horizontal motion (SH modes). Further, only Lamb modes will be addressed.

Substitution (22) into the (19) result into the form:

$$\nabla[(\lambda + 2\mu)\nabla^2\varphi - \rho\ddot{\varphi}] + \nabla \times [\mu\nabla^2\psi - \rho\ddot{\psi}] = 0 \tag{26}$$

The solution yields for the longitudinal and shear waves, respectively, if the displacement field is curl-free or divergence-free. Two independent wave equations are obtained for the potentials φ and ψ:

$$\nabla^2\varphi = \frac{1}{c_L^2}\ddot{\varphi} \tag{27}$$

$$\nabla^2\psi = \frac{1}{c_T^2}\ddot{\psi} \tag{28}$$

The solution for the wave equations is assumed harmonic and represent standing waves across the thickness in the x_3 direction and traveling waves along the x_1 direction:

$$\varphi = \varphi(x_3)exp[i(kx_1 - \omega t)] \tag{29}$$

$$\psi = \psi(x_3)exp[i(kx_1 - \omega t)] \tag{30}$$

Substitution of the assumed solution to the wave equations (27, 28) results in the following:

$$\varphi(x_3) = A_1 \sin(px_3) + A_2 \cos(px_3) \tag{31}$$
$$\psi(x_3) = B_1 \sin(qx_3) + B_2 \cos(qx_3) \tag{32}$$

where p, q, and k are defined as follows:

$$p^2 = \frac{\omega^2}{c_L^2} - k^2 \tag{33}$$
$$q^2 = \frac{\omega^2}{c_T^2} - k^2 \tag{34}$$
$$k^2 = \frac{\omega^2}{c_p^2} \tag{35}$$

where c_L, c_T, c_P, k, ω, d denote velocities of longitudinal and transverse waves, phase velocity, wavenumber, angular frequency, and plate thickness, respectively.

Displacement u_1 and u_3 become:

$$u_1 = (ik[A_1 \sin(px_3) + A_2 \cos(px_3)] - [qB_1 \cos(qx_3) - qB_2 \sin(qx_3)])exp[i(kx_1 - \omega t)] \tag{36}$$
$$u_3 = ([pA_1 \cos(px_3) - pA_2 \sin(px_3)] + ik[B_1 \sin(qx_3) + B_2 \cos(qx_3)])exp[i(kx_1 - \omega t)] \tag{37}$$

Displacement equations contain sine and cosine terms which are odd and even functions, respectively:

$$\sin(-x) = -\sin(x) \tag{38}$$
$$\cos(-x) = \cos(x) \tag{39}$$

The distinction between symmetrical and asymmetrical modes is based on the displacement field direction according to Figure 12.
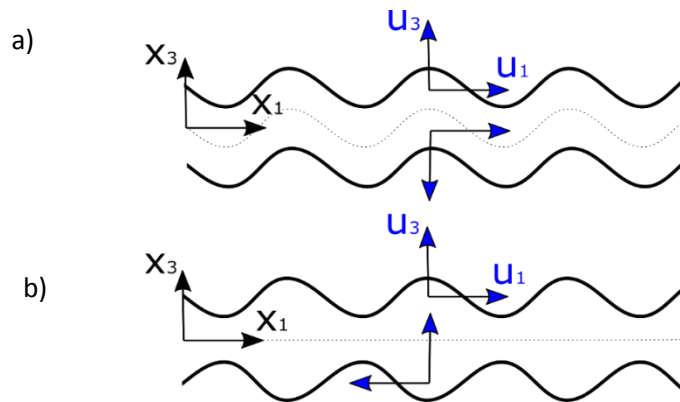
Figure 12 Displacement components of the fundamental Lamb wave modes a) asymmetric mode, b) symmetric mode

Symmetric mode:

$$u_1(x_1, x_3) = u_1(x_1, -x_3) \tag{40}$$
$$u_3(x_1, x_3) = -u_3(x_1, -x_3) \tag{41}$$

Antisymmetric mode:

$$u_1(x_1, x_3) = -u_1(x_1, -x_3) \tag{42}$$
$$u_3(x_1, x_3) = u_3(x_1, -x_3) \tag{43}$$

The motion is symmetrical with respect to the midplane if u_1 contains cosines and u_3 sines, while the motion is asymmetrical if u_1 contains sines and u_3 cosines. Exploiting odd and even properties of goniometric functions for symmetrical and asymmetrical modes result in the following displacement equations:

Symmetric mode:

$$u_1 = [ikA_2 \cos(px_3) - qB_1 \cos(qx_3)] \, exp[i(kx_1 - \omega t)] \tag{44}$$
$$u_3 = [-pA_2 \sin(px_3) + ikB_1 \sin(qx_3)] \, exp[i(kx_1 - \omega t)] \tag{45}$$

Asymmetric mode:

$$u_1 = [ikA_1 \sin(px_3) + qB_2 \sin(qx_3)] \, exp[i(kx_1 - \omega t)] \tag{46}$$
$$u_3 = [pA_1 \cos(px_3) + ikB_2 \cos(qx_3)] \, exp[i(kx_1 - \omega t)] \tag{47}$$

Displacement equations are used for the stress equations given by:

$$\sigma_{31} = \mu(u_{3,1} + u_{1,3}) \tag{48}$$
$$\sigma_{33} = \lambda(u_{1,1} + u_{3,3}) + 2\mu u_{3,3} \tag{49}$$

Stress equations become:

Symmetric mode:

$$\sigma_{31} = \mu[-2ikpA_2 \sin(px_3) - (q^2 - k^2)B_1 \sin(qx_3)] \, exp[i(kx_1 - \omega t)] \tag{50}$$
$$\sigma_{33} = \mu[-(q^2 - k^2)A_2 \cos(px_3) + 2ikqB_1 \cos(qx_3)] \, exp[i(kx_1 - \omega t)] \tag{51}$$

Asymmetric mode:

$$\sigma_{31} = \mu[2ikpA_1 \cos(px_3) + (q^2 - k^2)B_2 \cos(qx_3)] \, exp[i(kx_1 - \omega t)] \tag{52}$$
$$\sigma_{33} = \mu[-(q^2 - k^2)A_1 \sin(px_3) - 2ikqB_2 \sin(qx_3)] \, exp[i(kx_1 - \omega t)] \tag{53}$$

Boundary conditions for the free surfaces are:

$$\sigma_{31} = \sigma_{33} = 0 \text{ for } x_3 = +/-d \tag{54}$$

The resulting output is in the form of a homogeneous equation system in the matrix notation:

Symmetric mode:

$$\begin{bmatrix} -2ikpsin(pd) & (q^2 - k^2)\sin(qd) \\ -(q^2 - k^2)\cos(pd) & 2ikqcos(qd) \end{bmatrix} \begin{bmatrix} A_2 \\ B_1 \end{bmatrix} = \begin{bmatrix} 0 \\ 0 \end{bmatrix} \tag{55}$$

Asymmetric mode:

$$\begin{bmatrix} 2ikpcos(pd) & (q^2 - k^2)\cos(qd) \\ -(q^2 - k^2)\sin(pd) & -2ikqsin(pd) \end{bmatrix} \begin{bmatrix} A_1 \\ B_2 \end{bmatrix} = \begin{bmatrix} 0 \\ 0 \end{bmatrix} \tag{56}$$

Adjusting the systems of equations lead to the solution in the form of the Rayleigh-Lamb equation:

Symmetric mode:

$$\frac{\tan(qd)}{\tan(pd)} = \frac{4k^2pq}{(q^2 - k^2)^2} \tag{57}$$

Asymmetric mode:

$$\frac{\tan(qd)}{\tan(pd)} = \frac{(q^2 - k^2)^2}{4k^2pq} \tag{58}$$

The symmetric/asymmetric solution is calculated for three variants based on the expected region of c_P. In the symmetric and asymmetric model, c_P may lie in different intervals with respect to the c_L and c_T. Therefore, six equations need to be evaluated to find roots for both models. The number of modes increases with increasing frequency.
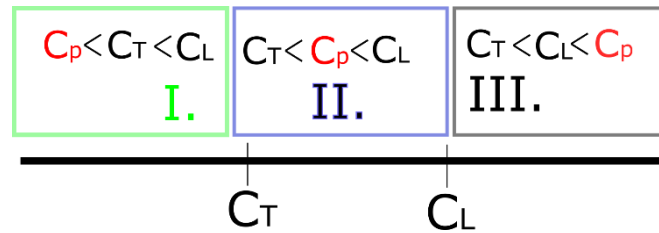
Figure 13 Three possible intervals for c_P

The following designations of p and q result according to Figure 13 and equation (58):

1. If the c_P lies in the region I., then p and q are imaginary
2. If the c_P lies in region II., then p is imaginary, and q is real
3. If c_P lies in region III., then p and q are real

Based on p and q the relation $i\tan(ix)=\tanh(x)$ is exploited.

Determination of three variants of the Rayleigh-Lamb equation for both models (symmetric and asymmetric) enable dispersion curves calculation for the whole frequency spectra. However, the calculation can be performed only numerically. The resulting plot is usually in the form of circular frequency - wavenumber (ω-k) or frequency – phase velocity (f- c_P) (Figure 14a and Figure 14b, respectively).
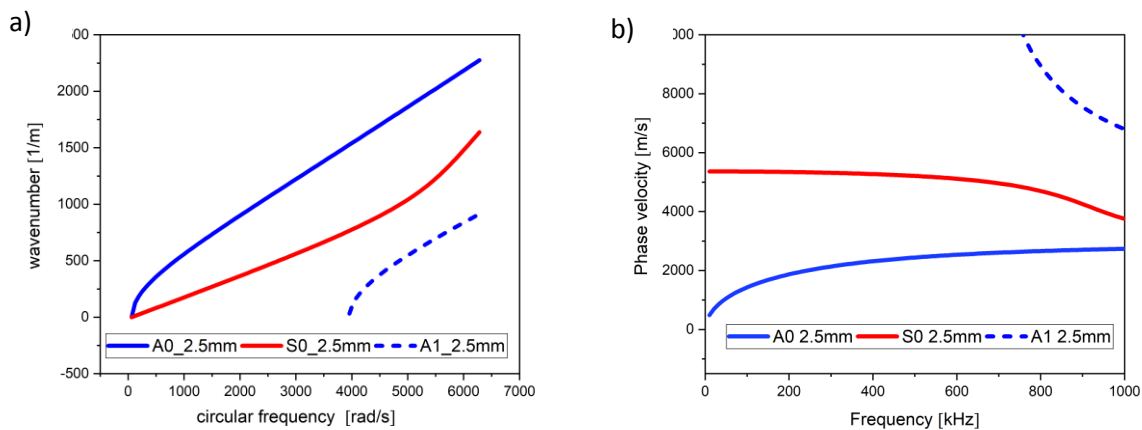
Figure 14 Dispersion curves a) wavenumber – circular frequency representation, b) phase velocity – frequency representation

The calculation is performed for the given frequency according to the following steps:

1. Use constants c_L and c_T and half thickness of the plate d
2. Choose the frequency $f \rightarrow \omega = 2\pi f$
3. Choose c_P
4. Use the corresponding variant of the Rayleigh-Lamb equation
5. Evaluate the equation: LHS-RHS=0
6. Based on the sign of the resulting number, choose another c_{P+1} or c_{P-1} until the sign changes
7. Repeat the steps 2-6 for the required frequencies

4.5 Dispersion

Dispersion is considered a dependency of a physical quantity on the frequency and is a key feature of Lamb waves. The dependency of the wave velocity and attenuation on the frequency are particularly observed. Velocity dispersion was quantitatively introduced in the previous subchapter using the dispersion relation in the form of the Rayleigh-Lamb equation. Each wavelength (frequency component) propagates with a different velocity. In practical applications, an actuation pulse has a certain frequency bandwidth +/- Δf around the central frequency. Therefore, a group of waves that travel together at similar frequencies, but varying velocities form a wave packet. Group velocity c_g is the term given to the propagation velocity of a wave packet, while with the phase velocity c_P propagate individual waves. As a result, shape distortion occurs - the propagating pulse changes shape with the increasing propagating distance [68]. The difference between non-dispersive and dispersive wave packets is shown in Figure 15a. The superposition of two waves with slightly different frequencies is shown in Figure 15b.
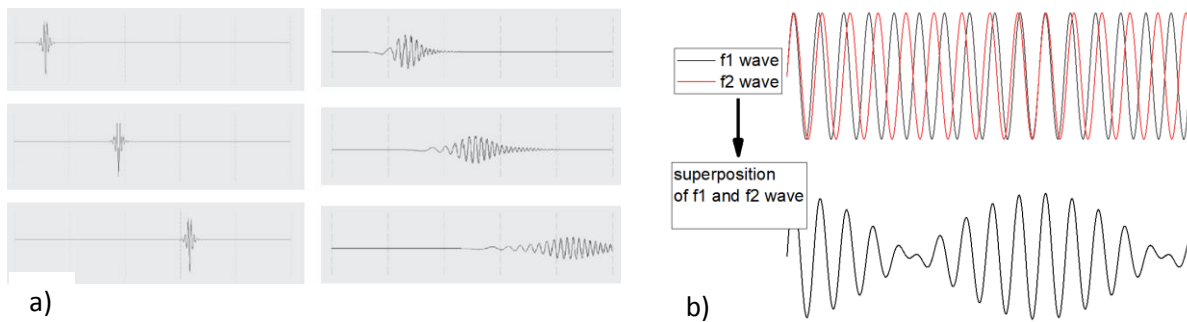
Figure 15 a) comparison between the non-dispersive and dispersive burst [68], b) superposition of waves into a wave packet

Experimentally, the group velocity is measured by tracking the envelope of the wave packet since the phase is "hidden" in the wave packet. Calculations are performed exploiting the dispersion relation. Rayleigh – Lamb dispersion equation evaluates not only the frequency-dependent phase velocities but also the structure thickness. Dispersion curves are, therefore, relationships of c_P (c_g) and the frequency-thickness product.

The construction of velocity dispersion curves is an effective way to describe Lamb waves. Usually, dependencies ω-k or c_P-f (c_g-f) are plotted. Rayleigh - Lamb equation directly gives the variable k or c_p for the given ω. Phase velocity is calculated as:

$$c_p = \frac{\omega}{k} \tag{59}$$

Group velocity is recalculated according to the following:

$$c_g = \frac{d\omega}{dk}$$ (60 a)

$$c_g = d\omega \left[\frac{d\omega}{c_p} - \omega \frac{dc_p}{c_p^2} \right]^{-1}$$ (60 b)

$$c_g = c_p^2 \left[c_p - \omega \frac{dc_p}{d\omega} \right]^{-1}$$ (60 c)

There are three cases of dispersion based on the relationship of c_P - c_g [68].

1. If $c_P = c_g$
    - Waves with constant velocity across the whole frequency spectrum (e.g., L, T waves)
    - Linear relation of ω-k
    - Non-dispersive behaviour
2. If $c_P < c_g$
    - Increasing trend of ω-k
    - Anomalous dispersion
3. If $c_P > c_g$
    - A decreasing trend of ω-k
    - Classical dispersion

Graphical representation of ω-k in Figure 16a shows the difference in c_P and c_g calculation. Group velocity is related to the tangent while phase velocity to the slope. Figure 16b shows the difference of c_P and c_g for the case of A0 mode up to 250 kHz.
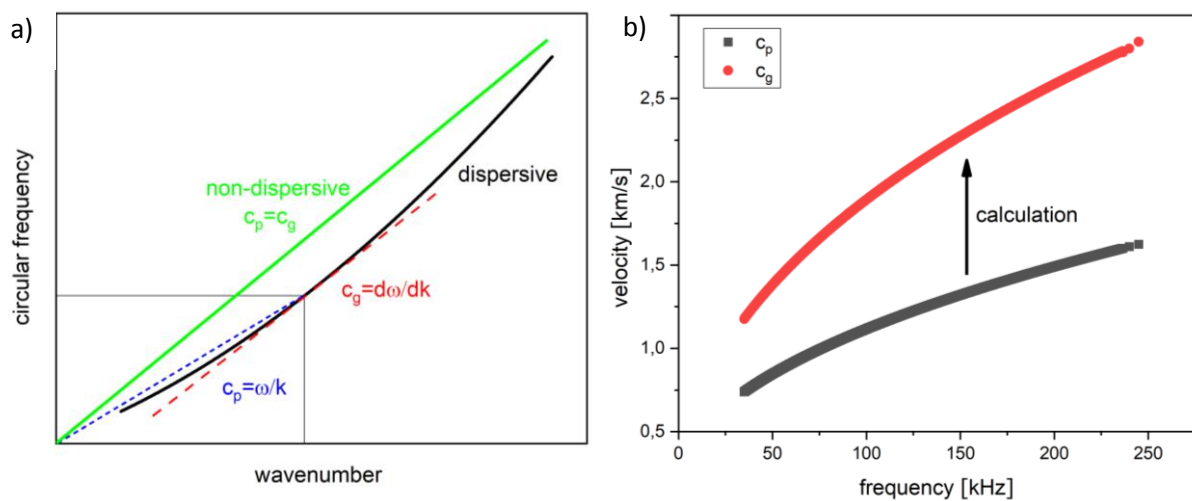
Figure 16 a) Wavenumber – circular frequency plots, b) phase and group velocity plot

Dispersive characteristics of the propagating modes vary across the frequency-thickness range for both modes. Figure 17 shows the difference between the dispersive A0 and almost non-dispersive S0 mode at 100 kHz. The plot is constructed based on experimental signals collected by PZT sensors at several equidistant points. Phase and group velocity may be distinguished by tracking the specific part of the wave packet. In the case of S0, both velocities are identical, unlike in the case of A0.
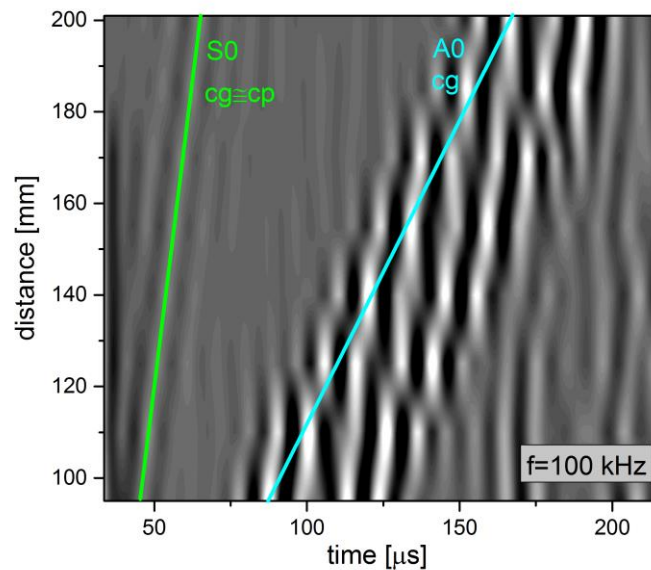
Figure 17 Experimental data collected at several equidistant points – the difference in dispersive (A0) and non-dispersive (S0) wave packet

4.6   Propagation in anisotropic media

As mentioned before, the loss of pure Lamb wave modes occurs in composites. While in isotropic materials, it is assumed that Lamb waves are formed by interference of L and SV waves, in anisotropic structures are formed by superpositions of reflected L, SV, and SH partial waves [70].

Lamb waves in anisotropic materials such as composites show not only velocity dispersion in relation to the frequency-thickness product. Velocity and amplitude vary with the propagation direction. The stiffness depends on the fibre orientation, hence the overall layup, and the velocity is directly linked to the stiffness. Therefore, in unidirectional composites, the velocity is more sensitive to the propagation angle than in quasi-isotropic composites. Also, the velocity of S0 mode is much more sensitive to the layup than the A0 mode. The mechanical

properties of composites are also influenced by the quality of the manufacturing process. The inner porosity (voids) is a very common issue. Therefore, the velocity may also vary with the location within the same direction [69].

The derivation of dispersion relations starts with the appropriate equation of motion, stress-strain relationships, and definition of boundary conditions. The solution is provided utilizing either the method of potentials or the partial wave technique. For the isotropic case, both techniques lead to Rayleigh – Lamb equation. However, for composites Rayleigh – Lamb equation cannot be used for dispersion curves construction anymore since Helmholtz decomposition does not provide the desired simplification. Therefore, the partial wave technique is utilized to derive dispersion relations in anisotropic structures. In a single anisotropic layer, a plate wave may be understood as a superposition of 6 partial waves – 2 quasi longitudinal (+/- L), 2 quasi shear – vertical (+/- SV), and 2 quasi shear – horizontal (+/- SH) [70]. The sign denotes the propagation direction (reflection from the top or the bottom surface). Complete analytical derivation of dispersion relations for Lamb type and SH waves can be found, for example, in [43, 58, 70]. Extension to the multi-layered structures is based on the assembly of the boundary conditions carried out by the Global matrix method (GMM) or Transfer matrix method (TMM). GMM approach may utilize the Helmholtz decomposition for the isotropic layers or the partial wave technique for both isotropic and anisotropic layers. The number of boundary conditions that need to be satisfied corresponds to the number of layers (2 boundary conditions for the top surface, 2 for the bottom surface, and 4 for each interface). For the 4 – layer structure, the matrix 16 × 16 need to be solved. This approach is evidently not suitable for structures with a large number of layers due to the high time consumption. TMM approach can be helpful since the transfer matrix (4 × 4) is independent on the number of layers. However, this method is unstable for large frequency–thickness products. To solve this problem, stiffness matrix method (SMM) was evolved from the TMM [43].

As an alternative approach to TMM/GMM a semi-analytical finite element (SAFE) method was developed to evaluate plate wave propagation. It is considered a hybrid method since the waveguide is discretized in the cross-section, and analytical solution (harmonic exponential term) is adopted in the wave propagation direction. The SAFE provides an advantage over matrix-based methods because they need to perform root searching in the complex domain and thus being more computationally expensive, and root-finding algorithms may miss certain roots [62].

4.7 Propagation in complex structures

Lamb wave propagation in complex structures is much more complicated compared to flat plates. In complex structures made of anisotropic materials, the fastest path between two points is not necessarily a straight line; hence, the shortest path may not be the fastest path [69].

Another difficulty arises from the mode conversion effect. A symmetrical mode may be converted into an asymmetrical one when reaching structural change (discontinuity, thickness change, shape change, etc.) or damage. The first wave packet propagates the fastest S0 mode and the last the slower A0 mode. In between, converted A0 can be distinguished. However, real structures have boundaries, and multiple edge reflections can distort the particular wave packets and disable mode distinction [19]. In multi-layered composite plates, continuous mode conversion has been observed. S0 mode converts into the A0 mode without passing any discontinuity. This effect was investigated numerically and experimentally using a scanning laser vibrometer [71].

4.8 Temperature dependence

Environmental and operational conditions, especially temperature, humidity, loadings, and vibrations, affect Lamb wave propagation [72]. Temperature effects may cause significant Lamb wave propagation variations in velocity and amplitude.

Longitudinal and transversal wave velocities are material constants for the given temperature and functions of temperature through the elastic modulus and density. Since Lamb waves are formed by portions of longitudinal and transversal displacements, symmetrical and asymmetrical modes are consequently temperature dependent as well. Generally, material stiffness decreases with increasing temperature, and so does the Lamb wave propagation velocity. Structure geometry in terms of in-plane expansion/compression may also influence the thickness and the actuator–sensor distance. Apart from the velocity, characteristics of PZT sensors as dielectric permittivity and piezoelectric coefficients change as well. Temperature variations also affect the material characteristics of the bonding layer between the actuator and the tested structure [72]. Substantial analyses of all temperature-dependent parameters (mechanical and electrical) of SHM system utilizing PZT sensors was published in [73]. Several publications have appeared documenting the temperature influence on Lamb wave propagation velocity. A decrease in ToF with decreasing temperature was documented within many publications. These investigations naturally lead to the decrease of the phase and group

velocities with increasing temperature [74, 75, 76]. However, experiments performed above 140 °C revealed a velocity increase [77]. The thermal dependency of Lamb wave velocity on the temperature is essential since ToF change is often used as a damage-sensitive parameter. Then, the temperature effect needs to be compensated, or identical environmental conditions need to be ensured. Temperature-affected signal responses may cause false alarms in damage detection algorithms. Therefore, compensation algorithms have been widely investigated, namely optimal baseline selection (OBS) and baseline signal stretch (BSS) or their combination [78, 79, 80].

4.9   Nonlinear effects

The exact frequency of the received and actuated signal is described by linear ultrasonics. Microstructural changes cause nonlinear elasticity, and therefore, higher harmonics can be generated. Nonlinear ultrasonics in bulk solids has been studied for more than four decades, but the initial studies of higher harmonics in plates are much more recent. Sensitivity to microstructural changes is considered a great advantage of nonlinear methods [81]. Nonlinear effects caused by fatigue cracks in metals have been studied extensively. There are also some publications dealing with nonlinear effects in composites.

In linear systems, the actuated frequency stays unchanged during the propagation within the structure. However, microstructure inhomogeneities (voids, dislocations, etc.) may cause nonlinear effects such as higher harmonics generation or subharmonic generation. The propagating wave is distorted, which is not fully visible in the time domain, but the frequency domain reveals the higher harmonics.

Material nonlinearities at the microstructure level act as a source of higher harmonics generation. The second harmonic Lamb waves may grow cumulatively as they propagate if precise conditions are satisfied. The phase and group velocity matching and non-zero power flux are conditional. Therefore, dispersion curve construction is essential [82]. Actuation frequency is selected, so the fundamental and the double frequency propagate with identical velocity. This condition shifts the selection to higher frequency ranges. The wave pairs often correspond to S1 – S2 modes. Higher harmonic wave is always symmetrical regardless of the fundamental wave mode [82, 83]. The comparison of the frequency selection of S0 mode, which satisfies and does not satisfy the matching condition, is described in the literature [84].

Higher harmonics generation may also be caused by the contact type of damages such as fatigue cracks or even delamination. In the case of the fatigue crack, the phenomenon of contact acoustic nonlinearity (CAN) is described by the breathing crack [85]. The compression part of

the incident Lamb wave closes the crack while the tension part opens. Nonlinearity is caused by the clapping behaviour of the crack surfaces [86]. The advantage of this approach lies in the possibility of using low-frequency Lamb waves.

Quantification of the nonlinearity feature is performed using the nonlinearity factor. The simplified form of the relative nonlinearity parameter represents the ratio of amplitudes of the corresponding waves [87]:

$$\beta = \frac{A_2}{A_1^2} \tag{61}$$

Recently, experimental studies supported by simulations focusing on delamination induced higher harmonics generation due to CAN have been published [88, 89]. S0 mode is much more effective for evaluation than A0 mode.

5 State of the art: literature review in relation to experiments

The literature review is focused primarily on the experimental investigation of damage detection in typical composite aircraft structures. Therefore, this chapter deals mainly with two topics - dispersion curve determination and damage detection process. Specifically, impact damage detection and debonding detection in adhesively bonded joints are covered in this section.

5.1 Dispersion curves determination

Velocity dispersion curves together with amplitude-frequency PWAS tuning provide unique information for the given structure and enable the identification of the measured wave packets. Dispersion curve calculations are validated by experimental measurements. For isotropic materials, calculations are performed by means of the Rayleigh-Lamb equation. Calculations for anisotropic layered structures are much more complex and utilize methods such as TMM, GMM, SMM, and SAFE [62, 90]. There are available SWs for dispersion curve determination, even for complex anisotropic structures as composite bonded joints. A Demo version of the SW DISPERSE with limited functions is provided by Lowe utilizing the GMM approach. There is also SW GUIGUW (Graphical User Interface for Guided Ultrasonic Waves) under development, providing a year-term license key that enables not only velocity dispersion curves calculation for isotropic/anisotropic structures but displays also wave structure curves. GUIGUW SW is based on the SAFE method [91]. Dispersion curves calculation for the isotropic structures (single-layered or multi-layered) is performed using either the c_L and c_T and density constants or material properties as Young modulus and Poisson. Input data for solving the anisotropic cases comprise the stiffness matrix for each layer.

As stated before, velocity dispersion curves represent a basic description of Lamb wave behaviour. The group velocity dispersion curve can be determined by the phase velocity recalculation using eq (60c). The trend of the wavenumber – circular frequency plots show the mutual relation of the phase and group velocity ($c_P > c_g$, $c_P < c_g$, $c_p = c_g$).

Experimental measurements may bring direct or indirect information about the phase and group velocity; hence signal processing tools need to be exploited. Mostly, actuated frequencies are chosen within the lower frequency-thickness range, where only the fundamental modes are present. Then, dispersion curves are constructed up to the first cut-off frequency. S0 mode is in the low frequency-thickness range much less dispersive than A0

mode, so A0 mode velocity determination is much more complicated. The group velocity of S0 mode is for the low frequency-thickness products almost identical with the phase velocity.

The standard way to obtain velocity is to define ToF between two close points of a known distance. For wave packets measured experimentally, phase velocities are measured by tracking wave peaks while the group velocity by tracking envelopes of wave packets [92]. The amplitude of different peaks might change due to dispersion with propagation distance, causing the change of the shape of the wave packet. Wave packets envelopes or peaks itself should not be distorted to be compared [17]. However, signal processing tools are often exploited since the distortion occurs often. Simple ToF difference or cross-correlation function is then used to determine the time lag. Information about the arrival time can also be extracted using Wavelet transform [92, 93, 94]. According to the literature [95], knowing the distance, time, and phase between 2 close signals, both phase and group velocity can be determined. First, the wave packets are extracted from the rest of the signal. Hilbert transform is used to obtain envelopes that are cross correlated to determine the time difference and the group velocity. Then, a phase shift that maximizes the correlation is found to calculate the phase velocity. Another precise method to determine dispersion curves is 2D FFT [31]. Discrete 2D FT is a quick tool to determine dispersion curves in a wavenumber–frequency domain. However, a high number of time signals at equidistant points is required. Therefore, this method is suitable for measurements obtained using laser interferometry or the ultrasonic receiver, which enables scanning along the desired path or for numerically gained data. Time-frequency analysis using short-time chirp- FT to determine both velocities exploiting only two close sensors has been proposed in [96]. The spectrum decomposition technique [97, 98] is described as a fast method since velocity values in a particular frequency range are obtained using the frequency spectrum decomposition of a single wave packet. A broadband excitation signal is transmitted, and different bandwidth filters (20-130 kHz) are applied to signals at two positions. The optimal bandwidth filter is considered the one with the least relative error of the theoretical and experimentally determined group velocity. Zero crossing technique together with spectrum decomposition [99] can be utilized to identify time delays for the corresponding phases. Two close transducers are utilized so the wave distortion due to the dispersion is not significant. A threshold level is defined at particular half periods, and the time where the signal crosses zero is registered. The frequency corresponds to the half periods, and phase velocity dispersion curves can be successfully reconstructed.

5.2 Lamb wave-based damage detection

Many different approaches and algorithms for damage detection, localization, identification, and quantification of aerospace structures have been presented by means of Lamb waves. These approaches reflect the Lamb wave behaviour. Wave propagation is dependent not only on the structure design and material properties but also on actuation signal parameters (frequency, actuation signal type, input voltage) and can be influenced by changing environmental conditions (temperature, humidity) and operational conditions (loading, vibrations) [72]. Identical conditions shall be ensured, or these effects shall be compensated to avoid false alarms or damage localization errors.

Interaction with damage depends on the propagating mode and varies with the size and type of damage. Wave ridge deflections, velocity changes of propagating modes, or wave scattering due to the presence of damage were many times visualized by numerical simulations and experiments. Experimentally, full wave-field images can be obtained employing scanning laser Doppler vibrometer (SLDV) [59]. Laser shearography (LS) has also been utilized for Lamb wave imaging [61]. Neither SLDV nor LS systems can be unlike PZT sensors considered for SHM, but they are very beneficial tools to understand Lamb wave propagation and interaction with damage.
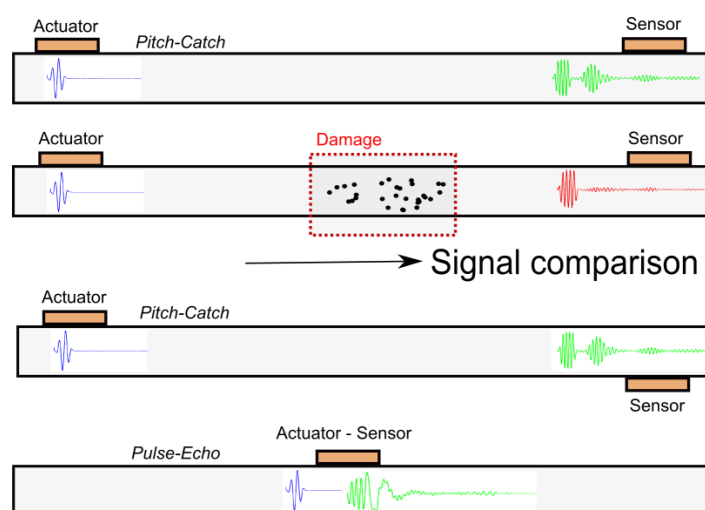
Figure 17 Common actuator - sensor configuration

The typical arrangement of the sensors utilizes pitch-catch or pulse-echo configuration (Figure 17). Pulse-echo mode provides ToF measurements of the damage induced scattered or reflected waves. These measurements result in damage localization and utilizing a sensor network enables even quantification. However, in complex structures is often difficult to

extract ToF feature. Pitch-catch arrangement enables to locate potential damage exploiting a network of actuator-sensor pairs. The dense the network, the more accurately localized the damage can be. Nevertheless, the overall objectives of SHM do not support the arrangement of thousands of sensors. Precise damage localization is the task of NDT. A simple sensor network with as few cables as possible is preferred (low weight is required). To overcome this issue, researchers are dealing with wireless sensor network technologies [100, 101].

The general evaluation methodology is based on the comparison of signals measured at different states. Damage indication and damage extent are defined by a damage index (DI) based on a damage-sensitive signal feature. DI can be extracted in the time-domain, frequency-domain, time-frequency-domain, or the frequency-wavenumber-domain [102].

The overall Lamb wave SHM process is performed according to the following steps:

1. Lamb wave tuning (simulations/calculations/preliminary measurements)
   - actuation frequency and damage sensitive mode determination
2. Measurements – baseline/baseline – free
3. Extraction of a signal feature (DI) and signal processing
4. The mathematical relation between the DI and the damage extent/damage imaging algorithms

The physical significance of the corresponding DI to damage should be explained. The ToF of the corresponding wave packet is a very powerful parameter often exploited as a DI. Wave propagation velocity is directly related to mechanical properties and the structure thickness; both can be evaluated by means of velocity change (ToF change). Thickness change may be caused by corrosion, icing, debonding, and even delamination. Mechanical properties expressed by material constants also showed significant change in Lamb wave velocity. It has been demonstrated that fatigue degradation and thermal damage in composites caused a decrease in Lamb wave velocity due to the stiffness degradation [103, 104]. The velocity is directly dependent on the structure temperature, so possible temperature variations shall be compensated, or identic conditions shall be ensured for all measurements. As a potential solution, baseline-free algorithms have been proposed by some researchers. A promising candidate for baseline-free damage detection is considered the concept of the time reversal process [106, 107, 108]. Input signal actuated by a sensor A is detected by a sensor B, reversed in time, and actuated back towards sensor B. If no damage is present between those two sensors, the reconstructed signal at sensor A will match the former input signal.

There are many other signal parameters to be considered as DI, e.g.: correlation coefficients, signal amplitude peak ratios, the signal sum of squared differences, discrete Wavelet transform coefficients, signal difference coefficients [105], nonlinear parameter, etc. This approach is beneficial in terms of automation. A mathematical relationship is established

between a suitable DI and damage parameter (crack length, size of impact, debonded region, etc.).

Basically, the evaluation approach is chosen according to the expected type of damage. For example, in the case of fatigue crack, a simple relationship of a crack length and DI is sufficient. In case of impact damage, an imaging algorithm is beneficial.

5.2.1 Impact damage detection

The literature on detection, localization, and quantification of barely visible impact damages (BVID) or visible impact damages (VID) shows a variety of approaches, including pattern recognition methods [109]. Full wave-field patterns and interactions with different sizes of BVID were investigated in [110] by means of numerical methods and experimentally using SLDV. Simple ToF measurements utilize pulse-echo configuration, and damage is localized based on time arrivals of damage-induced reflected waves [111]. Delay-and-sum imaging algorithm exploits residual signals (subtracted from the baseline), which are time-shifted according to the given rule, and then summed and averaged. Signals are filtered in the frequency domain to obtain individual images for different frequencies. Image fusion has also been introduced to improve localization [112]. Group velocity is conditional on calculating the corresponding time shift in the delay-and-sum algorithm. In complex structures, it may be impossible to identify the propagating mode and determine the ToF. To overcome such issues, imaging algorithms, especially probabilistic algorithms have become very popular [111]. The widely used RAPID (Reconstruction Algorithm for Probabilistic Inspection of Damage) algorithm is a tool for guided wave tomographic imaging and has been published in a variety of modifications. The pilot study is described in [113]. The experimental part was performed on several defects of an aluminium aircraft wing. Other studies followed by applying RAPID for damage detection in composites [114, 115] and by analysing and optimizing the algorithm features. The basic principle is shown in Figure 18a. The elliptical area of the actuator–sensor path (transducers in the loci) is influenced by the propagating wave packet. The effects of possible damage are expressed by the comparison between the baseline measurement and the following measurements. The final pseudo-image of damage is obtained by summation of all the effects from every possible sensor path (Figure 18). The algorithm enables to choose a variety of DIs. A comprehensive work, reported in [105], consisted of 112 impacts introduced to the full-scale door surround structure. Tests were performed on a large complex structure, and impacts were introduced not only to skin parts but also to the skin-stringer joints causing debonding. All 112 impacts were successfully detected. By introducing the Scaling Subtraction Method (SSM) the algorithm has been transformed into a baseline-free technique [116]. In the

reference [117], a comparison of the baseline-free TR approach and conventional RAPID was performed to evaluate BVID in a sandwich structure. Both fundamental modes A0 and S0 were sensitive to BVID, and both methods were successful in damage localization. Conventional RAPID showed better precision.
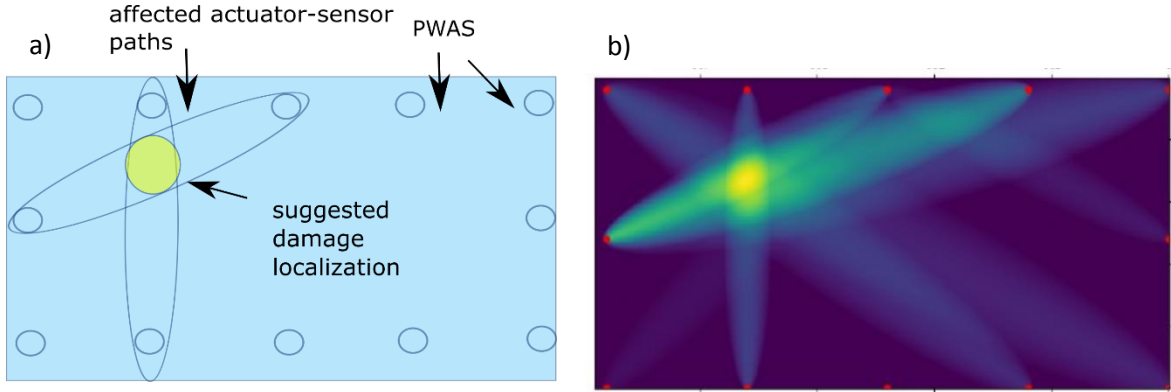
Figure 18 a) A sketch of a tomographic imaging principle, b) an example of impact damage imaging using RAPID

The theory of the RAPID algorithm is simple, as stated in [111]:

In general, the probability of damage P in location (x,y) is calculated according to the following equation:

$$P(x,y) = \sum_{i=1}^{N} DI_i \left[\frac{\beta - R_i(x,y)}{\beta - 1} \right], \tag{62}$$

Where DI_i denotes the damage index of the sensing path i and [β-R$_i$(x,y)/β-1] is a non-negative, linearly decreasing spatial elliptical distribution. β is the scaling factor that controls the size of the elliptical distribution area.

The ratio of the total distance of the point to the actuator and sensor in position (x, y) is represented by location parameter R_i.

$$R_i = \frac{\sqrt{(x-x_{1k})^2+(y-y_{1k})^2}+\sqrt{(x-x_{2k})^2+(y-y_{2k})^2}}{\sqrt{(x_{1k}-x_{2k})^2+(y_{1k}-y_{2k})^2}}, \tag{63}$$

According to a position of the evaluation point i(x,y), several cases can occur:

- If R_i (x,y) = 1, the point is on the direct line of the actuator-sensor path, and the probability of damage at that point is $Pi(x,y)=DIi(x,y)$.

- If $R_i(x,y) = \beta$, the point is on the boundary of the ellipse, and the probability of damage at that point is $Pi(x,y) = 0$.
- If $R_i(x,y) > 0$ and $R_i(x,y) < 1$, the point lies between the boundary of the ellipse and the direct line of the actuator-sensor path and the probability of damage at that point $Pi(x,y) \in (0,1)$.

DI_i represents the rate of similarity of 2 signals. The correlation coefficient ϱ is often used as a signal feature. Then, $DI_i = 1 - \varrho_i$. If two signals show no difference, correlation coefficient $\varrho_i = 1$, damage index $DI_i = 0$, and probability of damage at the given point $Pi(x, y) = 0$. The greater the difference, the smaller ϱ_i and the greater DI_i and P_i.

5.2.2 Debonding/delamination detection in adhesively bonded joints

A current challenge is the SHM of adhesively bonded composite joints: a three-layer system of adherent–adhesive–adherent. Different configurations of joints exist. Figure 19 shows a schematic of a single lap joint. From the perspective of standard NDT, more methods for the bond assessment, such as ultrasonic testing, thermography, shearography, etc., are available. Evaluation concerns damaged structure such as local delamination or complete debonding and also the bond quality. A pulse-echo technique using ultrasonic longitudinal waves is easily utilized for debonding detection. There are also commercial devices and probes (pitch-catch setup) generating Lamb waves and analysing amplitude increases within a disbonded region suitable for sandwich structures [53].

However, the current research attempts to establish a reliable real-time SHM method to ensure the integrity and reliability of adhesively bonded joints. The literature on adhesively bonded joint assessment using Lamb waves shows various approaches. Most of them are related to adhesively bonded aluminium joints, utilizing angle beam transducers, and exploiting higher-order modes.
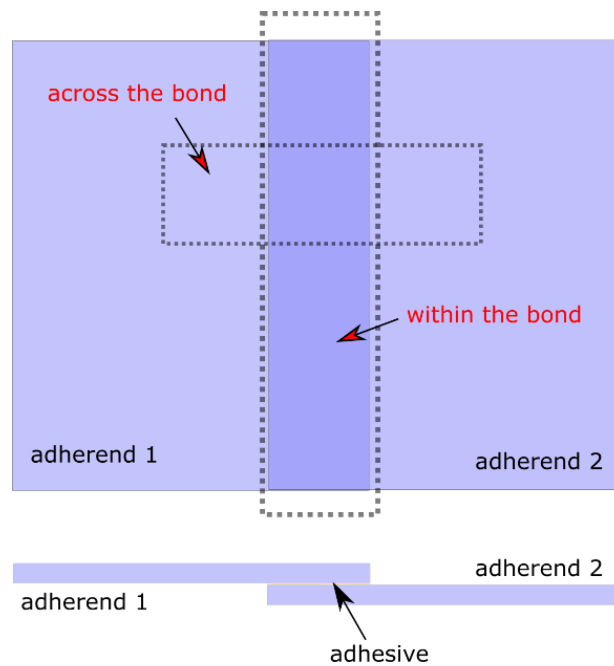
Figure 19 A sketch of a single lap joint

Theoretical work was conducted to simulate the Lamb wave propagation in an elastic–viscoelastic three-layer adhesive joint. The investigation of the wave structure curves showed that the interfacial continuity conditions for the Lamb wave propagation in the overlap section were satisfied. The phase velocity dispersion curves were determined using a global matrix method. Different modes in different frequency ranges with acceptable attenuation levels were identified as suitable for inspection [120]. Two sensor configurations can generally be used to investigate the bonds. Actuator–sensor pairs can be placed either across the bond or within the bond, on the overlap section (Figure 19). In literature [118], qualitative and quantitative analysis was performed on skin-stringer assembly. Transmission, reflection, and scattering behaviour were investigated regarding the particular modes and frequencies. Other papers dealing with experimental measurements also revealed the possibility of damage evaluation through the wave scattering patterns [119]. The degradation of the adhesive bond properties caused by aging was presented by the change in dispersion curves obtained using 2D-FFT [121, 122]. Transmission coefficients were calculated in the frequency domain to evaluate adhesive bond geometry, material properties, and the presence of a defect [123]. Transmission coefficients were determined in bonded aluminium plates to infer the mechanical properties of the bond. A wave propagation problem of composites joints was solved numerically, by SAFE and experimentally, focusing on transmission of S0 mode through the joint [124]. Specimens with initially good and poor adhesion were tested [125]. A wave structure analysis was proposed to select a sensitive mode and frequency for artificial defects in a composite skin-stringer assembly [126].

6 Objectives

The literature review concerning Lamb waves revealed that dispersion curve construction based on experimental data is often difficult to determine simply and fast.

Velocity dispersion curve is key information for further damage assessment. The time of flight (ToF) parameter may change due to the structural degradation or thickness change. Therefore, ToF is perfect for evaluating impact damage, delamination, or debonding. However, environmental and operational conditions influence guided wave propagation in terms of amplitude and ToF (velocity). Correct interpretation or compensation of the influenced signals is essential since it decreases false alarms of damage detection.

As a result, the general objectives of the thesis are formulated as follows:

1. Propose a fast method for dispersion curves construction based on experimental data
2. Improve input data pre-processing for existing impact damage detection algorithm
3. Improve diagnostic capabilities for delamination assessment exploiting velocity-thickness relation
4. Evaluate the performance of the method under the environmental and operational conditions

The thesis objectives are defined separately; however, they follow each other somehow. Velocity determination is closely tight to the mode identification, and velocity values may be used in damage extent calculations.

For reliable utilization of the UGW method within the structural tests, it is critical to understand the method itself, conduct as many tests as possible, learn the corresponding procedures with equipment, and get experiences with different structures and damage types. All experiments were performed in the Czech Aerospace Research Centre (VZLU), by which a sufficient number of test specimens representing aircraft structures was guaranteed.

7 Dispersion curves

Group velocity is the velocity at which the wave packets travel, and its knowledge supports the propagating mode identification. Knowing the whole segment of a group velocity curve for both modes help orientate which mode and when to expect at various actuator–sensor paths. However, based on a very easy distortion of wave packets in practice due to the frequency shifting, edge reflections, etc., group velocity has been determined within this thesis only indicatively. Therefore, a methodology for the phase velocity determination was proposed since the phase velocity may be easily recalculated into the group velocity.

The experimental part of the thesis is focused on the typical composite structures used for aerospace applications. However, the topic of velocity dispersion curves is dedicated to both isotropic and anisotropic structures. The complications with the Lamb wave propagation in anisotropic structures compared to the isotropic ones were briefly explained in chapter 4. In this chapter, frequency filtering is proposed to determine phase velocities using the experimental data. First, measurements performed on an aluminium alloy sheet representing the isotropic structure were exploited to demonstrate the proposed methodology. Then, phase and group velocity measurements supplemented by related calculations were conducted for both structures – isotropic and anisotropic. A thermoplastic composite plate was utilized to verify the methodology for anisotropic structures. Experimental data were compared to the theoretical calculations. Theoretical dispersion curves for isotropic plates were calculated according to the Rayleigh-Lamb equation. SW GUIGUW based on the SAFE method was exploited to determine theoretical dispersion curves for the composite structure.

7.1 Phase velocity determination proposal

The methodology of the phase velocity determination using experimental data is proposed. Depending on the actuation parameters, the particular actuation burst has a certain frequency bandwidth +/- Δf around the central frequency. For instance, as seen in Figure 20 b, bandwidth at the full width at half maximum (FWHM) for a 5-cycle sine burst in the Hanning window with the centre frequency of 60 kHz is 28 kHz (45-73 kHz). Therefore, the potential lies in many single-frequency components filtering using one broadband signal.

The whole process outlined in Figure 20 is comprised of the following steps:

1. Pre-processing – wave packets extraction + zero padding
2. Signals conversion from the time domain into the frequency domain

3. Band filtering (low pass and high pass)
4. Signals transformation back to the time domain
5. Time shift determination of the corresponding phases
6. Phase velocity calculation

The corresponding wave packets/the partial wave packets are truncated from the signals measured at two close positions. Afterward, the signal is zero-padded (Figure 20a) to extend in the time domain to increase the frequency resolution. Steps 2-5 are performed twice. First, a band filter is used with such frequency bandwidth, so the amplitude variations back in the time domain are still distinct (Figure 20c). The signals are shifted in time to match (cross-correlated). Then, a band filter is used again to get a narrow frequency spectrum (Figure 20d). Finally, the time shift is adjusted to match both signals again. The corresponding time shifts are used to calculate phase velocities.
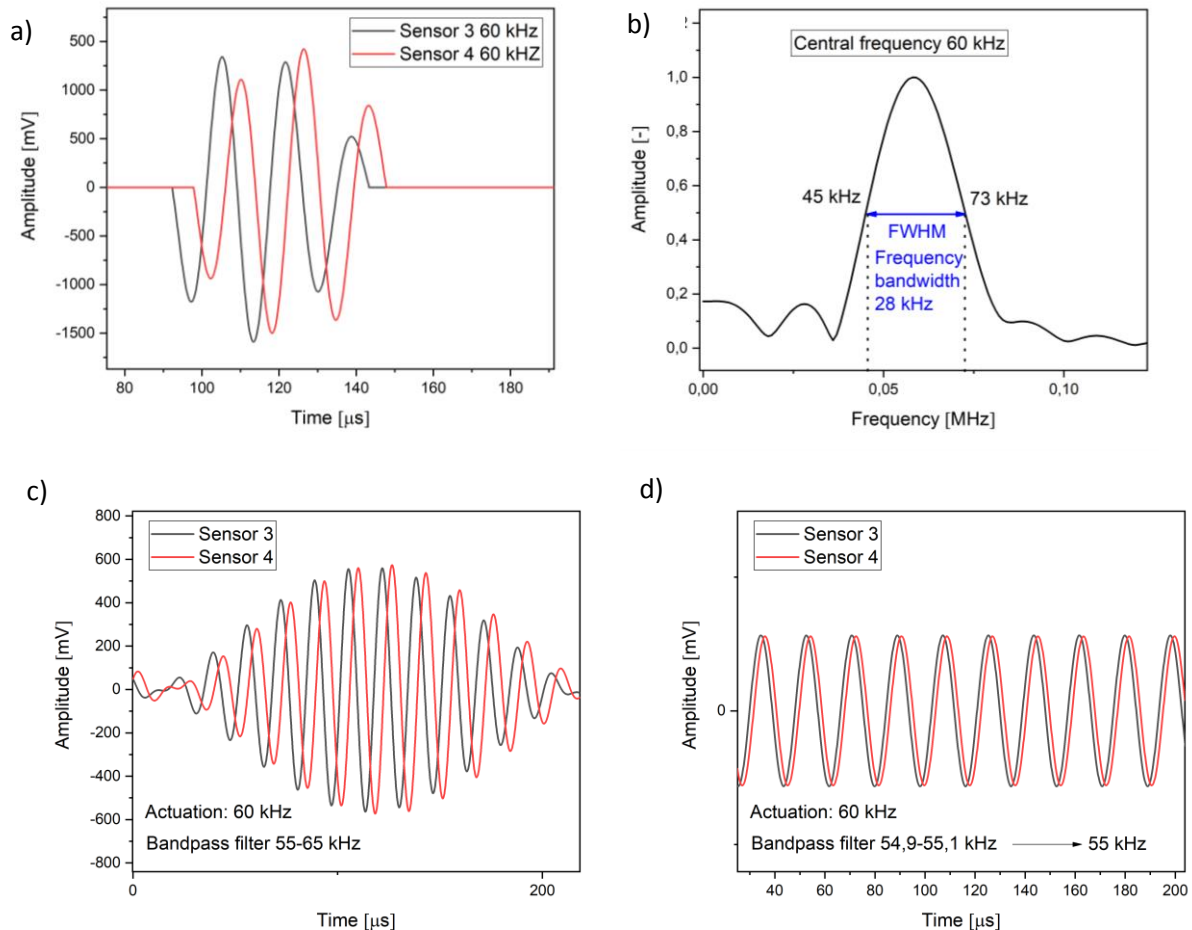
Figure 20 Example of the phase velocity determination methodology for 60 kHz signal a) signals at two close positions, b) frequency spectrum, c) wider filtered signals, d) narrow filtered signals

Narrow frequency bandwidth is very close to a single frequency signal which travels with the phase velocity. The resulting phase velocity is very close to the real phase velocity value. The frequency filters are determined for values resulting from the frequency resolution, so the centre of the bandwidth is the corresponding discrete frequency value. If the frequency step is 1 kHz, the precision is better than +/- 1 kHz.

The methodology is demonstrated on measurements performed on a 1.4 mm thick aluminium alloy sheet. A comparison of the phase velocity calculations using the Rayleigh-Lamb equation and values obtained by the proposed methodology is presented in Figure 21. Phase velocity values within the range of 35 kHz – 135 kHz were experimentally determined using only four broadband signals at 50 kHz, 60 kHz, 90 kHz, and 120 kHz.
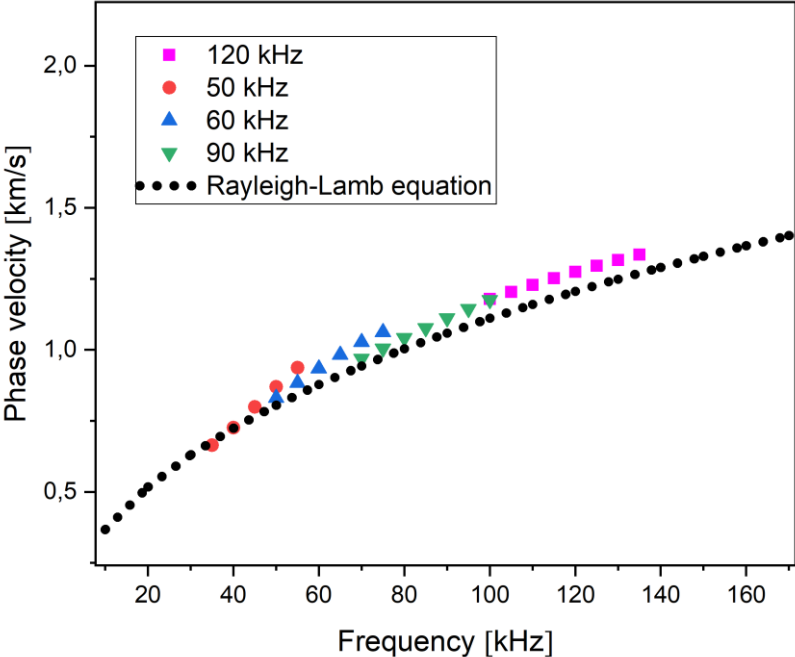
Figure 21 Comparison of the calculated phase velocity and values obtained using the experimental data

7.2   Dispersion curves for the isotropic plate

The isotropic structure is represented by a 1.4mm aluminium alloy sheet. Phase and group velocity dispersion curves were determined using:

1. Rayleigh-Lamb equation
2. Experimental measurements
   a. Group velocity tracking the envelope
   b. Phase velocity using the frequency filtering
3. Calculation of c_g using equation (60)

Aluminium alloy sheet 7475 T735 with a thickness of 1.4 mm and 400 × 500 mm dimensions was utilized for this experiment. Transducer A1 in the middle of the plate served as an actuator a two transducers S2 and S3 at a considerable distance from the edges served as sensors. 5-cycle sine burst was used as an actuation signal in the frequency range of 30-250 kHz with the step of 5 kHz. A schema is presented in Figure 22.
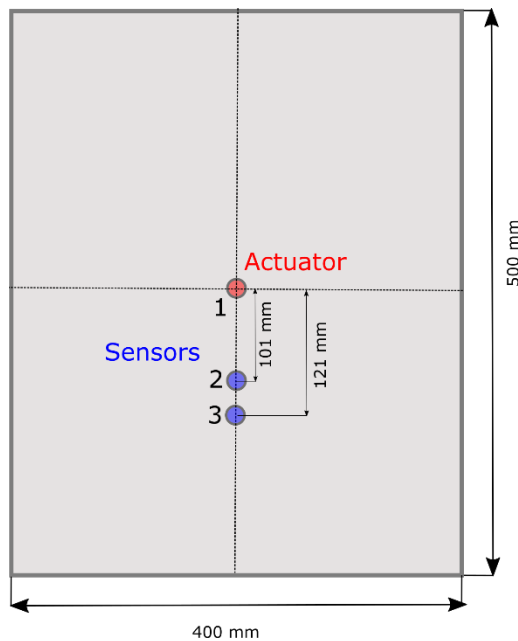
Figure 22 Schema of the aluminum alloy test specimen

The difference of ToF at the locations of S2 and S3 was used to determine the group velocity of the fundamental A0 mode. Figure 23 shows the obtained time difference *dt* using the maximum peak correlation and envelope correlation approach. Correlation of the envelope maximum amplitudes gives in the case of 120 kHz time difference of 10.164 μs while for the maximum peak correlation, the time difference is 7.88 μs. The resulting group velocity would be either 1968 ms^{-1} or 2538 ms^{-1}. Compared to Rayleigh – Lamb equation calculation, the methodology of envelope correlation is more precise. As explained before, the maximum energy of the wave packet is shifting within the envelope and is somewhere between the maximum amplitude peak and the adjacent left or right peak.
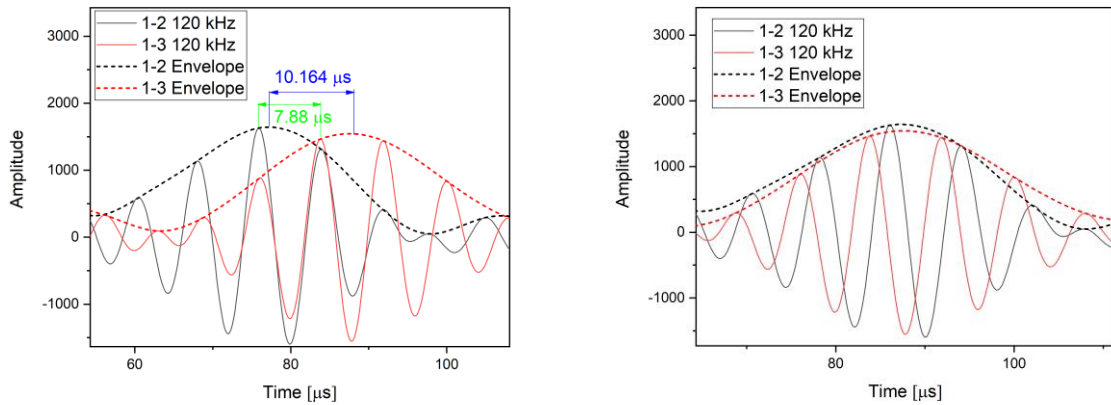
Figure 23 a) Difference in time delay of envelopes and maximum peaks, b) correlated envelopes

The segment of phase and group velocity dispersion curve of A0 mode is shown in Figure 24. "c_g experimental" are group velocity values obtained using the tracking of the maximum of envelopes. "c_P experimental" denotes phase velocity determined using the proposed frequency filtering methodology. Then, the time delay is easily identified, and velocity is calculated. This velocity is the closest value to the real phase velocity. Calculation of c_g based on the c_P using the equation (60) requires a much smaller frequency step. The resulting data were fitted with the step of 0.22 kHz to obtain better frequency resolution to calculate group velocities. Finally, the Rayleigh–Lamb equation was used to calculate the theoretical dispersion curve for the given frequency range. Longitudinal and shear velocities were set as 6.2 and 3.1 km/s, respectively. The experimentally obtained phase velocity curve shows a great match with the Rayleigh – Lamb equation.
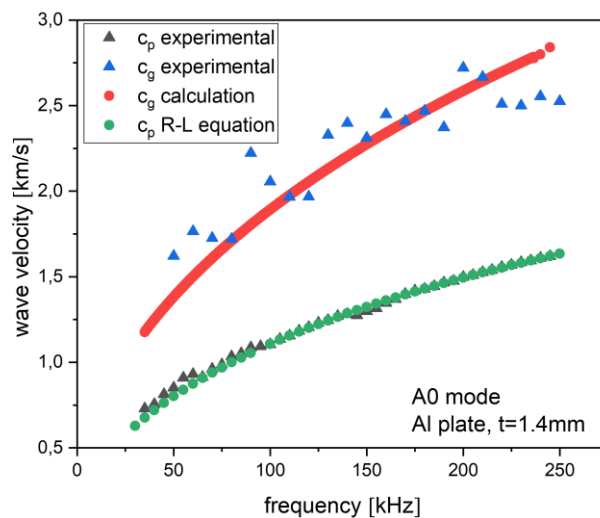
Figure 24 A segment of a phase and group velocity dispersion curve

7.3   Dispersion curves for the anisotropic plate

The anisotropic structure is represented by a flat plate made of a carbon fibre composite with a thermoplastic matrix. The following analyses were performed:

1. Phase velocity determination
    a. Experimentally using the frequency filtering
    b. Calculation employing GUIGUW SW
2. Direction dependent velocity calculation (GUIGUW)

Experimental measurements exploited the same methodology to determine phase velocity dispersion curves as for isotropic plates. The frequency filtering of signals measured at two close positions was utilized. SW GUIGUW based on the SAFE method, was exploited to compare dispersion curves with experimental data. In the case of multi-layered structures, stiffness matrix, density, the rotation of each layer, and the layer thickness serve as input data. The material is considered orthotropic, and the number of independent elastic constants is reduced to 9. The stiffness matrix is in the form of:

$$C = \begin{bmatrix} C_{11} & C_{12} & C_{13} & & & \\ & C_{22} & C_{23} & & & \\ & & C_{33} & & & \\ & & & C_{44} & & \\ & & & & C_{55} & \\ & & & & & C_{66} \end{bmatrix}$$

The following material data are essential for the coefficients C_{ij} calculations:

Young modulus E_{ij}, shear modulus G_{ij}, and Poisson's ratio ν_{ij}.

9 coefficients for the stiffness matrix C are calculated as follows:

$$C_{11} = \frac{1 - \nu_{23}\nu_{32}}{E_2 E_3 \Delta} \tag{65}$$

$$C_{22} = \frac{1 - \nu_{13}\nu_{31}}{E_1 E_3 \Delta} \tag{66}$$

$$C_{33} = \frac{1 - \nu_{12}\nu_{21}}{E_1 E_2 \Delta} \tag{67}$$

$$C_{12} = \frac{\nu_{21} + \nu_{23}\nu_{31}}{E_2 E_3 \Delta} \tag{68}$$

$$C_{13} \frac{\nu_{31} + \nu_{21}\nu_{32}}{E_2 E_3 \Delta} \tag{69}$$

$$C_{23} = \frac{\nu_{32} + \nu_{12}\nu_{31}}{E_1 E_3 \Delta} \tag{70}$$

$$C_{44} = G_{23} \tag{71}$$

$$C_{55} = G_{13} \tag{72}$$

$$C_{66} = G_{12} \tag{73}$$

$$\Delta = \frac{1 - \nu_{12}\nu_{21} - \nu_{23}\nu_{32} - \nu_{13}\nu_{31} - 2\nu_{21}\nu_{32}\nu_{13}}{E_1 E_2 E_3} \tag{74}$$

In general, $\nu_{ij} \neq \nu_{ji}$. The corresponding Poisson's ratio is calculated as follows:

$$E_1 \nu_{21} = E_2 \nu_{12} \tag{75}$$
$$E_1 \nu_{31} = E_3 \nu_{13} \tag{76}$$
$$E_3 \nu_{23} = E_2 \nu_{32} \tag{77}$$

A comprehensive analysis using the GUIGUW SW was performed on the carbon fibre composite material with a thermoplastic matrix (carbon/PPS laminate). Coefficients for the stiffness matrix were calculated based on the material parameters used for numerical simulations for the exact material in reference [132, 133]. Results were compared with experiments carried out on a simple plate. Also, phase velocity dispersion curves for the different number of layers were plotted to visualize the difference with increasing thickness. Direction-dependent phase velocities for A0 and S0 modes were calculated for a single layer, three-layered and seven-layered structure. Calculations were performed for three different numbers of layers, while the experiment was performed only for the 7-layered plate. Specifications are presented in Table 3. Figure 25 shows direction-dependent phase velocity for a 100 kHz S0 and A0 mode.

Table 3 Layer specifications

Number of layers	Stacking sequence	Thickness [mm]
1	(0/90)	0.315
3	(0/90), (+/-45), (0/90)	0.945
7	[(0/90), (+/-45)]$_3$ (0/90)	2.205
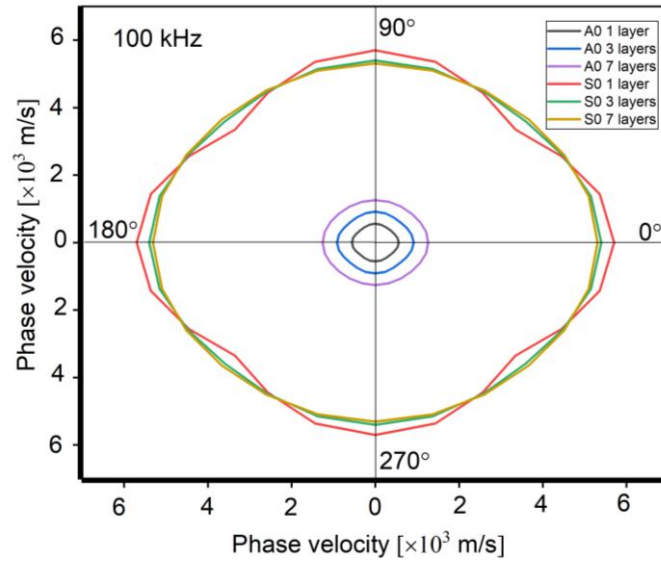
Figure 25 Direction dependent phase velocity of A0 and S0 modes for 1, 3, and 7-layered composite

The influence of an angle and a thickness was assessed using a 2-way analysis of variance (ANOVA). Both angle and thickness significantly influence the phase velocity for both modes. The difference between the lowest and highest velocity values for the A0 mode regarding the angle are 8.6 %, 7.4 %, and 3.4 % for the 1, 3, and 7-layered plates, respectively. The same analysis for the S0 mode shows direction-dependent velocity variations of 16.9%, 5.9 %, and 2.6 %. ANOVA proved the significant influence of both factors on the phase velocity. However, the 7-layered plate with velocity variations of 3.4 % for A0 and 2.6 % for S0 mode can be considered quasi-isotropic. A comparison of a segment of phase velocity dispersion curve calculated using GUIGUW SW and experimentally determined values using the proposed method described in subchapter 7.1 is seen in Figure 26.
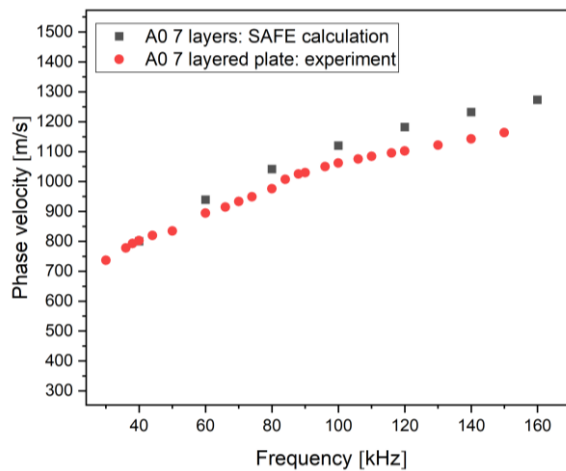
Figure 26 Comparison of experimental determination and SAFE calculation of a segment of a phase velocity dispersion curve for 7-layered composite plate

7.4 Conclusion

Presented results indicate that the proposed methodology of phase velocity determination using frequency filtering matches the calculations. Whether the input data are E, G, ϱ/ c_L, c_T for calculations using the Rayleigh – Lamb equation for isotropic plates or the stiffness matrix and ϱ for SAFE based GUIGUW SW for multi-layered anisotropic structures, the experimental methodology can be considered suitable. Deviations for anisotropic structures can be caused by material parameters variations. Material properties were taken from the literature. The methodology for the phase velocity determination is valid only for signals captured at two close positions with the same frequency spectra. The same condition is applied to the experimental data for the group velocity determination. Wave packet distortion shall be as little as possible, which can be ensured using two close sensors placed far from the edges and other geometrical discontinuities. Then, envelopes are correlated, and group velocity is determined. However, these conditions are more challenging to fulfil for the group velocity than phase velocity determination. Group velocity determination requires the whole wave packet and the corresponding envelope, whereas a few periods of the signal for the phase velocity determination are sufficient.

GUIGUW SW was used to demonstrate the direction-dependent velocity for both modes. The calculations indicate that the velocity variations are significant in the case of 1 layer: the more layered structure, the less variation in velocity. Variations are influenced by the mechanical properties in the given direction, so the layup plays and important role. In practical applications, the layup mostly shows the quasi-isotropic character.

8   Damage detection in composite structures

In the framework of this thesis, damage detection in composite structures include delamination detection in DCB specimens, a comprehensive impact damage detection in different structures, and debonding/delamination in adhesively bonded structures. Impact damage detection was performed on test specimens that correspond to the real aircraft structures and materials. Tests were performed on plates with constant and variable thickness, followed by impact damage detection in a complex structure as a skin-stringer joint. Delamination detection in DCB specimens was carried out, and Lamb wave propagation assumptions were exploited for the adhesively bonded structures. Delamination/debonding in the adhesively bonded joint was evaluated during the fatigue test.

The methodology of damage detection is based on the comparison of baseline measurements and measurements in the damaged state. In fact, any measurement can be compared. It depends on whether the desired output compares any two consecutive measurements (e.g., delamination growth) or absolute damage extent (absolute delamination length).

Time of flight (ToF) was the parameter chosen to characterize the damaged state due to the effect of the thickness change and/or mechanical properties degradation. Macroscopic delamination and debonding extent correspond to the ToF changes due to the thickness change. The corresponding mathematical relations were established. Impact damage detection exploits imaging algorithms, precisely the RAPID algorithm. ToF changes caused by impact damage were evaluated at the maximum wave packets peaks.

Attention was also paid to the identification of the propagating modes and suitable frequency tuning. Propagating modes were mostly identified using sensors mounted on the exact opposite spots of the tested structure. For the A0 mode, the signals are detected as out of phase and for the S0 mode as in phase. The knowledge of dispersion curves is also helpful.

The corresponding measurements were performed under the exact environmental conditions since Lamb wave velocity is temperature dependent. However, temperature dependency was investigated in Chapter 9.

In this work PWAS StemInc transducers or SmartLayer single sensors were used to actuate and detect Lamb waves. Two data acquisition measuring devices were utilized. One of them was the Scan Genie II developed by Acellent company with SW Access for damage detection. ScanGenie II is easy to control; however, the system, in general, has two disadvantages for the proposed measurements:

- The system is a black box.
- The system is unfit for nonlinear measurements.

The second system is ZEDO developed by the DAKEL company. This system was initially developed for Acoustic emission measurements and later adapted for the Lamb wave measurements (for VZLU purposes). The main reasons were to overcome disadvantages provided by Acellent system, primarily to enable nonlinear measurements, eliminate crosstalk and get a transparent data acquisition unit. However, SW control and suitable data processing tools are still under development by the time of finalizing the thesis, especially from the point of view of data automatization.

8.1 Delamination measurements in DCB specimens

A part of this chapter was published as Delamination growth analysis in mode I by means of Lamb waves in *Materials Today: Proceedings* within the DAS 2018 conference [b].

Several papers have been published investigating delamination propagation in double cantilever beam (DCB) specimens using Lamb waves, both experimentally and numerically. The proposed evaluations incorporated different signal features, such as correlation coefficients, magnitude changes, and velocity/time-of-flight (ToF) changes in a lengthwise actuator-sensor configuration [127, 128]. Another research deals with the numerical assessment of the ToF of direct and turning Lamb modes during crack propagation [129]. Interaction of A0 and S0 Lamb wave modes with delamination was investigated numerically and experimentally in [130]. Delamination was evaluated quantitatively. ToF changes were utilized to assess delamination size and location.

In this chapter, the delamination growth of DCB specimens using Lamb waves is investigated from the point of frequency tuning, actuation waveform, sensor placement, and selection of a parameter sensitive to delamination growth. The velocity dispersion of the fundamental asymmetric mode is exploited in order to determine the delamination onset during the test. Two types of preliminary Lamb wave measurements were performed - measurements on undamaged and already delaminated DCB specimens. Then, measurements during the DCB tests were performed. Precise delamination lengths were determined using the change in the ToF of A0 mode. A0 mode is delayed as the original beam shortens and the delaminated part lengthens. A relationship of the ToF change and delamination length using propagation velocities in a full-thickness and a half-thickness specimen was established. Another approach using reflected Lamb wave mode was outlined. Finally, the Lamb-wave-based delamination lengths were compared to the visually measured values. An error of up to 10% between the Lamb-wave-based delamination length and visually identified length was achieved.

8.1.1 Undamaged DCB specimen

Specimens were made of carbon-fibre plain-weave fabric reinforced with epoxy resin with a sequence of lamination of [(+/-45), (0/90)]4s. A polymer foil with a length of ~25 mm was inserted into the midplane of the 16-ply laminated panels as initial artificial delamination (Figure 27). Specimens with dimensions of 250×25 mm and thickness of 3.2 mm were cut from the panels.
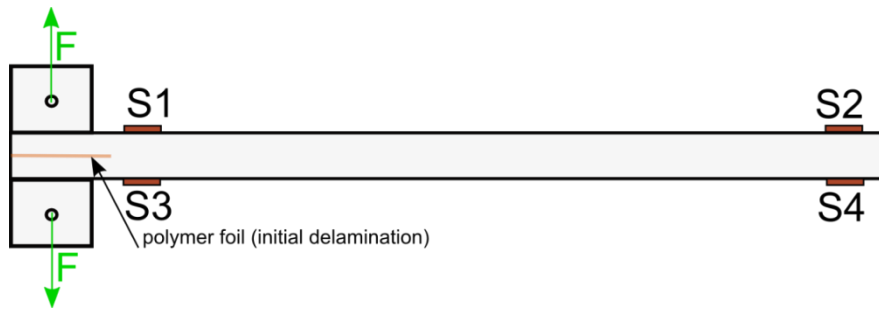
Figure 27 Sensor placement on DCB specimen

A pitch-catch configuration with transducers S1 and S3 as the actuators and S2 and S4 as sensors was utilized. Pairs of sensors—S1 and S3, S2 and S4—were glued symmetrically on both sides of the specimen. This arrangement enables the determination of the propagating mode. The example with four different actuation frequencies is shown in Figure 28. Regarding the specimen dimensions, edge reflections are included in the wave packets. Out-of-phase wave packets indicate A0 mode and in-phase signals S0 mode.
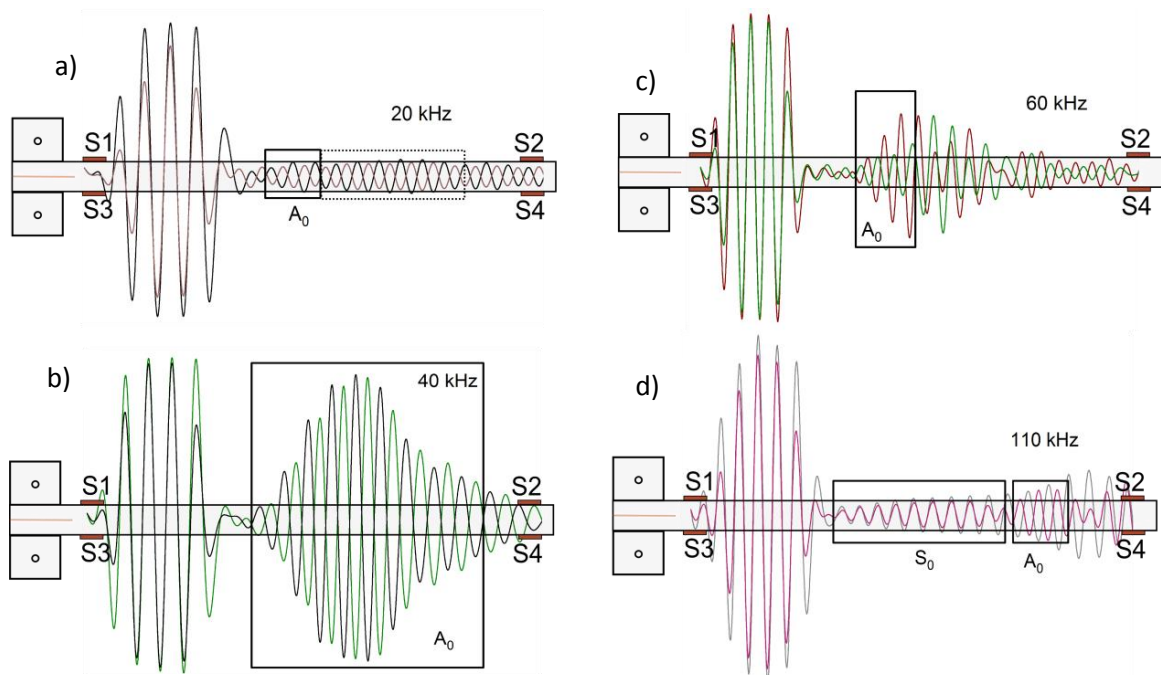
Figure 28 Lamb wave actuated by sensor S1 and detected by sensors S2 and S4 for a) 20 kHz, b) 40 kHz, c) 60 kHz, and d) 110 kHz

Parameters suitable for signal actuation were selected experimentally before the test. The objective was to actuate the fundamental A0 mode of high amplitude and clear shape. The comparison between Burst 3 (a sine wave of 3 cycles) and Burst 5 (a sine wave of 5 cycles) is shown in Figure 29a. Burst 5 generates more energy into the specimen and, unlike Burst 3, provides a clear shape of the A0 mode. The selection of the actuation waveform and the

frequency tuning was performed experimentally. Pulses in the range of 20–110 kHz with a frequency step of 5 kHz were actuated, as seen in Figure 29b. A high amplitude, clearly shaped A0 mode was generated with a frequency of approximately 40-45 kHz. In the first part of the signal, crosstalk that may be a limitation appears (marked in Figure 29a). The length of the crosstalk depends on the actuation frequency and actuation pulse. The longer the pulse and the smaller the frequency, the longer the crosstalk. If sensors are mounted too close to each other, the A0 mode is hidden in the crosstalk.
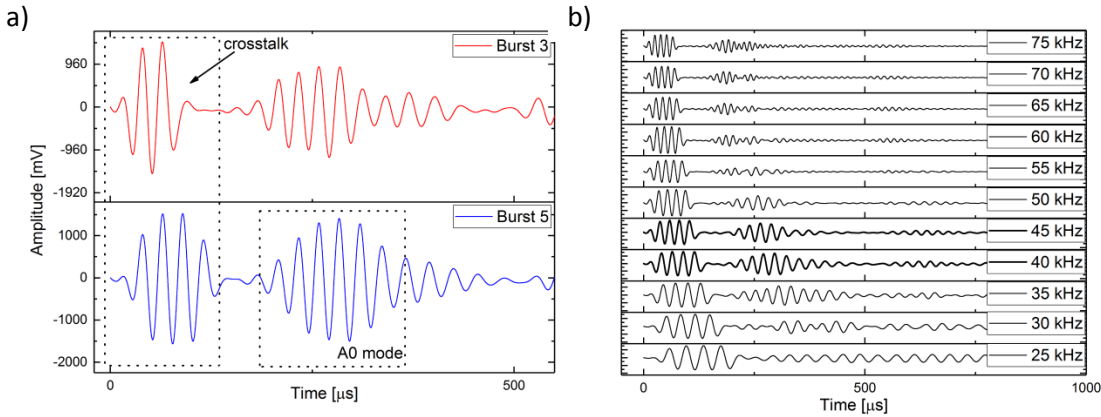
Figure 29 Comparison of actuation parameters: a) actuation waveform, b) actuation frequency

8.1.2 Delaminated DCB specimen

Measurement of the DCB specimen was also performed on the already delaminated specimen. 12 PZT transducers (serving as both actuators and sensors) were attached on both surfaces to verify the propagating mode and velocity variations for the two thicknesses. The longitudinal cross-section of DCB specimen with the indicated wave propagation is shown in Figure 30. Out-of-phase signals indicate an asymmetrical mode. The wave splitting of the fundamental A0 mode at the delamination tip was proved as well. A0 mode propagates through the original thickness and, at the delamination tip, splits into two slower A0 modes, as demonstrated in Figure 31.
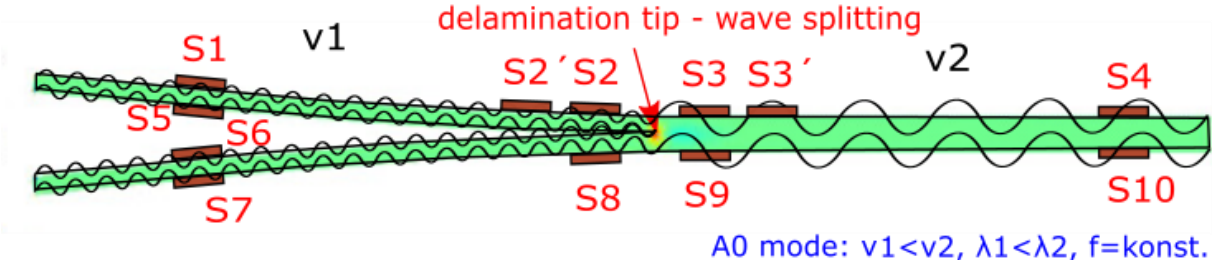
Figure 30 A0 mode propagation through a DCB specimen

60

The objective of these measurements was to prove the wave splitting and define velocity variations for the two thicknesses of the delaminated test specimen. Waves were transmitted by the actuator A4 and detected by sensors S1 + S5 and S6 + S7, indicating one wave splitting into two asymmetrical waves propagating along two delaminated sections. The out-of-phase signals detected at both delaminated beams are shown in Figure 31.
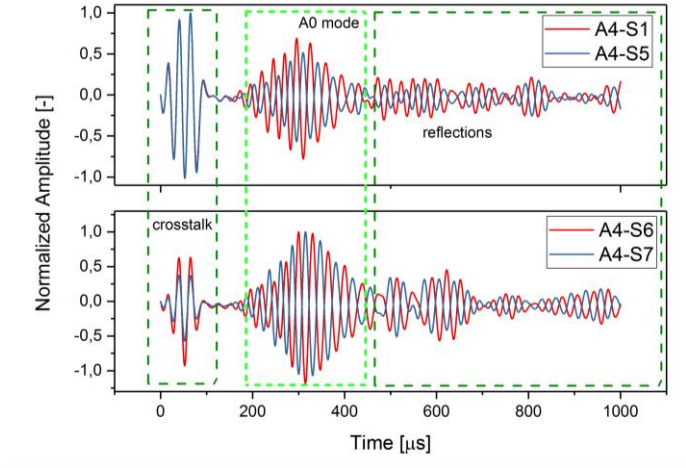
Figure 31 Signals of the A0 mode detected at both ends of the delaminated beams

A segment of a phase velocity dispersion curve for A0 mode was determined according to the methodology of frequency filtering. Actuator A1 and sensors S2, S2′ for delaminated part and S3, S3′ for the full thickness part were utilized. Phase velocity dispersion curves for both thicknesses were calculated using the GUIGUW SW. The comparison of experimentally determined and calculated values is shown in Figure 32.
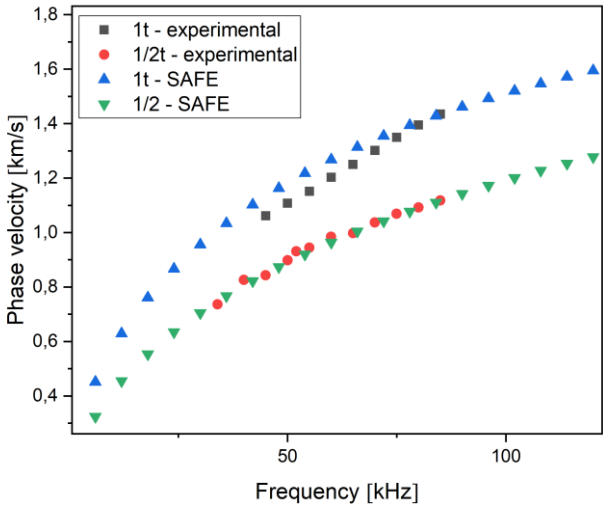
Figure 32 Segments of phase velocity curves for the half-thickness (1/2t) and full thickness (1t) of DCB specimen

61

8.1.3   Parameter sensitive to delamination growth

The phase and group velocity of Lamb waves are dependent on the product of the frequency and thickness. With delamination growth, two delaminated parts of the specimen, each with half thickness, extend, and the original beam shortens. As the delamination grows, the A0 mode propagates slower along the delaminated part. Lengthwise sensors were utilized for evaluation according to Figure 27. S1 as the actuator and S2 as the sensor results in time delays of signal arrivals compared to the baseline measurement. An equation solving the delamination length was analytically derived as follows:

$$a_n = \frac{v_1 v_2 \Delta t_n}{v_2 - v_1} \tag{78}$$

where a_n represents the delamination length, v_1 and v_2 represent the velocity of a Lamb wave of a specific frequency in the specimen with half thickness and full thickness, respectively. The variable Δt_n denotes the time difference of the n_{th} measurement compared to the baseline state. The knowledge of velocities for both thicknesses is conditional, and the accuracy of velocity determination is directly linked to the accuracy of delamination length determination. The equation is valid for both group and phase velocities. If it is possible to track the envelope, the group velocity is exploited for calculations. The corresponding phase velocity is used if the specific peak or zero-crossing point is tracked. Differences in time of arrival differences based on tracking the particular point (zero crossings, maximum and minimum peak points) of the wave packet are seen in Figure 33. Time of arrival differences increase for A0 due to dispersion nature. Each time of arrival difference corresponds to a different phase velocity and hence the frequency. A corresponding velocity for the points being tracked shall be considered to reduce the deviation in the delamination length calculation.
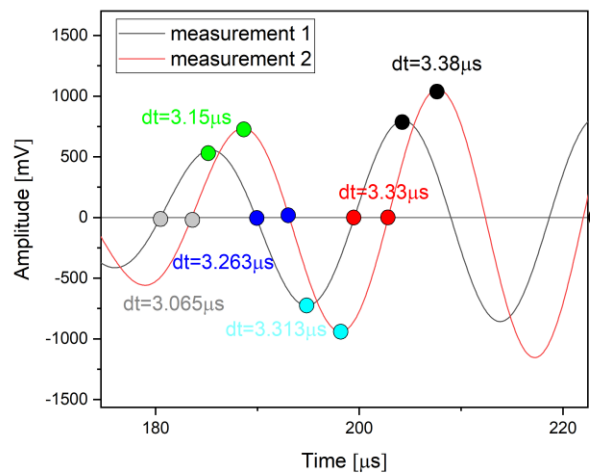
Figure 33 Example of dt variation

Except of the lengthwise sensor configuration, one more sensor configuration is sensitive to delamination growth. Sensor S1 as an actuator and S3 as a sensor (according to the placement of the sensors in Figure 27) were also exploited for evaluation. A turning Lamb-wave mode likely appears at the delamination tip, and the determined time delays correspond to the delamination growth.

8.1.4 DCB test

DCB tests were performed according to the ASTM D5528 standard [131]. Based on the preliminary measurements, A0 mode with a frequency of 45 kHz was chosen. An approach of direct calculation of delamination lengths using an actuator and sensor placed lengthwise on the opposite sides of the specimen was introduced. Time delays corresponding to the delamination lengths were tracked at the maximum peak points. Using this approach, the same phase of the wave packet was tracked, and the corresponding phase velocities were used in the equation. The phase velocities included in the equation were $v_1 = 858$ m/s for the half-thickness and $v_2 = 1160$ m/s for the full-thickness part.

A comparison between the visually identified delamination lengths and Lamb-wave-based calculated lengths according to the equation (78) is shown in Figure 34 for two specimens. An average mean percentage error of 8.4 % and 4.9 % were achieved.
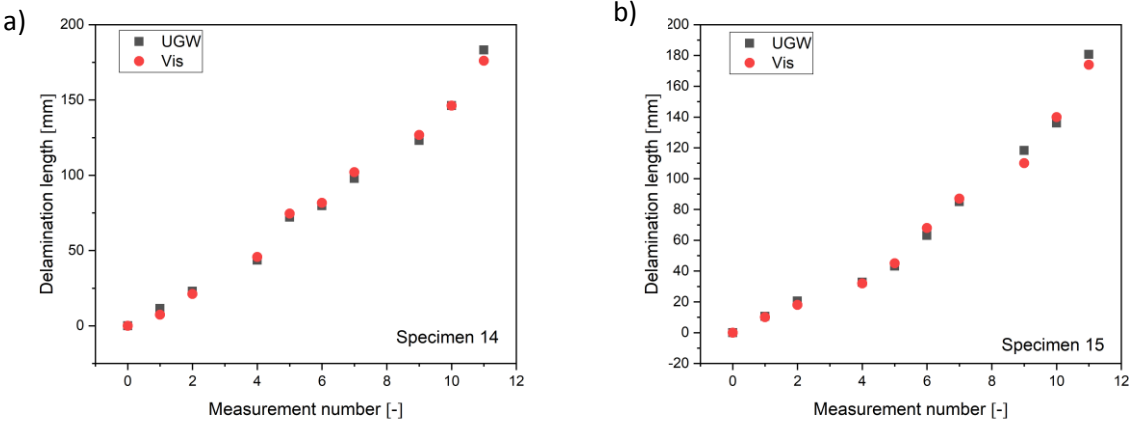
Figure 34 Results: a) the trend of time delays of the A0 mode during the delamination growth, b) the comparison of Lamb wave-based calculated delamination lengths and visually determined values

An example of signal delays of the turning mode utilizing sensors S1 and S3 is shown in Figure 35. The specific first arrival time value corresponds to twice the delamination length. The wave

packet travels forward, and at the delamination tip propagates back again. The first visible delay corresponds to a delamination length of 68 mm. During the final measurement, the specimen is split into two separate beams for the delamination of 200 mm; therefore, no signal is measured by the sensor mounted on the second beam. At a frequency of 40 kHz, the delayed A0 mode is hidden in the crosstalk for the measurements of smaller delamination. This issue can be overcome by using higher frequencies. However, using the Acellent system, the crosstalk limitation remains.
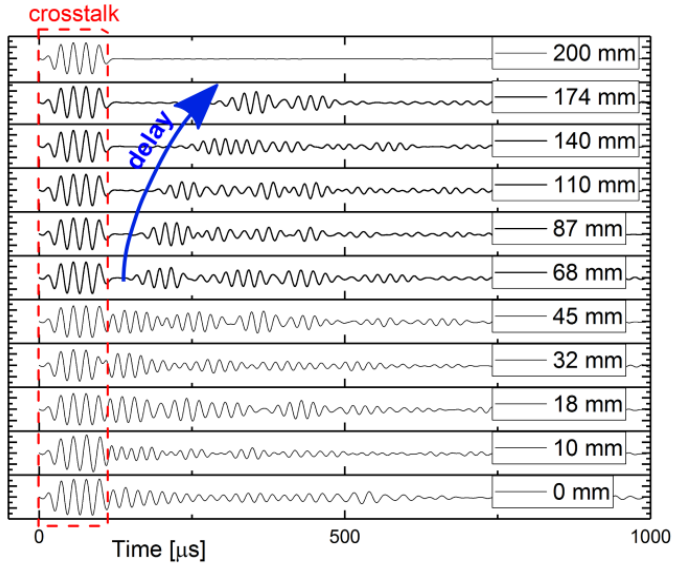
Figure 35 Signals actuated by sensor S1 and detected by sensor S3 during the test

8.1.5 Conclusion

A comprehensive Lamb-wave propagation analysis was performed on DCB specimens in two static configurations and during the DCB test. Basic parameters, such as actuation frequency and waveform, were taken into account, as well as the configuration of the actuators and sensors. The following conclusions regarding DCB specimens of a given thickness can be stated:

- Burst 5 actuation waveform was used instead of Burst 3 to actuate the clearly shaped and high-amplitude mode
- A burst of a frequency of approximately 40-50 kHz actuated the clearly shaped and high-amplitude A0 mode.
- Two actuator/sensor arrangements were investigated:
  - Lengthwise, 200-mm-distant sensors enabled measurements of ToF of A0 mode

- o Symmetrically placed sensors on both sides of the specimen enabled measurement of the A0 turning mode. The first detected delamination length was at 68 mm due to the crosstalk.
- Time delays from measurements using lengthwise-placed sensors can be directly used for delamination length calculation using equation (78).
- The knowledge of the precise values of the A0 mode phase velocities for the original thickness and half-thickness beam is conditional. Deviations may lead to misleading results.

In conclusion, using the proper actuation parameters evaluation of delamination lengths proved not to be complicated. Moreover, Lamb-wave monitoring of delamination growth showed excellent agreement with the visual data. DCB test is a standard test to determine the fracture toughness G_{IC} and delamination lengths determination is conditional. Lamb wave measurements can be used instead of visual measurements based on these experiments.

8.2 Impact damage detection in plates

Impact damage detection assessment was included in the publication Defect Detectability in Composite Plates with Variable Thickness Using Lamb Waves presented during the 58th conference on experimental stress analysis (EAN2020). The conference presentation was awarded as the best presentation within the section of NDT [c].

Several tests have been performed to detect impact damages. RAPID algorithm programmed in Phyton was utilized for impact damage imaging. Composite plates with constant and variable thickness served as the basic structures to verify the methodology of data pre-processing and test the algorithm. These measurements were followed by impact damage detection in a more complex and typical aircraft structure: a skin-stringer joint.

The research of impact damage detection was comprised of the following steps:

1. Determination of the damage-sensitive mode (A0/S0)
2. Determination of the suitable frequency
3. Methodology of extraction of the suitable DI

Lamb wave parameters and signal processing tools were defined to enhance the automatization process of impact damage detection.

8.2.1 Materials and methods

Test specimens were manufactured from carbon composite with thermoplastic matrix ABS5045. The first plate (P1) had dimensions of 280×530 mm and thickness of 2.2 mm, and the second plate (P2) had dimensions of 240×615 mm and thickness of 3.5-4.3 mm. The second plate with variable thickness was stacked from 4 or 5 glass layers and 10 or 15 carbon layers according to the part thickness. Three impacts were subjected to plate P1 and two to plate P2. PZT discs were placed along the edges and served as both actuators and sensors. Measurements were performed before and after each impact. Standard 5-cycle sine wave modulated by Hanning window was used as the actuation signal. The frequency of 80 kHz was chosen for the A0 mode based on the clear mode shape (no distortion of the wave packet), and the frequency of the 180 kHz was chosen for the S0 mode.

Impact damage evaluation was performed using three methods based on the signal comparison of all the actuation–sensor pairs before and after the induced damage.

1. The first one exploited SW Acess provided with the Acellent Scan Genie II measuring device. The correct determination of the impact location was inconsistent. It was not possible to choose one frequency and methodology to correctly locate all the impacts.
2. Therefore, the RAPID algorithm was programmed to obtain variability in signal processing. The correlation coefficient and ToF delay were exploited as a signal parameter to calculate the damage index (DI) as follows:
    a. $DI_i = 1 - \varrho_i$
    b. $DI_i = 1 - T_i$,

where T_i is the normalized value of the corresponding $\varDelta t_i$ taken from the set of all paths and ρ_i is the correlation coefficient.

Evaluation of the chosen signal parameters was performed according to the following steps:
1. Group velocity determination of the A0/S0 mode
2. Identification of the corresponding wave packets for all actuator–sensor paths to be used for evaluation
3. Extraction of the particular wave modes
4. Determination of:
    a. The correlation coefficient of the relevant wave packets
    b. ToF delay of the maximum amplitude peak of the relevant wave packets

The comparison of the three methods utilizing A0 mode at 80 kHz is shown in Figure 37 and Figure 38 for the constant thickness plate P1 and variable thickness plate P2, respectively. Designations a), b), c) denote evaluation using SW Acess, RAPID - Correlation coefficient, and RAPID - ToF delay, respectively. The ToF delay parameter was the only one that showed the correct localization of all impacts. The real impact locations are marked with the red cross. ToF delays at the direct actuator – sensor path through impacts for the variable thickness plate were about 4-10 times smaller than for the constant thickness plate. The difference is shown in Figure 36. However, normalized values are used in the RAPID algorithm, so all impacts are clearly visualized.
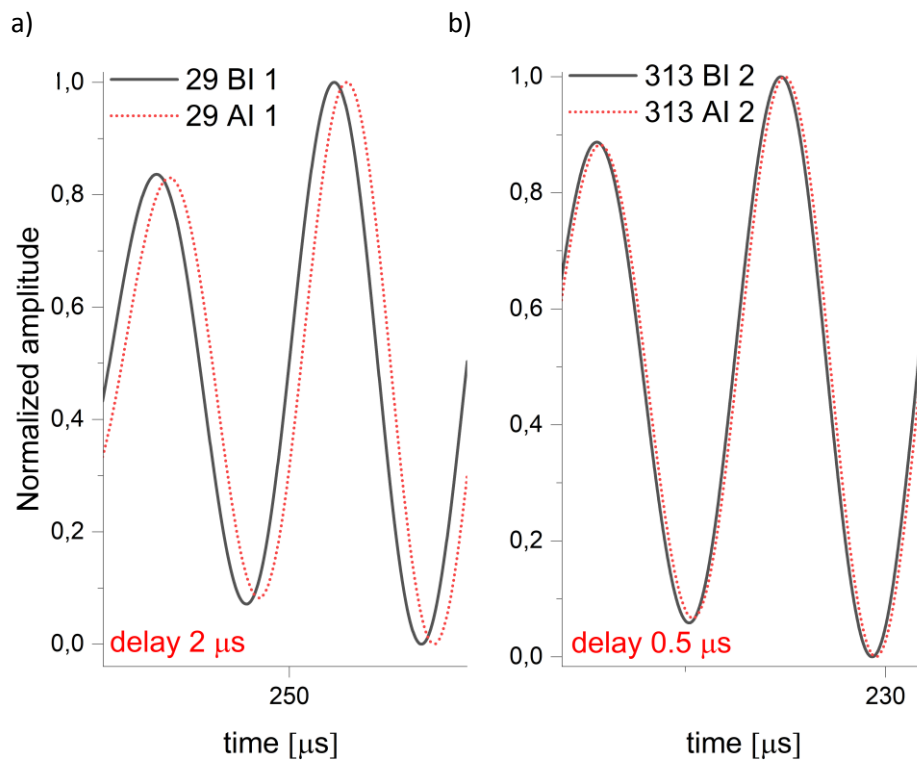
Figure 36 Comparison of the A0 wave delay for a) constant thickness plate and b) variable thickness plate
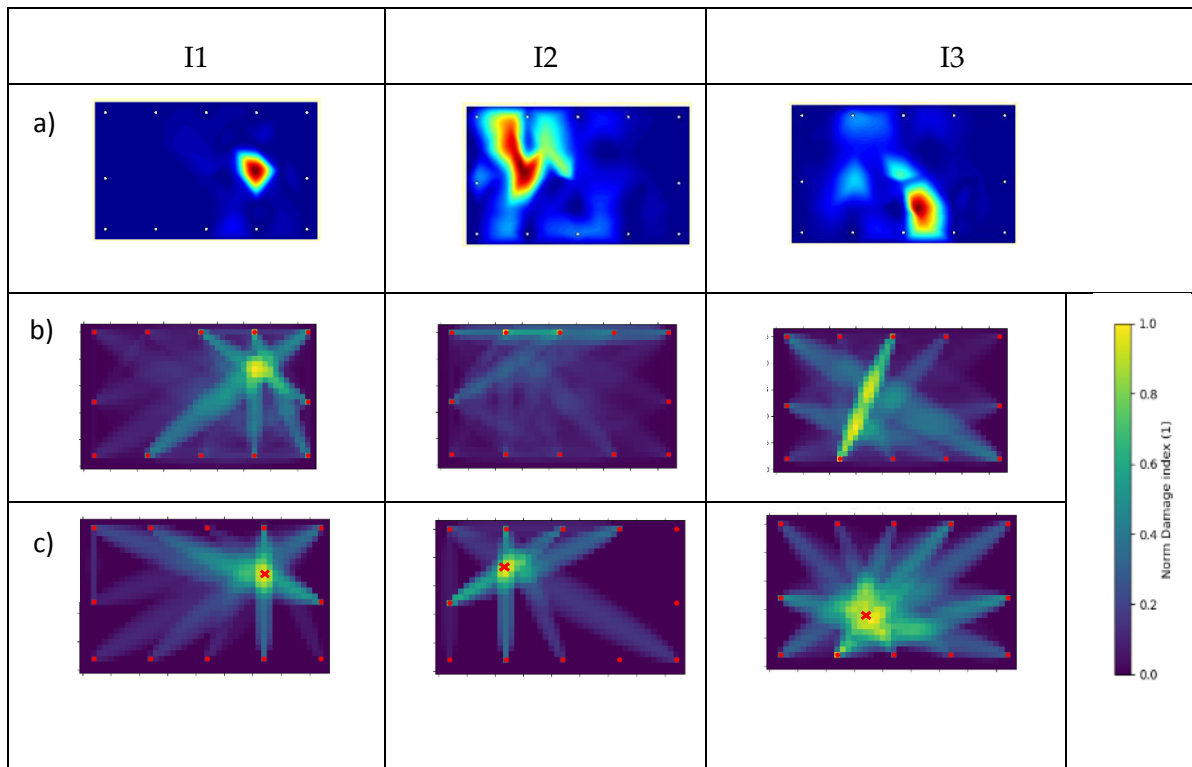
Figure 37 Comparison of impact evaluation for the constant thickness plate using a) SW Acess, b) RAPID - correlation coefficient, c) RAPID - ToF delay
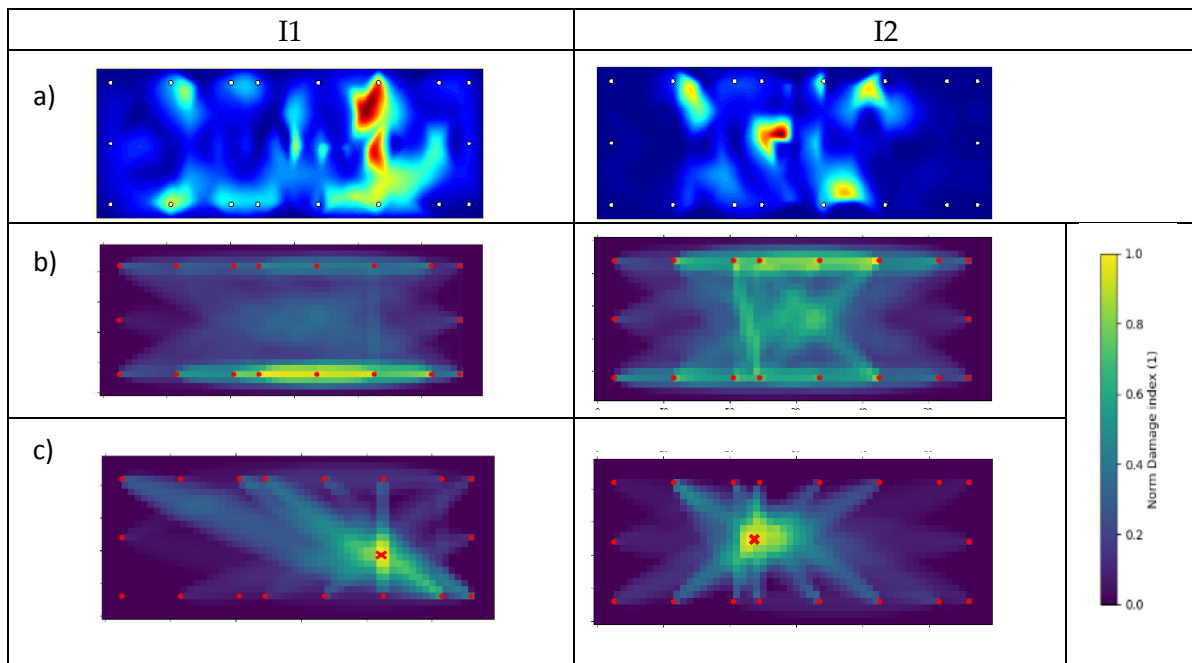
Figure 38 Comparison of impact evaluation for the variable thickness plate using a) SW Acess, b) RAPID - correlation coefficient, c) RAPID - ToF delay

The comparison of impact damage detection using A0 at 80 kHz and S0 mode at 180 kHz was performed. Both modes were possible to exploit; however, time delays were about ten times smaller for the S0 mode than the A0 mode.
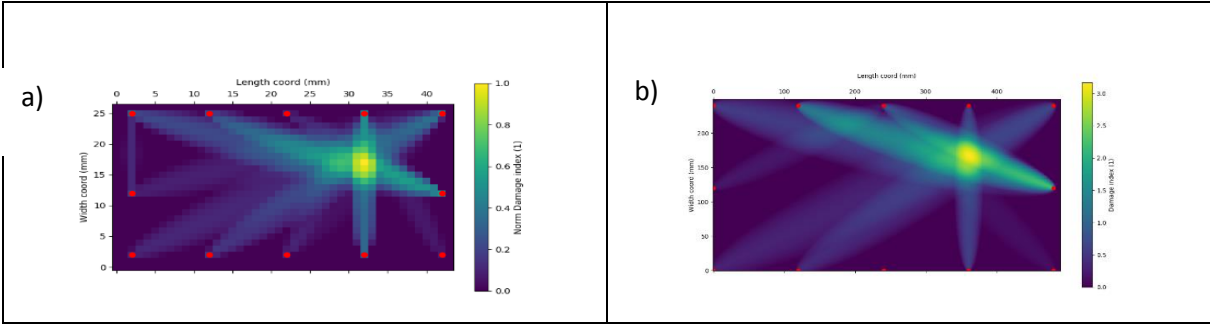
Figure 39 Impact I1 on the plate P1 visualized exploiting a) A0 mode at 80 kHz and b) S0 mode at 180 kHz.

8.2.3   Conclusion

Two thermoplastic composite plates were subjected to multiple impact damages. Three methods were used for damage evaluation. SW Acess with unknown algorithm and RAPID algorithm with two different DI based on the correlation coefficient and ToF delay were used to evaluate impacts. Results using SW Acess did not correctly locate all impact damages at the given frequency, so this method was not effective. The correlation coefficient used in RAPID algorithm did not show correct results either. ToF delay extraction of the relevant peaks of A0 mode detected the location of all five impacts correctly. However, ToF delays measured on the variable thickness plate had significantly smaller values than on the constant thickness plate. Nevertheless, normalized values in the RAPID algorithm enabled clear visualization. Significantly smaller ToF delays were probably caused by the material itself. The variable thickness plate contains multiple glass layers, which probably influence the guided wave propagation. S0 mode was also exploited. Impact damage was correctly localized even if ToF delays for the frequency of 180 kHz were about ten times smaller than for A0 mode. S0 mode is in this frequency range much faster than A0 mode. Therefore, the S0 mode was the first to be detected and could not be mistaken. On the other hand, time delay sensitivity to impact damage is lower. DI can be normalized, so the visualization is correct. However, the A0 mode was proposed to be utilized if possible. Also, it can be concluded that extraction of the particular wave is essential, especially for the variable thickness plate. Using the same time window length for different actuator-sensor distances includes multiple wave reflections, which can cause false damage indications.

8.3 Impact damage detection in complex structures

Detailed analysis of Lamb wave propagation in the typical aircraft composite structure - a skin-stringer joint representing a part of the aircraft door was performed. Findings were exploited for the proper frequency selection to detect impact damages. The impact damage detection procedure used for the plates was assumed to be exploited. Previous results indicated that A0 mode is more sensitive to impact damage than S0 mode, so the time delay of the A0 mode was planned to be used as DI. Nevertheless, the complexity of the test specimen made the use of A0 difficult. Wave propagation effects at the structural changes enabled A0 mode extraction at all actuator-sensor paths. Therefore, the ToF delay of S0 mode was used as DI.

The following tasks were realized:

1. Measurements before and after the skin and stringer were bolted together.
   - The aim was to analyse the propagation at different frequencies in terms of the propagation of individual modes through the joint.
2. Sensor network optimization and suitable frequency selection.
   - The aim was to choose mode and frequency in such a way that the wave packet would propagate dominantly either into the bottom skin or into the stringer.
3. Impact damages realization in the stringer section.
4. Evaluation of damage detection ability using RAPID.

8.3.1 Experimental setup

Two test specimens designated as Omega 1 and Omega 2 were manufactured. The identical material as for the plates – carbon composite with thermoplastic matrix was used. The skin-stringer joints were realized only by high locks, without any adhesive. 16 PZT disc sensors were mounted on the test specimens within four sections, according to Figure 40. The sections were determined according to the potential location of the impact damage. Sensors within sections 1, 3, 2′ covered the skin, and section 2 covered the stringer.
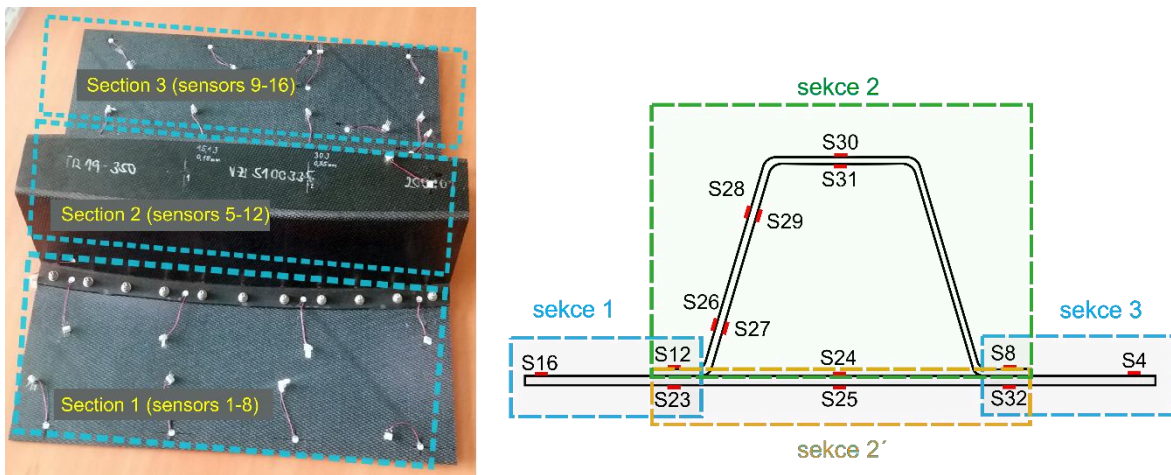
Figure 40 Subsections within the Omega test specimen

Preliminary measurements included evaluation of amplitude dependency on the frequency for both modes. The 3-sine wave was actuated in the frequency range of 50 – 250 kHz. A0 mode amplitude increases up to 90 kHz and then decreases again. S0 mode amplitude increases up to 250 kHz.
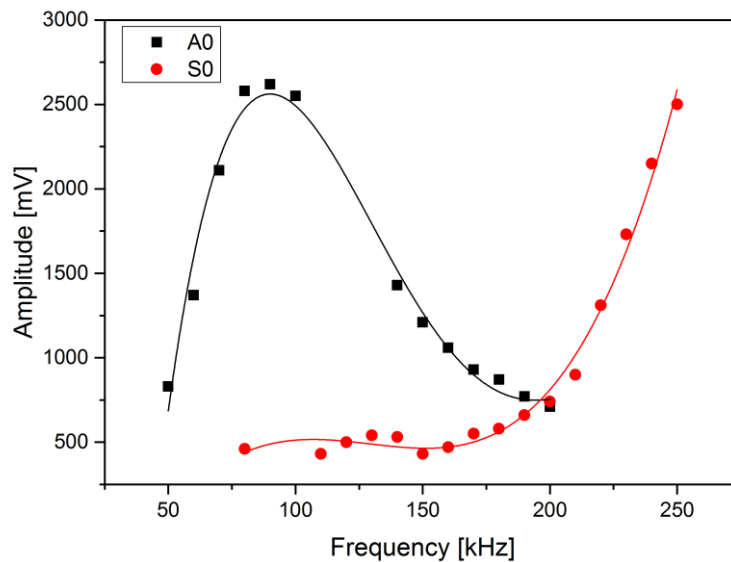
Figure 41 A segment of the frequency – amplitude dependency for A0 and S0 mode

Segments of phase velocity dispersion curves were determined experimentally and compared to the calculations using the GUIGUW SW. The identical material parameters as for plates in section 6.3. were exploited.
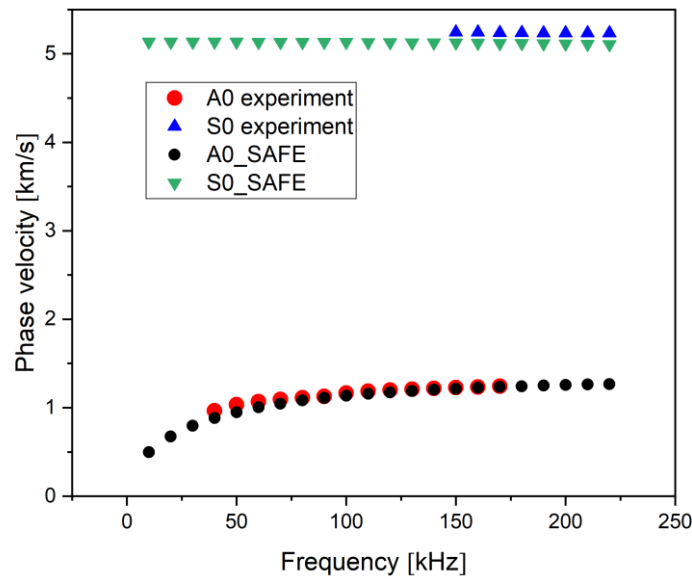
Figure 42 A segment of a phase velocity dispersion curve – experimental and calculated values

8.3.2 Qualitative evaluation of Lamb wave propagation

Skin-stringer joint represents a complicated structure from the perspective of mode identification. Unlike the propagation in a simple plate, the joint may cause mode conversion. Together with multiple reflections, mode identification is difficult without numerical simulations or experimental methods of full wavefield imaging. Due to the lack of these techniques, supporting measurements were also performed before and after the skin and stringer were bolted together to assess the propagating modes qualitatively. Two frequencies, 80 kHz and 180 kHz were used to evaluate the propagation qualitatively. The signal actuated in the area of the joint and detected on the other side of the joint is presented in Figure 43. There is almost no change in the propagation of S0 mode at neither the frequency. Other detected wave packets are probably comprised of various reflections and A0 mode. Especially at the frequency of 180 kHz, secondary wave packets are affected by the structure change. The probable cause is the wavelength sensitivity. A smaller wavelength is more sensitive to structural changes. At 180 kHz, the A0 wavelength is several times smaller than S0.
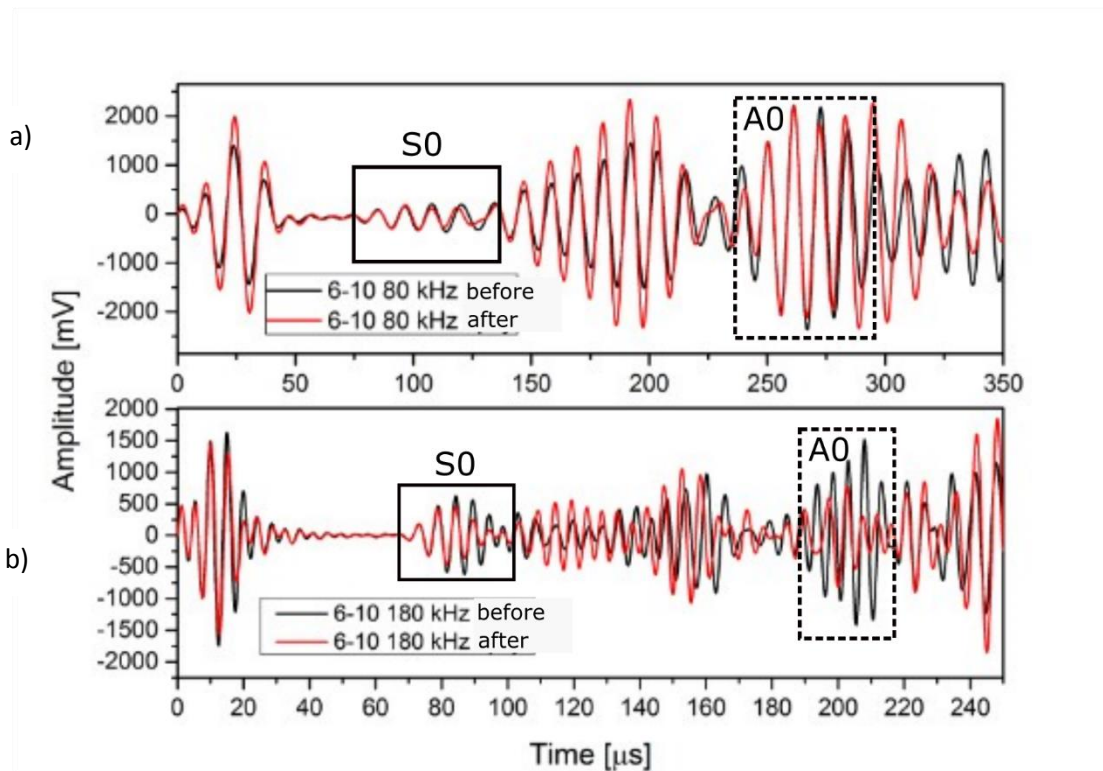
Figure 43 Signals detected on the stringer before and after the section were bolted together

Additional sensors were mounted on the test specimens, according to Figure 44. Sensors were placed along the cross-section line on both surfaces. The aim was to assess Lamb wave behaviour on the joint and determine frequencies at which the specific modes propagate into the skin and the stringer.
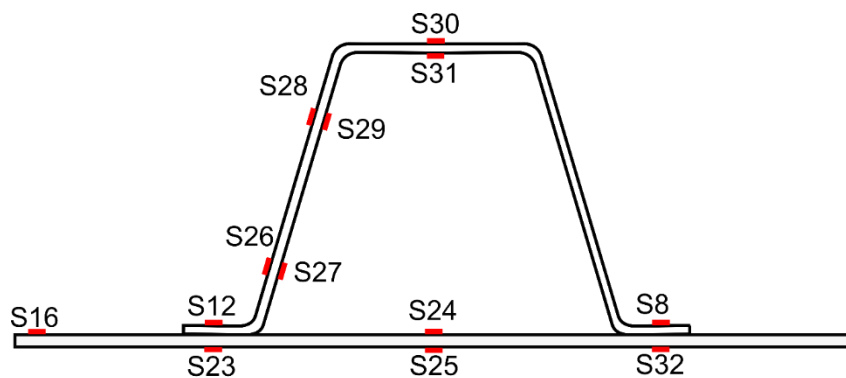
Figure 44 Sensors positions to qualitatively evaluate the wave propagation

Signals were actuated either from the end of the plate (S16) or from the joint (S12/S23) at both surfaces. Wave propagation through the joint and the subsequent propagation to the stringer

and/or to the skin, and finally to the joint on the other side was observed. The waveforms are shown for the frequencies of 50 kHz and 180 kHz, representing A0 and S0, respectively.

Figure 45 represents the actuation of the 50 kHz burst from the end of the plate (S16). At this frequency, only A0 mode is detected. If not distorted, the A0 mode is determined as an out-of-phase wave packet. However, the first joint cause the phase shift (a), then the wave packet propagates into both the skin (b) and the stringer (c). A0 is also identified on both surfaces of the second joint (d). However, based on the time of arrival, the first wave packet is identified as A0 mode guided by the skin, not the stringer. The same scheme for the frequency of 180 kHz is shown in Figure 46.
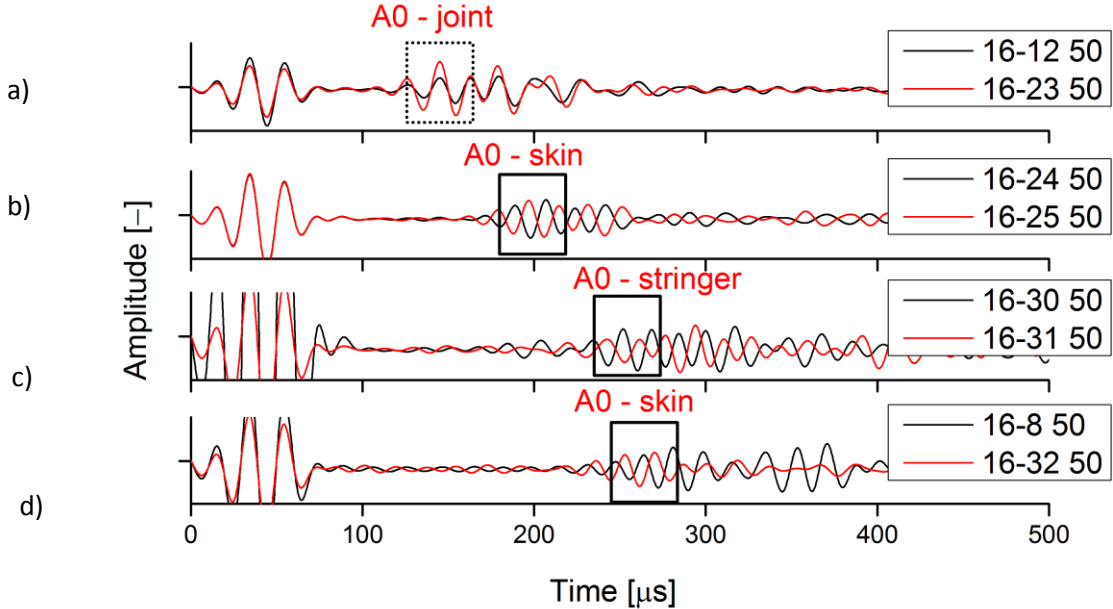
Figure 45 Wave transmission into the skin and into the stringer at the frequency of 50 kHz

At the frequency of 180 kHz, S0 mode is identified as in-phase signals. S0 is detected at the skin part of the first joint (a), then propagates into both the skin (b) and the stringer (Figure 46c), and finally detected at the skin part of the second joint (d). S0 mode is reliably detected only at the skin part of the joint. The joint evidently causes a significant energy loss leading to evaluation inability when propagating through the stringer. The first arrived S0 mode propagated through the skin.
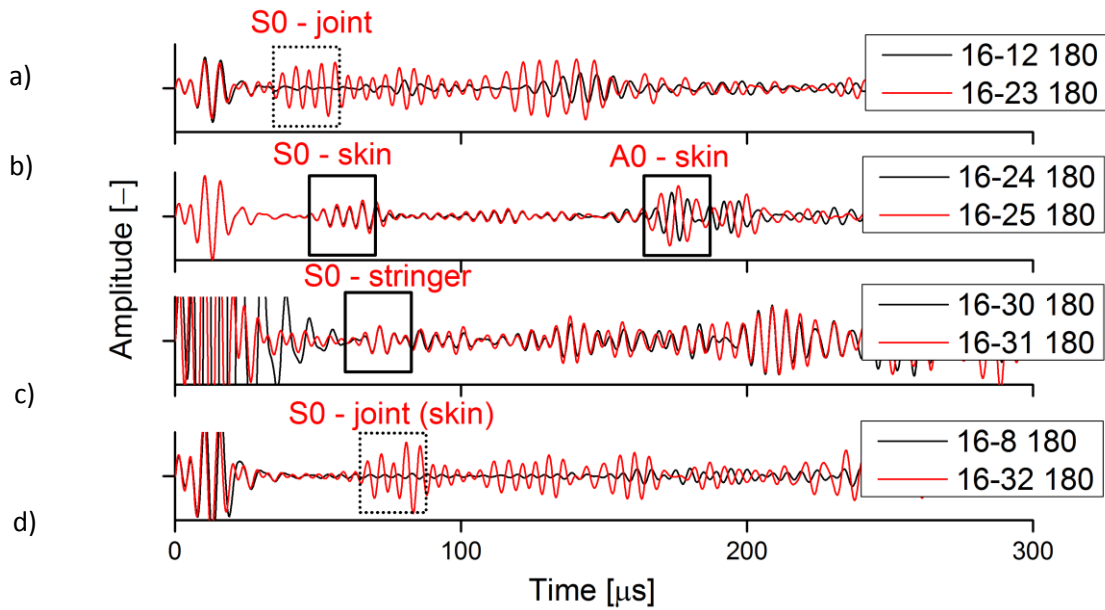
Figure 46 Wave transmission into the skin and the stringer at the frequency of 180 kHz
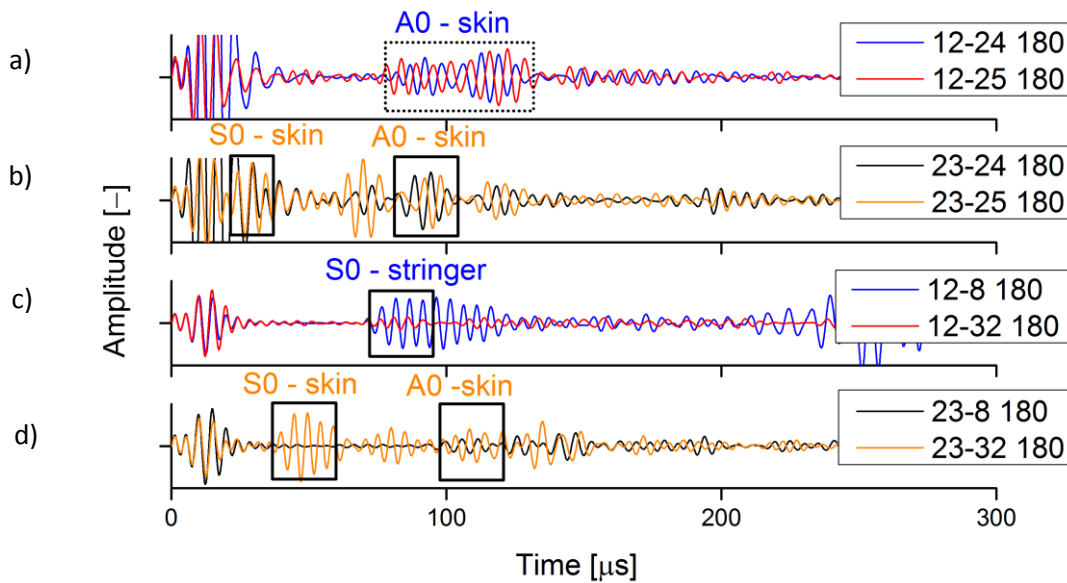
Figure 47 Wave propagation actuated from the area of the joint at the frequency of 180 kHz

The wave propagation from the first joint to the second joint at the frequency of 180 kHz is described in Figure 47. Based on the location of the transducers (skin or stringer part of the joint), the wave packet propagates through none, one or two joints, hence either along the skin or the stringer.

Both S0 and A0 modes propagate into the skin when actuated at the skin part of the first joint (S23), as seen in Figure 47 b. When reaching the second joint, both modes are detected at the

skin part of the joint, while only A0 mode is clearly detected on the stringer part of the joint (Figure 47 d). This indicates that, unlike A0 mode, S0 mode does not propagate through one joint or does with significant attenuation. Indeed, A0 mode propagates into the skin when actuated at the stringer part of the first joint (S12), as seen in Figure 47 a. However, the first wave packet at the second joint is identified as S0 mode propagated through the stringer (Figure 47 c). S0 is detected by S8 with significant amplitude (propagation through no joint), while by S32 with significant amplitude loss (propagation through one joint). Propagation through the skin would mean propagation through two joints, which is for S0 is immeasurable. Therefore, propagation only through the stringer is ensured by this configuration.

Sensors mounted on the stringer part of the joint (S12 and S8) are exploited for impact damage evaluation. Figure 48 and Figure 49 show wave packets A0 and S0, respectively, propagating through the cross-section line according to the sketch in Figure 44. A0 mode at the frequency of 50 kHz and S0 mode at 180 kHz were actuated. The wave packets actuated by S12 propagate along the stringer and are detected by sensor pairs S26/S27, S28/S29, S30/31, and finally S8/S32 (Figure 48 a-d, Figure 49 a-d). However, A0 mode at the frequency of 50 kHz propagates also into the skin. Therefore, the first wave packet detected by sensors S8/S32 is A0 propagated through the skin, and the third one detected by S8 is based on the time of arrival considered as A0 propagated through the stringer (Figure 48d). On the contrary, S0 mode propagated through the stringer is the first detected wave packet at S8 for 180 kHz (Figure 49d). In that case, propagation through the skin would be propagation through two joints and, based on previous conclusions, a significant attenuation unable wave packet detection.
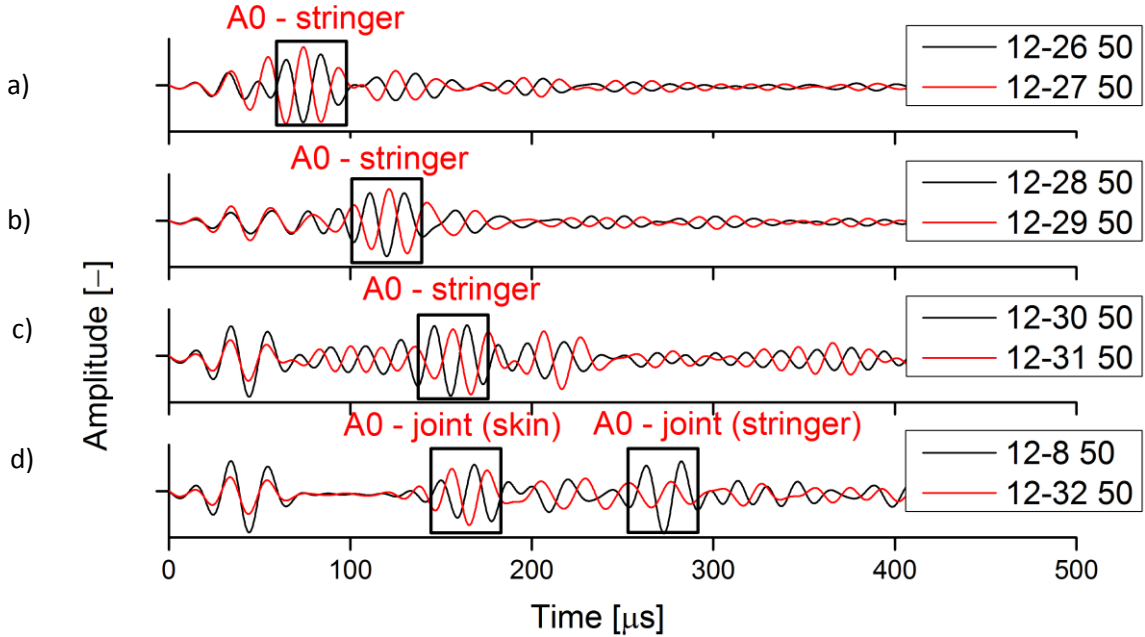
Figure 48 Wave propagation along the stringer cross-section at the frequency of 50 kHz
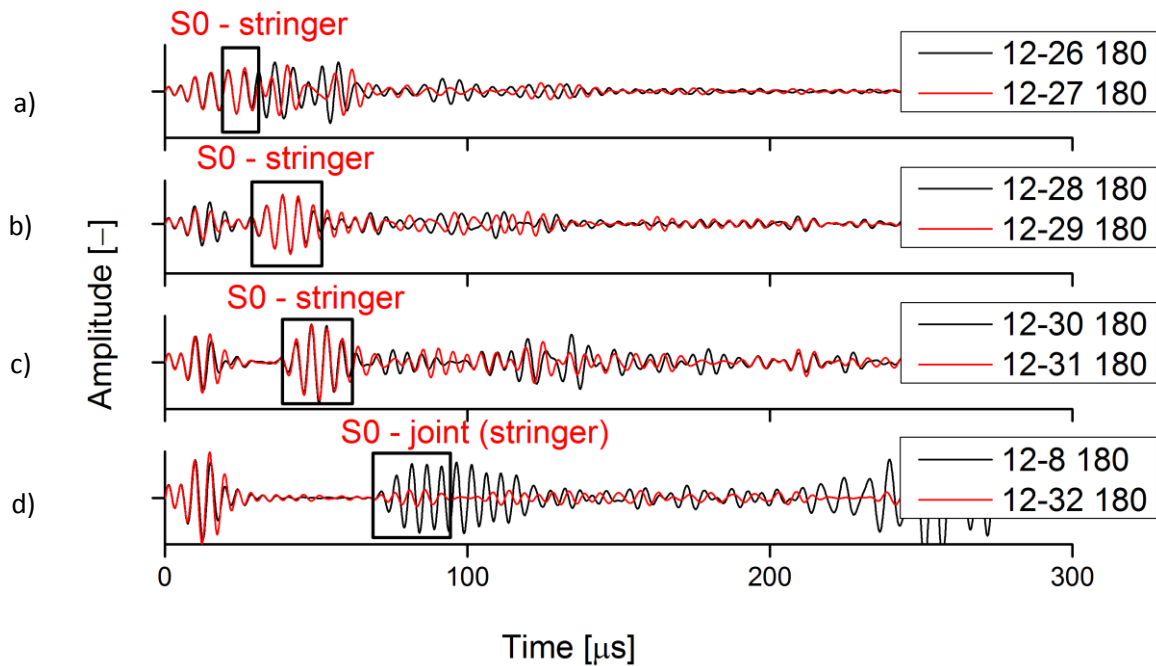
Figure 49 Wave propagation along the stringer cross-section at the frequency of 180 kHz

Based on the described measurements, S0 mode was chosen for impact damage evaluation at the stringer part of the specimen. The reasons are as follows:

1. A0 mode at frequencies up to 100 kHz was more sensitive to the introduced damages (based on the measurements on plates). However, it was impossible to reliably identify at all actuator–sensor paths which wave packet propagated through the stringer. The first detected wave packet was identified as the wave packet propagated along the skin.

2. S0 mode at the frequency of 180 kHz does not propagate dominantly into the skin due to the presence of the joint. Therefore, the first detected wave packet was identified as the wave packet propagated through the stringer.

8.3.3 Impact damage - Omega1

Three impact damages in total were introduced to the test specimen Omega 1. Parameters of individual impacts in terms of energy and depth are specified in Table 4. The test specimen Omega 1 with marked impact location and configuration of sensors is seen in Figure 50.

Table 4 Impact specifications

Omega 1			Omega 2		
I1*	15 J	0.18 mm	I1**	20 J	0.49 mm
I2*	30 J	0.55 mm	I2**	35 J	1.04 mm
I3**	40 J	0.99 mm	I3**	40 J	1.29 mm

*16 mm impactor, ** 1 inch impactor
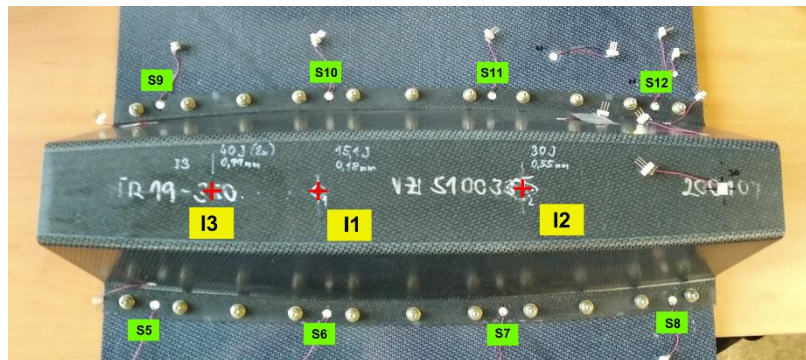
Figure 50 Omega 1 – configuration of sensors and marked impact location

Figure 51 shows that impacts I1 and I2 introduced with the ½-inch impactor could not be localized clearly. On the other hand, the location of I3, which was introduced by a 1-inch impactor, was detected positively. Impact damage areas were determined by means of UT A-scan. The impact damage area of I1 and I2 is significantly smaller than the area of I3.
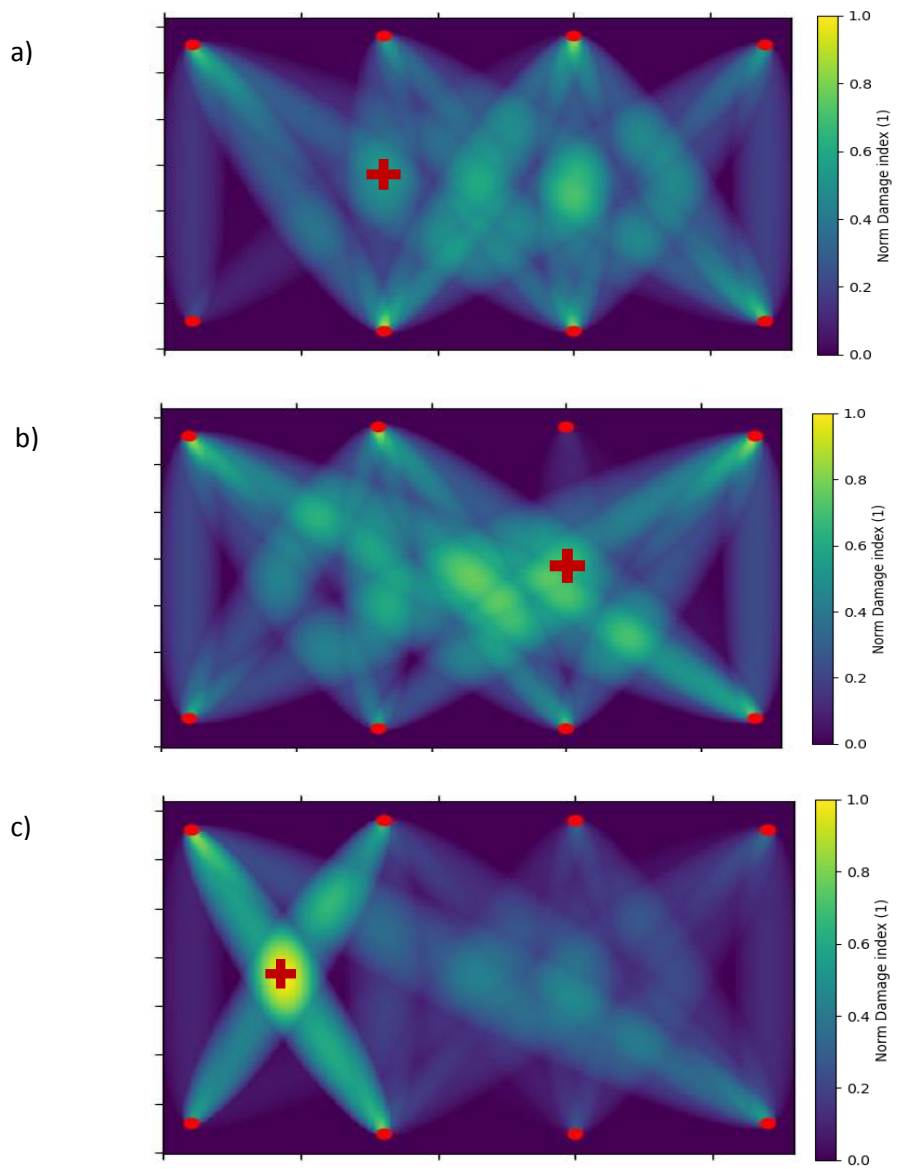
Figure 51 Impact localization using RAPID a) I1, b) I2, c) I3

8.3.4 Impact damage– Omega 2

The test specimen Omega 2 with marked impact location and configuration of sensors is seen in Figure 52.
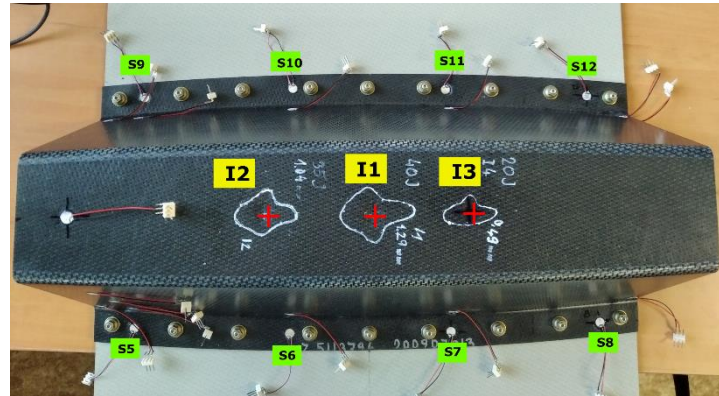
Figure 52 Omega 2 – configuration of sensors and marked impact location

Figure 53 a-c shows that all impacts (I1, I2, and I3) introduced by the 1-inch impactor were localized correctly. In addition, the evaluation of two impacts at once was performed correctly (Figure 53 d).

Impact damage areas were marked by UT A-scan. Based on these measurements, impact damage areas of I1, I2, and I3 at the test specimen Omega 2 are much larger than impact damage areas at the test specimen Omega 1.
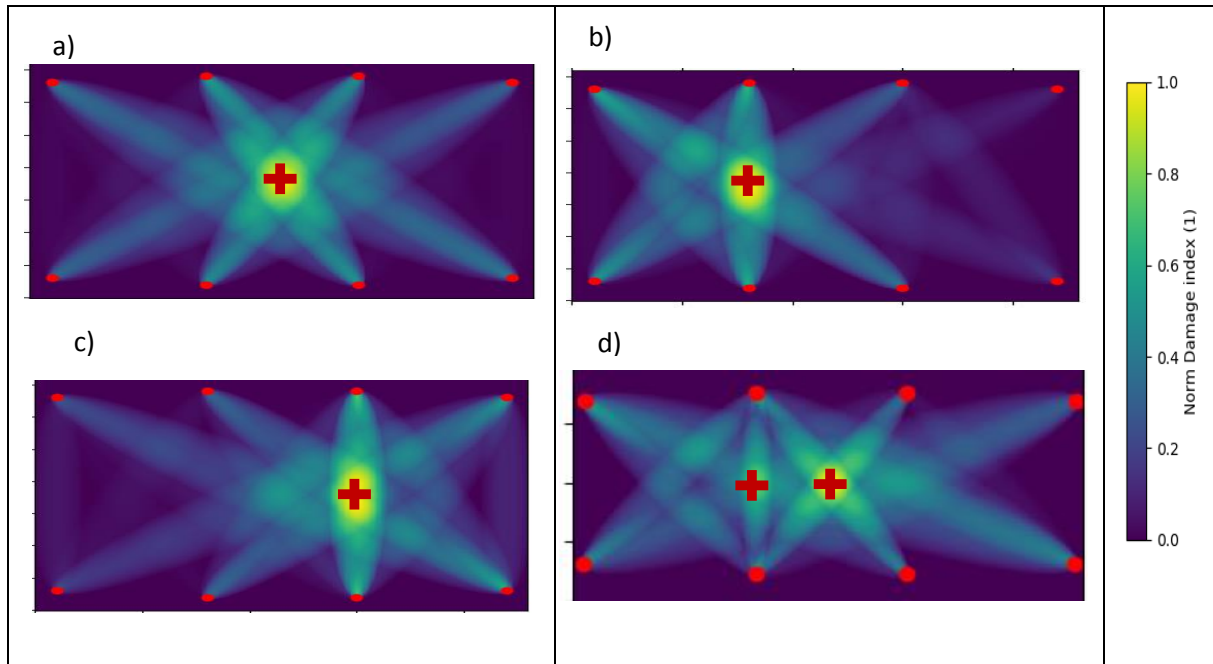
Figure 53 Impact localization using RAPID a) I1, b) I2, c) I3, d) I1+I2

Additional sensors were mounted on the test specimen Omega 2. Close to the positions of sensors S5 - S12 were mounted additional sensors. The former group of sensors placed at the area of the joint was designated as outer and the new group of them as inner. The inner sensors were mounted very close to the outer ones but onto the stringer web. The positions are seen in Figure 54.
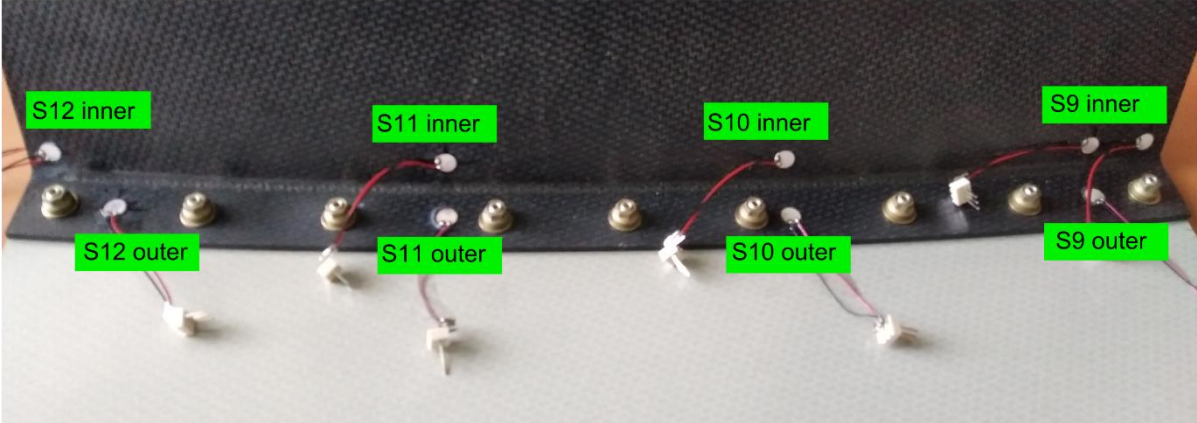
Figure 54 Inner and outer sensors configuration

Evaluation of measurements utilizing the outer or inner group of sensors was performed. It was found that both configurations can be used to impact damage detection (Figure 55).
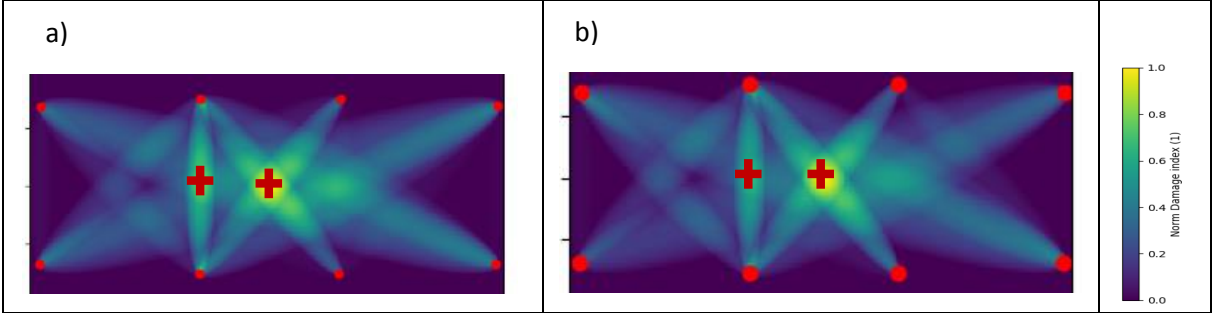
Figure 55 Comparison of impacts I1 and I2 localization using a) inner sensors configuration, b) outer sensors configuration

8.3.5 Conclusion

Based on the qualitative measurements at frequencies of 50 kHz and 180 kHz, the following conclusions have been drawn:

1. The propagation of the S0 mode at 180 kHz through the skin-stringer joint shows significant energy loss. One joint causes significant amplitude loss; both joints enable propagation completely. A0 is less sensitive to joints.

2. Actuating at the skin and propagating towards the joint, Lamb waves are detected phase-shifted at both surfaces of a skin-stringer joint. Further propagation into the skin and stringer shows phase alignment correspondingly to the specific mode (in phase displacements for S0 mode and out of phase for A0 mode).

3. Specific actuator-sensor configuration and frequency and mode selection can be exploited to ensure Lamb wave propagation only through the stringer, one joint, or both joints.

Based on impact damage assessment, the following conclusions have been drawn:

1. Suitable transducers configuration for impact damage detection within the stringer (section 2) is at the stringer part of the joint. For frequencies above 120 kHz, S0 mode propagation into the stringer is dominant. At these frequencies, propagation into the skin is eliminated by attenuation, and the modes are clearly identified. S0 mode at the frequency of 180 kHz was selected for evaluation. S0 mode was the first arrived mode for all exploited actuator-sensor paths.

2. A0 mode at lower frequencies (50 – 90 kHz) is suitable for impact damage assessment within the skin (section 1, section 2′, section 3). Based on the previous impact damage detection performed on plates, the A0 mode is more sensitive to the impact damage. Also, qualitative measurements and amplitude-frequency dependency showed that the A0 mode is dominant and clearly identified at lower frequencies.

3. Six impact damages were introduced into the stringer. Four of them were localized correctly. Impact damage boundaries were marked by ultrasonic A-scans. The two unidentified impact damages areas were significantly smaller than the other four. The method limitation exploiting S0 mode lies probably in the damage extent. The minimum damage extent for evaluation using the A0 mode has not been determined so far.

8.4 Adhesively bonded composite joints

This chapter was included in the manuscript Delamination/disbond propagation analysis in adhesively bonded composite joints using guided waves published in the Journal of Structural Integrity and Maintenance [d].

The research investigates debonding and delamination assessment by means of Lamb waves in adhesively bonded composite joints. Adhesively bonded wide CFRP panels with initial delamination were subjected to fatigue loading. First of all, preliminary measurements were performed. A segment of the phase velocity dispersion curve was constructed using frequency filtering and compared to calculations using the GUIGUW SW. Calculations were also used to verify Lamb wave propagation in this specific three-layer system. Also, a segment of the velocity dispersion curve was constructed for both thicknesses (single panel and the bonded section) by tracking the maximum amplitude peak. ToF shift was exploited as a damage parameter. Based on the sensitivity analysis, it was found that the A0 mode is more sensitive to delamination/debonding than the S0 mode. Quantitative evaluation was performed using sensors mounted on both surfaces of the bonded section. A linear relationship was established between delamination lengths determined by ultrasonic A-scans and time delays of A0 mode. Additionally, the RAPID algorithm was used to visualize the delamination/debonding extent.

8.4.1 Materials and methods

Adhesively bonded panels (wide single-lap shear) with initial artificial delamination, schematically seen in Figure 56, were made of CFRP with epoxy resin with the lamination sequence of $[0/45/90/135]_{2s}$. The bonded panels were 4.16 mm thick (2 mm + 0.16 mm of adhesive + 2 mm).

Several experimental techniques were exploited to evaluate delamination propagation in an adhesively bonded structure. During the fatigue test, standard ultrasonic pulse-echo A-scans and Lamb wave measurements were performed. After the test, macro fractographic images and metallography were utilized to assess the fracture surface and support Lamb wave measurement findings. The description is provided in the following sections.

The test specimen was subjected to fatigue loading. The maximum load of 120 kN with the load ratio of R=0.1 and the frequency of 7 Hz was applied. The delamination/debonding propagated approximately symmetrically from the central initially debonded section to both sides. The test was conducted until the final failure.
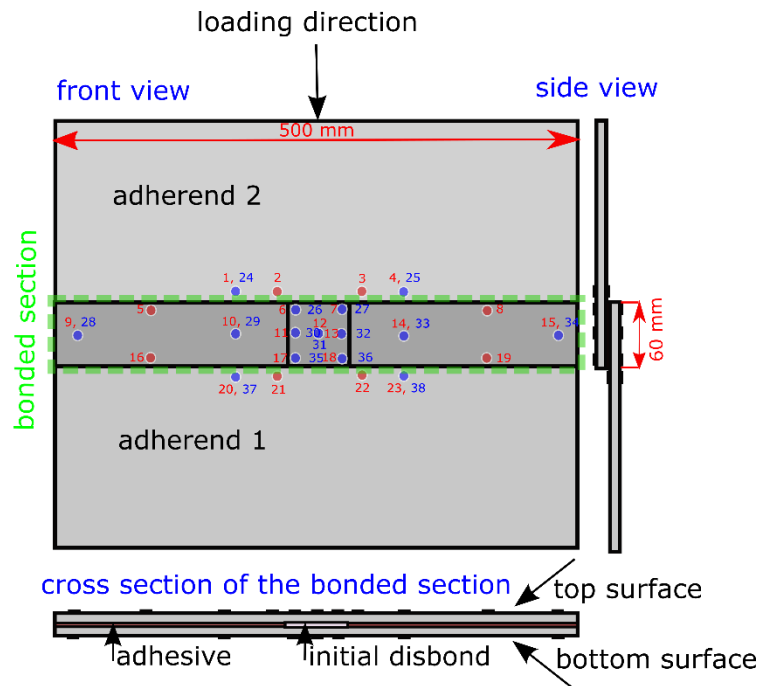
Figure 56. Schematic drawing of the bonded structure with transducers placement; red and blue numbers indicate front and back sensor placement, respectively.

Ultrasonic pulse-echo periodic inspections using a 20 MHz single element probe were performed to mark the actual delamination boundary. At the same intervals, Lamb wave measurements were performed. A total of 13 inspections were performed. For Lamb wave measurements, 38 PZT disc transducers were attached symmetrically to both surfaces of the structure to enable mode identification. Some of them were exploited for damage assessment. After the final failure, metallographic analyses of the debonded panels' cross-sections were performed to support findings based on Lamb wave measurements.

8.4.2 Assumptions and preliminary Lamb wave measurements

The propagation of A0 mode through the entire three-layer system (adherent-adhesive-adherent) is assumed. The wave of a suitable frequency propagates through the entire thickness of the bonded section, splits into two separate slower waves at one end of the debonded area, and, at the second end, adapts again to the bonded section. Based on dispersion curves, in the case of S0 mode, the wave would get faster when propagating along the delaminated section. Therefore, time delays are expected to be measured when delamination/debonding increases for the A0 mode while time advances for the S0 mode. The longitudinal cross-section of the specimen with the indicated scheme of the A0 wave propagation is shown in

Figure 57. A longer wavelength for the bonded section than for the delaminated part is also schematically illustrated for the particular frequency.
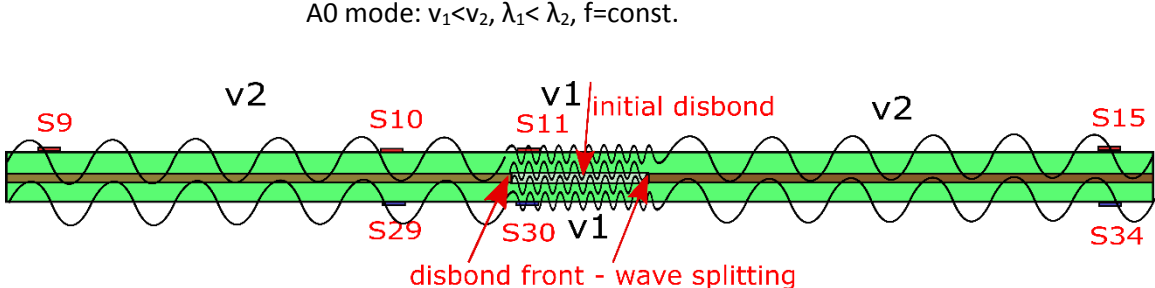
Figure 57. A0 mode propagation along the bonded section of adhesively bonded panels with an initial disbond

Lamb wave frequency tuning was performed to generate a clearly shaped and high amplitude A0 mode. The suitable frequency was determined to be 50 kHz. A segment of the velocity dispersion curve was constructed for both thicknesses (Figure 58 a) by tracking the maximum amplitude peak over two close sensors. This velocity value is close to the phase velocity. Tracking the envelopes to determine the group velocity was enabled by the envelope's distortion. Up to 100 kHz, low amplitude S0 mode was hidden in the crosstalk, and only A0 was visible, while in the frequency range of 190 – 210 kHz, velocity for both modes was determined.

GUIGUW SW utilizing the SAFE method was used to support the above assumptions. A segment of the phase velocity dispersion curve for the bonded section was constructed experimentally using frequency filtering and compared to results obtained by the SAFE method (Figure 58 b).
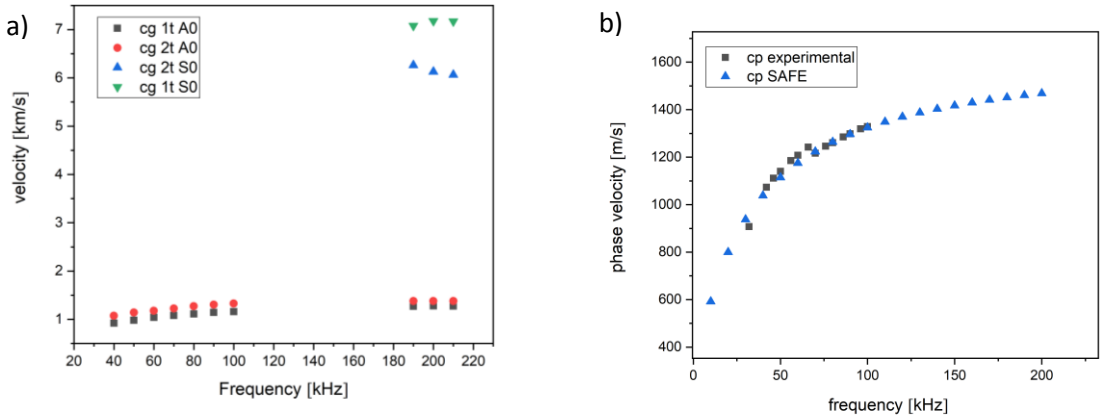
Figure 58. A segment of a dispersion curve for a) the single panel (1t) and the bonded section (2t), b) comparison of experimentally determined and calculated phase velocities for the bonded section (2t)

Preliminary measurements performed on the bonded section using A9-S10/S29 and A9-S11/S30 proved the propagation of the A0 mode by clear out-of-phase signals through the whole three-layer system and splitting into two asymmetrical waves within the debonded area (Figure 59). The A0 mode reaches the debonded tip, splits into two waves, slows down, and at the end of the debonded area, adapts again to the bonded structure and accelerates. Therefore, a suitable arrangement of sensors to measure time delays is directly linked to the disbond/delamination length.
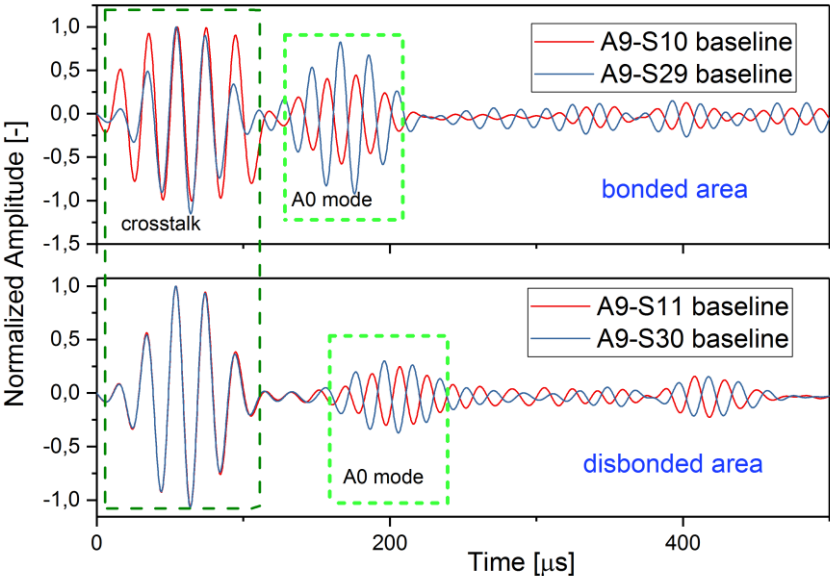
Figure 59. Baseline measurements of the A0 mode in the bonded and debonded area

8.4.3 Frequency sensitivity to the time shift

The measurements were analysed after the test. The sensitivity analysis was performed to choose a suitable frequency for the evaluation. Figure 60 shows ToF shift from the perspective of different frequencies and modes related to the delamination length (Figure 60 a) and the number of cycles (Figure 60 b). The plots correspond to the actuator-sensor path A9-S11. Analysis was performed for five frequencies for the A0 mode and two frequencies for the S0 mode. As stated before, time delays were measured for A0 mode as delamination propagated and time advances for S0 mode by tracking the maximum peak. S0 mode was possible to extract for the frequency of 100 kHz and 190 – 210 kHz. The maximum time advance (for the maximum delamination length) was determined to be 0.8335 µs for the frequency of 100 kHz. A0 mode was much more sensitive. The maximum time delay of 17.167 µs was determined for the frequency of 40 kHz. However, the frequency of 50 kHz with a maximum time delay of 16.167 µs was chosen for further evaluation. The amplitude was higher than for the 40 kHz

wave, and part of the mode was no longer hidden in the crosstalk for the close actuator-sensor paths.
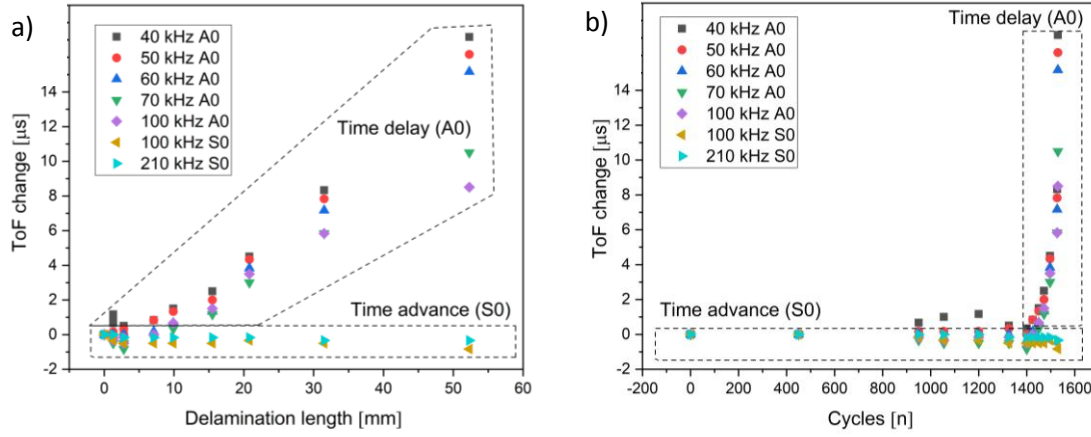
Figure 60. ToF delay at different frequencies and a) delamination lengths, b) cycles counted in thousands

8.4.4   Calculation of delamination length

Sensor paths along the central line of the structure, A9-S11/S30 for the left side of delamination propagation and A15-S13/S32 for the right side, were chosen for analysis (Figure 61). Debonding started to propagate from the four corners of the initial square disbond. Significant damage, measurable using the sensors in the central line (continuous damage), occurred later in 1 425 000 cycles (93% of the fatigue life). Seven measurements were performed since the damage became continuous.

Delamination lengths were calculated using the equation (78) derived in the reference [b]:

$$a_n = \frac{(v_2 v_1) \Delta t}{v_2 - v_1},$$

where v_1, v_2 are A0 mode velocities for the single panel and the bonded section, respectively, and Δt designates the time delay corresponding to the delamination length a_n.

Calculated delamination lengths and those determined at the central line of the bonded section using ultrasonic A-scans did not match well. The mean absolute percentage error was 32.07%. The error was probably caused by the velocity values, which were determined for the two exact thicknesses – the single panel and the bonded section (adherend – adhesive – adherend). In fact, there was a mixture of debonding and delamination propagation dividing the bonded

section into the adherend + adhesive + a few layers of the second adherend and the corresponding rest of the bonded section. So, the actual velocities were different from those determined experimentally.
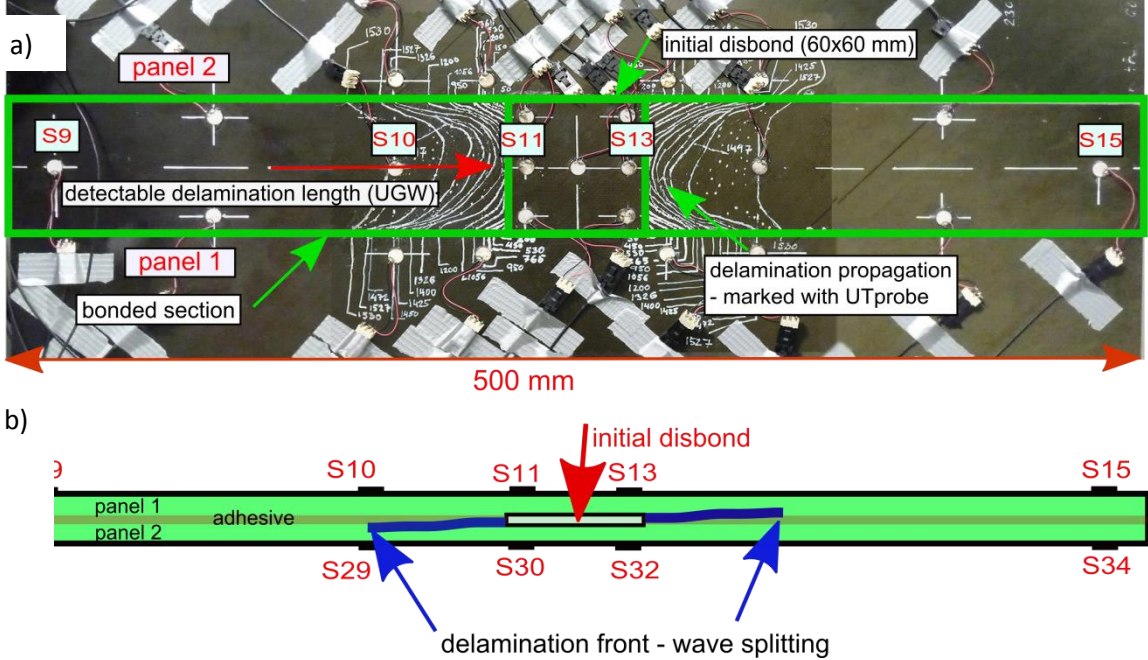
Figure 61. Delamination propagation in adhesively bonded panels a) front view, b) cross-section schema

However, time delays were additionally analysed and compared to the baseline measurement for four sensor paths in the central line, as stated above. If the debonding propagated symmetrically in the adhesive layer, Lamb waves actuated by S9 and S15 would propagate in two identical thicknesses, and the time delays compared to the baseline measurements of sensors S11 + S30 and S13 + S32 would also be identical, and calculations using the equation (78) would match. However, time delays differed on both sides. Time delay is directly linked to the velocity and, for the given frequency, to the thickness of the structure. Therefore, different time delays detected using sensors on the top and bottom surfaces (panel I and panel II) indicated that the initial debonding in the middle adhesive layer changed into the delamination propagating in adherend 1 or 2, dividing the bonded section into two asymmetrical parts. The least-squares method was utilized to estimate the linear relationship between the ToF and delamination length. However, the linear relationship is valid only for higher delamination lengths propagating in one layer. Therefore, the regression calculates only with higher delamination values. A linear relationship between delamination length and time delay within the central line is plotted in Figure 62. The slope of the linear function indicates the rate of the slowdown of the velocity, hence the structure thickness. The greater

the slope of the curve is, the thinner the delaminated structure. Based on these results, the delamination did not propagate into the adhesive but to the left side in adherend 1 and the right side in adherend 2. Described qualitative analysis was supported by means of metallographic analysis.
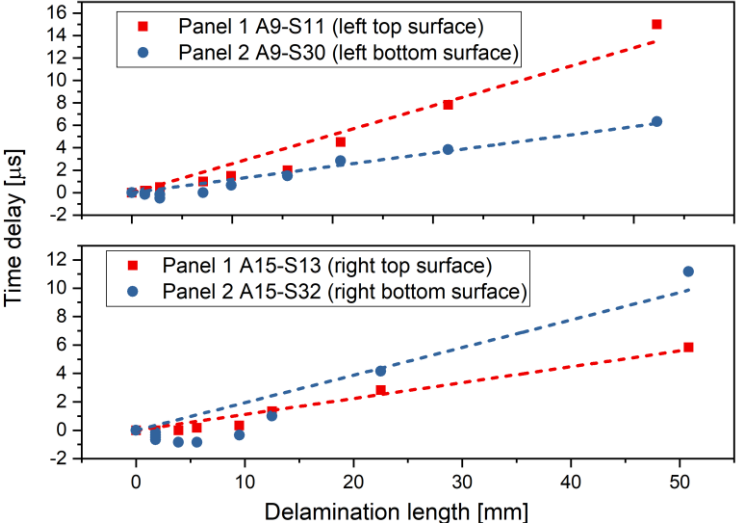
Figure 62. Relationship between time delays and delamination length for the left and right side

8.4.5 Metallographic analysis

Results indicating delamination propagation in different adherents were confirmed using detailed macro fractographic images and, also by metallographic analysis. The fracture surface of panels I and II is shown in Figure 63 a) and b).
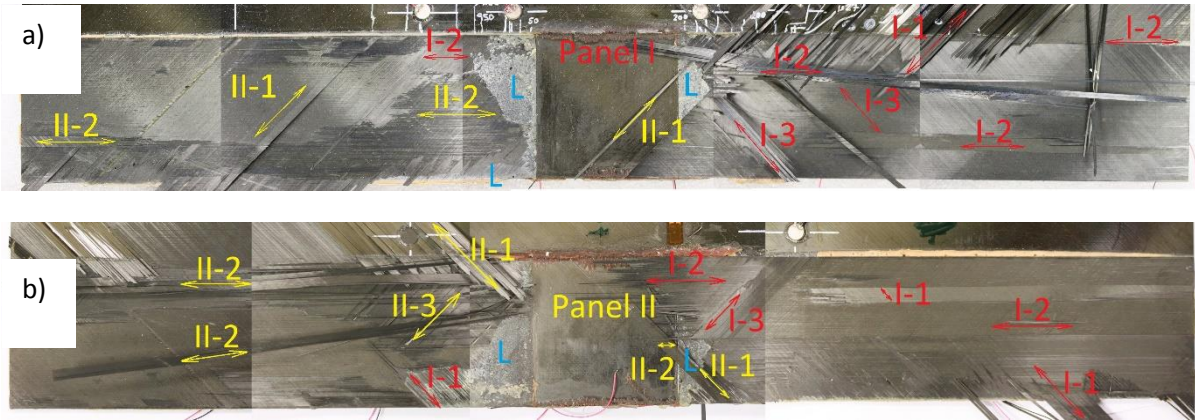
Figure 63. The fracture surface of both panels; the first number designates the panel, and the second number designates the layer

Debonding occurred at the beginning in the adhesive (L), followed by delamination in different layers (1. – 3. layer). The fracture surface of the panel I include adhesive and up to two remaining layers of panel II on the right side. There are up to three missing layers of the panel I on the left side. The fracture surface of panel II shows the opposite markings – the left side shows missing layers, and the right side includes adhesive and layers of the panel I.

Metallographic cross-section samples were prepared from the left and right sides of the panel I. Figure 64 on the left side clearly shows 16 layers of the panel I, the adhesive layer, the first layer, and part of the second layer of panel II and on the right side, only 14 layers and part of the 15th layer of the panel I.
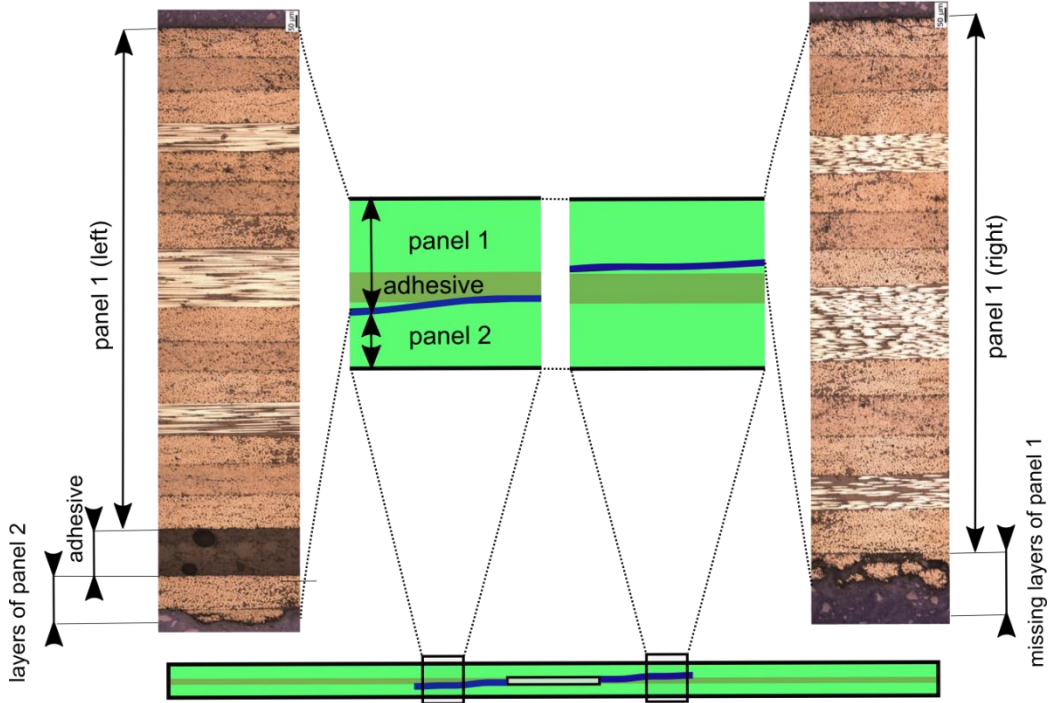
Figure 64 Metallographic samples of the cross-section in the context of the delaminated joint

8.4.6 Damage visualization

Visualization using the RAPID was performed. The A0 mode was extracted for all actuator-sensor paths based on the sensitivity analysis. Considering the proximity of some transducers, a 50 kHz waveform was hidden in the crosstalk, so the 70 kHz A0 mode was used. ToF delay was exploited as a damage-sensitive parameter. An example of A0 wave packets at two

different stages of the fatigue test compared to the baseline measurement is illustrated in Figure 65. The structure was divided into segments which were combined after the analysis.
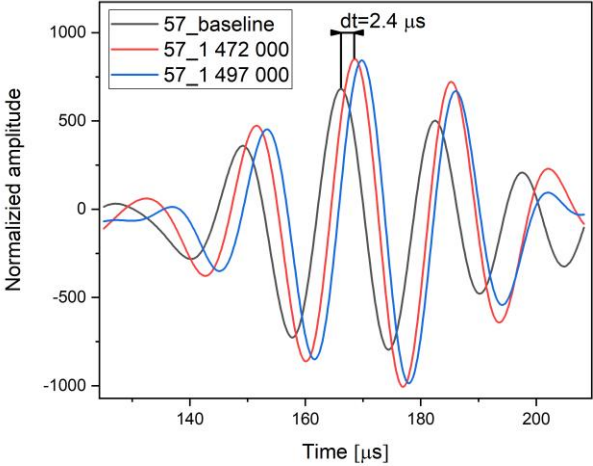
Figure 65 Extracted A0 mode at three different damage states

The resolution of the RAPID algorithm is based primarily on the number of sensors. Therefore, visualization of that complicated delamination/debonding propagation represents an informative character. Damage localization can be improved by dividing the sensor network into segments. Damage visualization on the left side was combined using two segments. The first segment contained three sensors (three actuator-sensor paths), and the second segment contained nine sensors (36 actuator–sensor paths). Figure 66 and Figure 67 show damage visualization at 450 00 cycles (29.4 % of the fatigue life) and 1 472 000 cycles (96.2 % of the fatigue life). At 450 000 cycles, delamination started to propagate from the corners. Time delays were measurable. However, the visualization did not show any severe damage. At 1472 000 cycles, the visualization matches more the actual state.
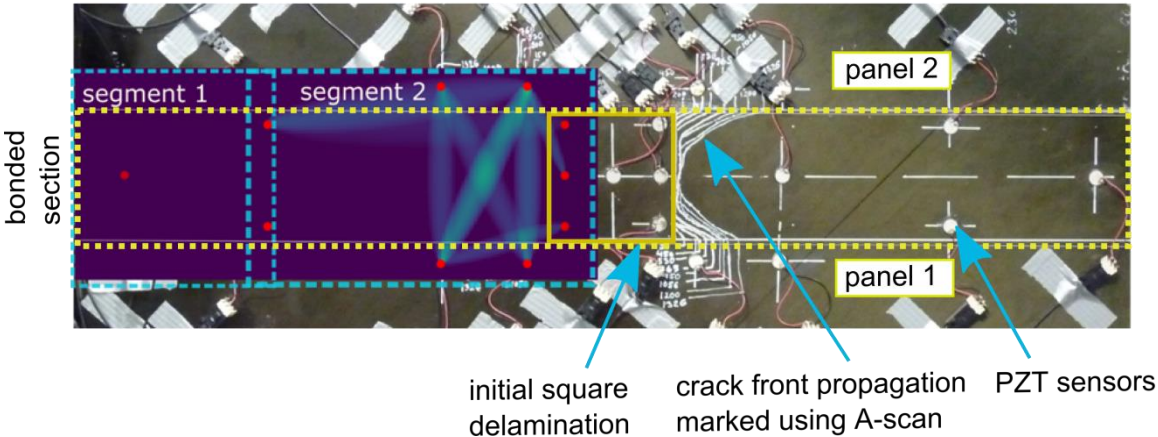
Figure 66 Damage visualization at 450 000 cycles (29.4 % of the fatigue life)
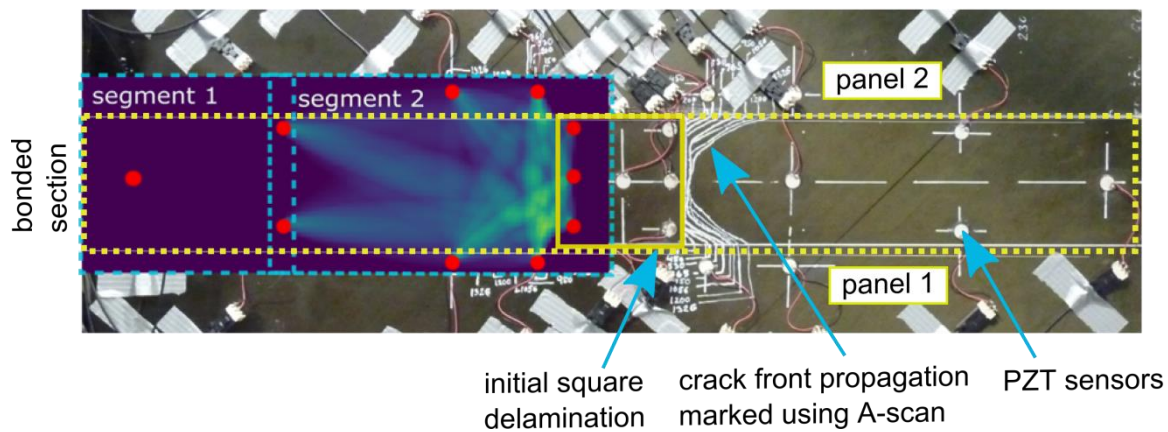
Figure 67 Damage visualization at 1 472 000 cycles (96.2 % of the fatigue life)

8.4.7 Discussion and conclusion

These measurements aimed to experimentally confirm the approach of delamination/debonding propagation assessment in an adhesively bonded structure using ToF delay of the A0 mode. A segment of the velocity dispersion curve was experimentally constructed by tracking the maximum peak amplitude for both sub-structures: the single panel and the bonded section. The phase velocity determined using the frequency filtering was compared to calculations performed by GUIGUW SW. Additionally, measurements performed using sensors along the central line of the bonded section confirmed propagation of the A0 mode within the full thickness and splitting of the wave at the disbond tip into two slower asymmetrical waves. Sensors were attached to both surfaces symmetrically, and clear out-of-phase signals indicating A0 mode were identified.

ToF delays were recorded as the delaminated area increased. However, time delays varied with the side of propagation (left or right) and the surface (panel I or panel II) of the sensor placement. The most likely explanation for the different time delays was different velocities implicating different thicknesses. These results showed the linear relationship between time delays and delamination lengths determined using the standard UT pulse-echo. The slope of the linear function indicated the velocity slowdown, which differed for four sensors placed on the left and right sides and both surfaces of the bonded section. The experimental investigation led to the conclusion that the difference in the slowdown was caused due to the asymmetrical delamination, which split the bonded structure into parts with different thicknesses. Therefore, precise calculations led to significant errors. The macroscopic overview of the fracture area indicated that delamination propagated on each side in a different layer. Therefore, a detailed metallographic analysis was performed, confirming previous assumptions and findings.

Finally, RAPID algorithm was used to visualize the damage. ToF delays were exploited and recalculated into a damage index. The approach of combining different segments was used to avoid false localization of the damage. The purpose of the visualization was not the accuracy but information in which segment the delamination/debonding occurred. Although preliminary measurements indicated the most sensitive frequency of A0 mode was 40 – 50 kHz, the proximity of actuator–sensor pairs enabled the extraction of the waveforms due to the crosstalk; therefore, a 70 kHz wave was used.

To conclude this research, the A0 Lamb wave mode was exploited to determine delamination propagation during the fatigue loading. In the low-frequency range of the dispersion curve for the A0 mode, the velocity decreases with a decrease in thickness. Delaminated or debonded sections of the structure represented the thinner part. The novelty of this analysis lies in the identification of the specific adherend in which delamination propagates to both sides using only six sensors. Different ToF delays recorded on symmetrically mounted sensors on both surfaces served as an indicator. The findings were confirmed by metallographic analysis. During the fatigue test, significant ToF delays in the central line of the bonded section were detected at 93% of the fatigue life. Earlier detection can be measured using sensors placed at the corners of the initial delamination. Additionally, RAPID algorithm, which is usually used for one-time impact damage detection, was used to visualize the damage extent. In this case, RAPID was exploited during the continuous fatigue test. The first damage detection was visualized in 29.4 % of the fatigue life.

9 Thermal dependency

Lamb waves are formed by portions of longitudinal and transversal motions. Their velocity is a material constant for a given temperature. As well as mechanical properties, the velocity of elastic waves varies with temperature. Generally, the velocity decreases with increasing temperature. The temperature dependency of Lamb wave velocity on the temperature is essential since the ToF change is often used as a damage-sensitive parameter. Then, either the temperature change needs to be compensated, or identical environmental conditions must be ensured.

The following experiments were performed for both isotropic and anisotropic structures to understand how the temperature influences the velocity. A controlled experiment in an environmental chamber was performed utilizing a composite sandwich structure. Afterward, the plate was subjected to two impact damages. All three measurements – baseline, after the first impact, and after the second impact was performed in slightly different temperatures. The second experiment exploited real operational conditions. Several flight tests were conducted with transducers mounted on an aluminium alloy fuselage skin of an ultralight aircraft. Operational conditions of an aircraft include the temperature changes with the flight altitude. According to the International standard atmosphere (ISA), there is a direct linear dependence of the air temperature on the altitude valid up to 36 000 feet. The temperature lapse rate decreases at the rate of approximately 2 °C per 1 000 feet. It is assumed that the temperature of the outer skin of an aircraft, changes correspondingly with the air temperature. Lamb waves propagating in such structural parts are also naturally affected by changing altitude. Therefore, Lamb wave signals in different flight altitudes, hence the temperatures were examined.

9.1   Laboratory controlled experiment

A part of this chapter was published as Temperature and damage-affected Lamb wave signals in composite sandwich plate within the EWSHM2022 conference [e].

A sandwich plate with CFRP skins and a foam core with dimensions 530×225 mm, including sensor locations and impact locations, is presented in Figure 68. Standard environmental tests are usually performed for the temperature range from -55 to +80 °C. This range corresponds to the operating conditions of an aircraft. However, the temperature range of -50 to + 50 °C with the step of 10 °C was considered sufficient for this purpose.
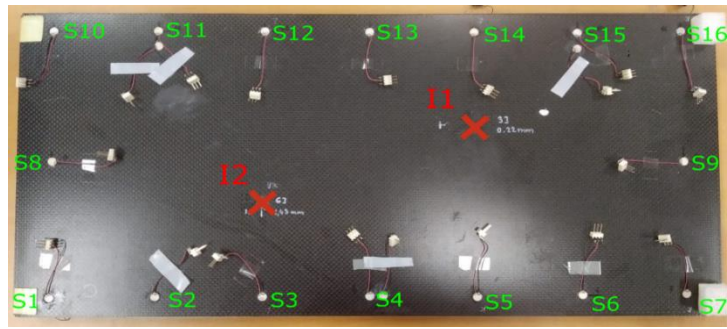
Figure 68 Sensor placement and impact damage location in the tested sandwich panel

Temperature-dependent signals were in agreement with theory and published research. It was proved that the ToF delay of the corresponding peaks increases with increasing temperature. Time delays compared to some baselines naturally imply a decrease in velocity; on the other hand, time advances indicate a velocity increase. Representative wave packets for both A0 and S0 mode are shown in Figure 69a andFigure 69c, respectively.
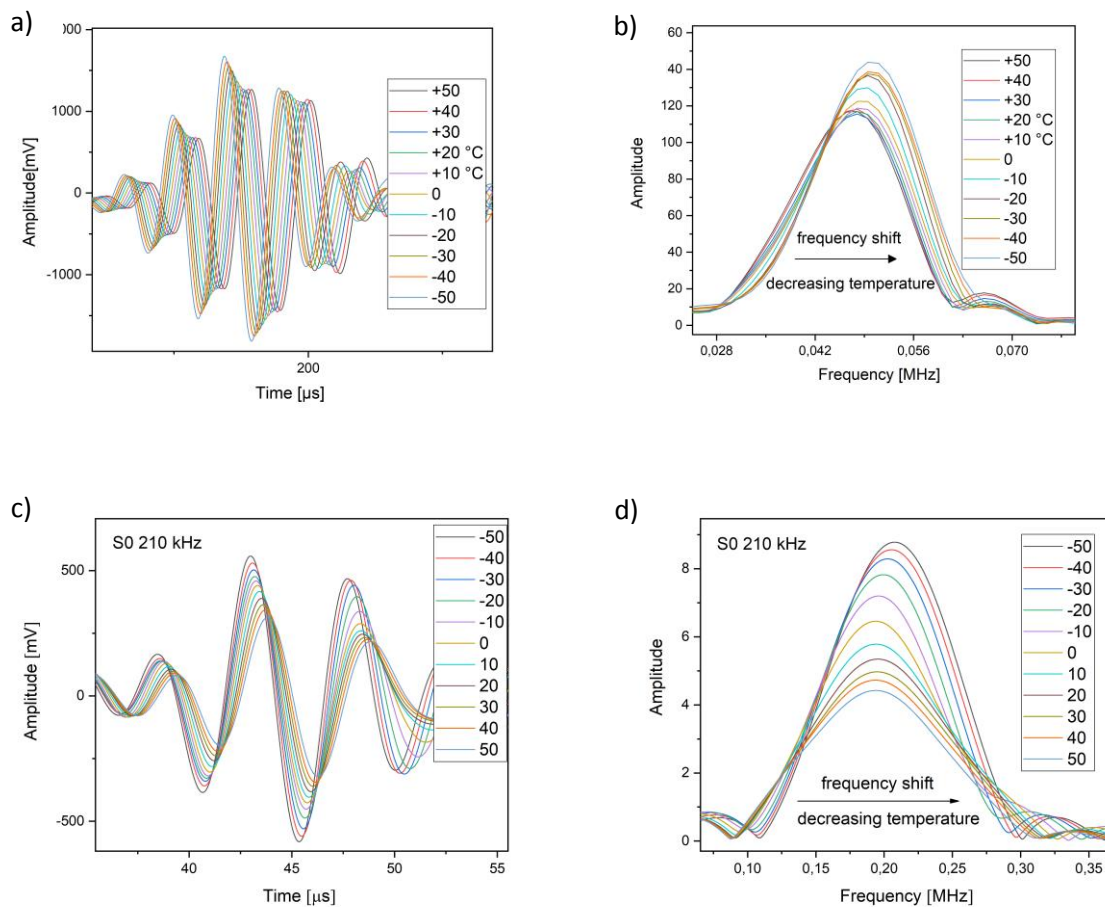
Figure 69 a) Wave packets at the different temperatures a) A0 in the time domain, b) A0 in the frequency domain, c) S0 in the time domain, d) S0 in the frequency domain.

Moreover, the frequency shift (compared to the actuation pulse) towards higher frequencies was observed with decreasing temperature for both modes (Figure 69b, Figure 69d). As a result, these findings must be considered when calculating wave velocities. Subsequently, this investigation focused on ToF measurements instead of the velocity calculation.

An example of the maximum peak time shift of a 50 kHz A0 mode for three temperatures is shown in Figure 70a. A relationship between the ToF and temperature Figure 70Figure 70b. Maximum peak shift is used for the further assessment of impact damage. The temperature – ToF relation is considered a "calibration curve" and is utilized for the exact temperature change determination during the damage assessment.
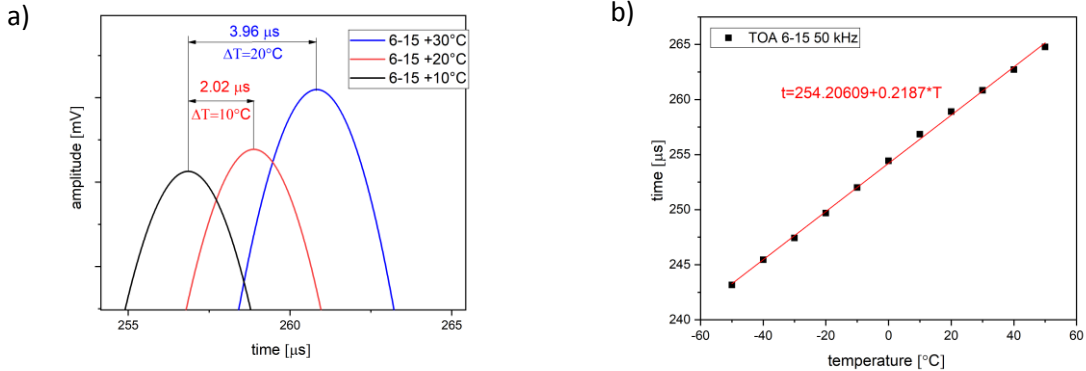
Figure 70 TOA of A0 mode at 50 kHz a) example of the maximum peak time shift, b) linear dependency on the temperature

ToF difference caused by changing temperature or damage cannot be distinguished on the extracted waveform. Figure 71 shows time delay caused by damage (a) and temperature (b).
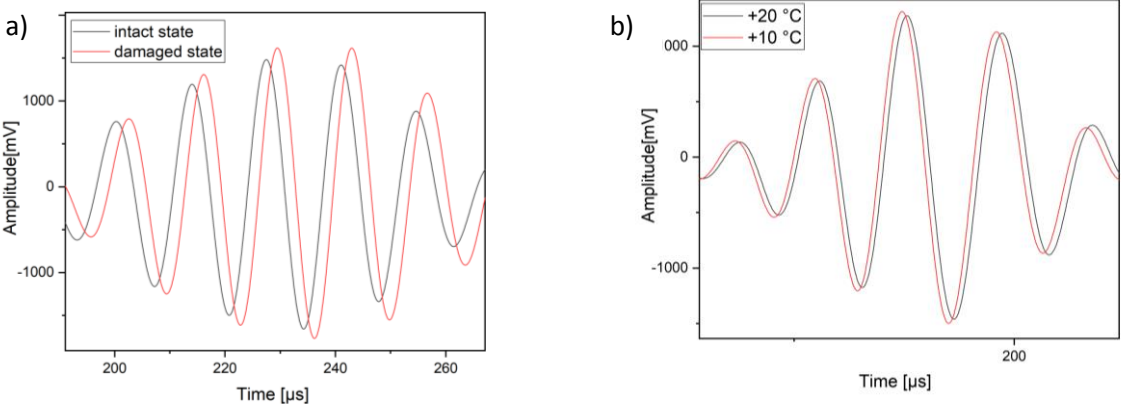
Figure 71 Time shift caused by a) damage, b) temperature

Nevertheless, analysing the longer part of the measured signal, the difference between those two situations is evident in Figure 72. Figure 72a shows a signal measured at 50 kHz for two temperatures with 10 °C difference. The first arrived wave – A0 mode is little affected. With increasing distance, the time delay of other reflections increases gradually. Since temperature influence increases within the signal time window, damage obviously influences only some parts of the signal, as seen in Figure 72b. The first arrived wave packet was delayed; some reflections probably propagated outside the damage area were not influenced, and some of them were.
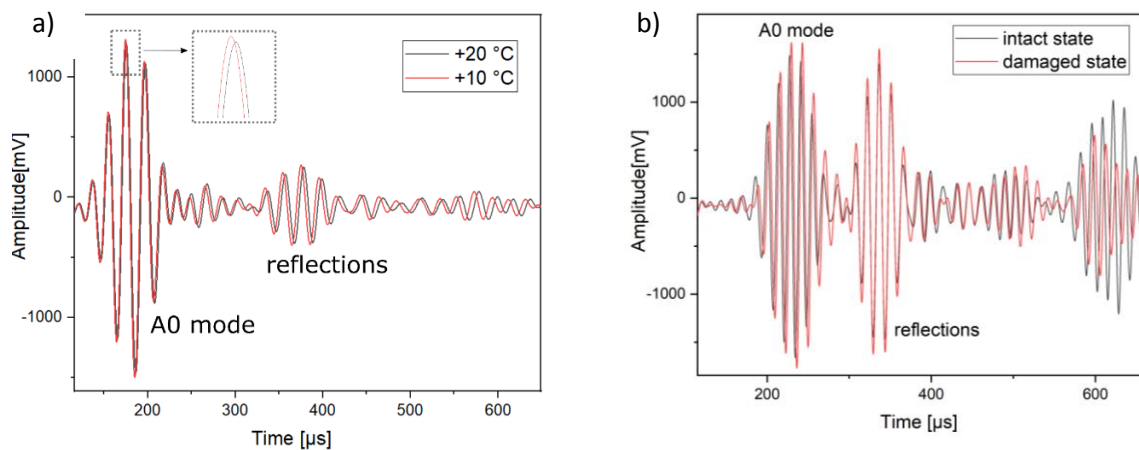
Figure 72 Signal comparison for a) two temperatures, b) intact and damage state

The sandwich plate was subjected to two impact damages. The evaluation was performed by means of the RAPID algorithm. ToF shift of a 50 kHz A0 mode was exploited as a damage-sensitive parameter. Three measurements – Baseline (BI), after Impact 1 (AI1), after Impact 2 (AI2) were conducted in slightly different temperatures. Signals exploited for impact damage detection were analysed qualitatively according to Figure 72. Signals AI1 for different actuator-sensor paths came earlier than BI measurements, indicating decreased temperature. On the other hand, signals AI2 showed time delays indicating increased temperature compared to the BI and AI1 measurements.

According to Figure 68, impact I1 (3J, 0.22 mm dent depth) was located on the direct line of transducers 5-14 and impact I2 (6J, 1.43 mm dent depth) on the direct line of 3-12. ToF of the 50 kHz A0 mode from the similar sensor pair of the same direction and distance (6-15) was evaluated for different temperatures. The linear relationship presented in Figure 70b led to the determination of the temperature change within the baseline measurements, after impact I1 and after impact I2. The temperature change was then calculated according to the equation:

$$\Delta T = \frac{\Delta t}{0.2187} \tag{79}$$

ΔT denotes the temperature change, and Δt denotes the measured time change.
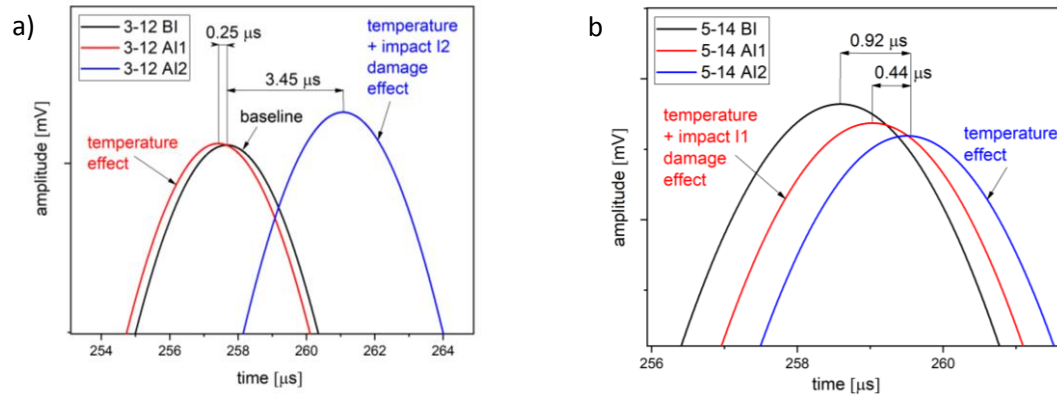
Figure 73. ToF of a maximum peak of a 50 kHz A0 mode with an effect of a) temperature and impact 2, b) temperature and impact 1

Figure 73 shows ToF of the maximum peaks of A0 mode for the direct lines through the impacts I1 (b) and I2 (a), indicating the temperature together with damage effect and temperature effect only. Time advance for the sensor pair 3-12 after I1 indicates only a temperature effect since the damage was caused later by I2. Time delay for the sensor pair 5-14 after I2 indicated temperature effect only since the damage was caused earlier by I1. Based on equation (79), the temperature decreased about 1.14 °C from the baseline measurement to the measurement AI1 and then increased about 2.01 °C after AI2. The total temperature effect from BI to AI2 measurement was about 0.87 °C. The set of time delays and advances was determined for all the actuator-sensor paths as input data for RAPID. Usually, without temperature changes, only time delays indicating damage are present for the corresponding paths, while for other paths, signals stay unchanged. Since RAPID calculates with numbers in the range of (0,1), normalizing by dividing the minimum value is usually sufficient. However, both positive and negative time shifts were present with a temperature effect. Therefore, min-max normalization was exploited. Figure 74 shows pseudo-images of I1 (a), I2 (b), and both I1 and I2 (c). Comparing the BI and AI2 datasets enabled imaging of both impacts. Impact I1 was less distinctive than I2 since its extent was significantly smaller. Impacts were still localized correctly; however, time shifts caused by the temperature effect caused noise in the pseudo image.
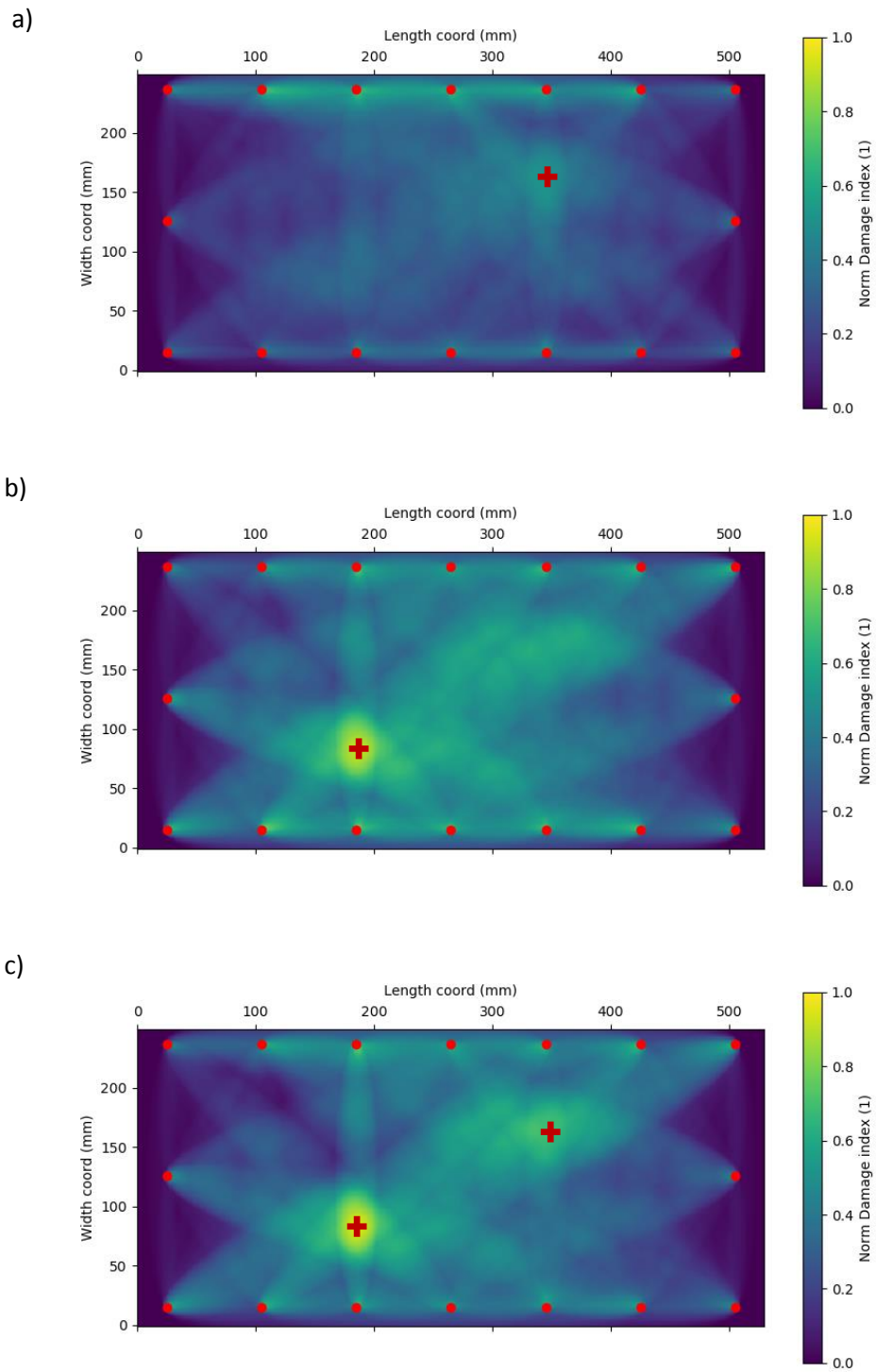
Figure 74 RAPID based pseudo images of a) impact 1, b) impact 2 and c) both impacts

9.2   Operational conditions test

An extended version of this chapter was published as Influence of operational and environmental conditions on Lamb wave signals within the EWSHM2022 conference [f].

Several tests were performed in real operational conditions. SmartLayers© sensors were mounted on the left side of the fuselage skin (Figure 75a) and on the cover located on the bottom of the fuselage (Figure 75b) of Eurostar EV 97 ultralight aircraft. Several measurements using the Acellent ScanGenie II were performed to examine the possibility of using the system in real environmental conditions.
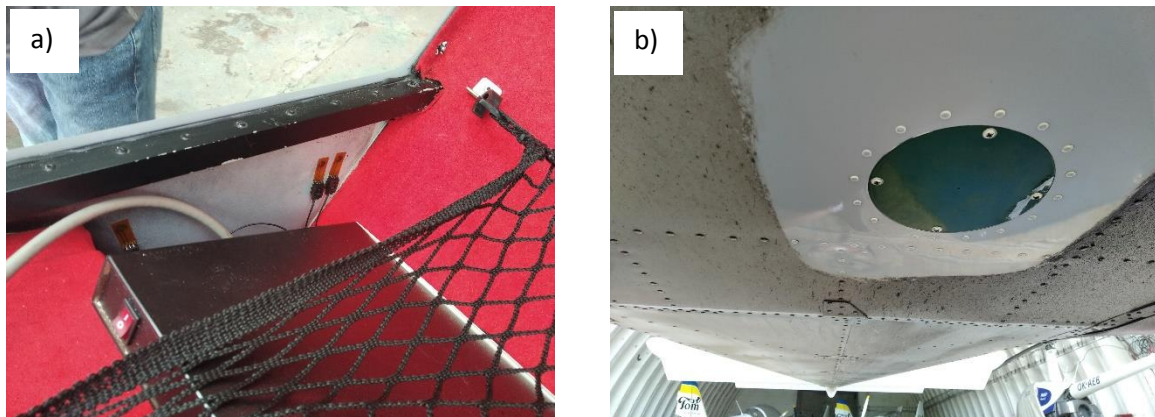
Figure 75 Sensor placement a) side fuselage skin, b) cover on the bottom of the fuselage

Figure 76 shows data for the frequency of 80 kHz (a) and 180 kHz (b) measured on the ground with the switched-off engine and then at 3000 ft and 7000 ft. The temperature decreases with increasing altitude. Based on the time of arrival, the velocity increases with altitude. These results are consistent with the theory. At 80 kHz, only the A0 is visible, while at 180 kHz, both fundamental modes are present. ToF change with the temperature exhibits more significant shifts for A0 mode than S0 mode.

The data confirmed that the time difference between two signals at different altitudes increases gradually with the length of the signal, which indicates a temperature effect, not a damage effect. However, a more straightforward situation is for the 80 kHz signal, where only one mode is present.
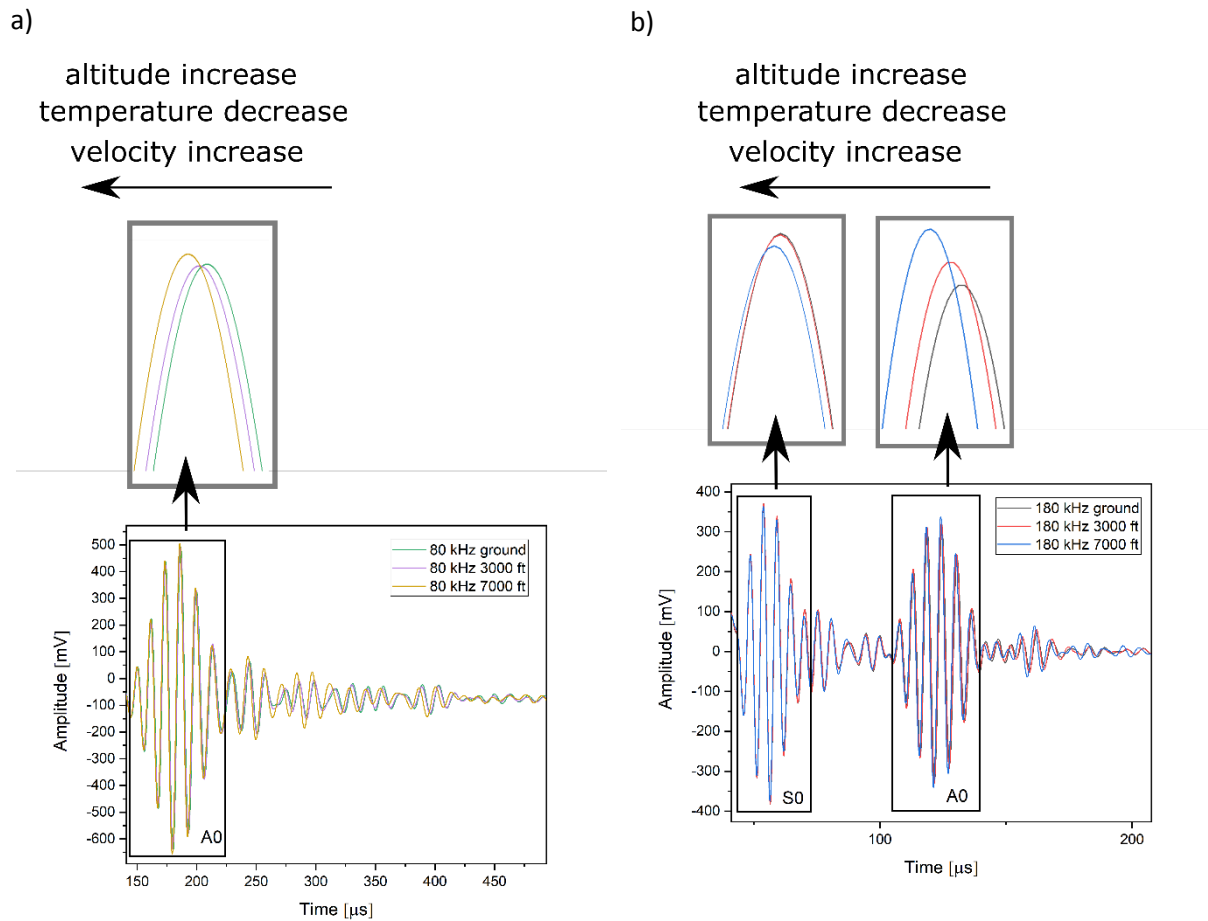
Figure 76 A Comparison of signals measured on the ground, in 3000 ft and 7000 ft for a) 80 kHz and b) 180 kHz

9.3   Conclusion

Environmental and operational effects on A0 and S0 mode propagation were analysed. Test results agreed with the theory. ToF decrease, hence the velocity increase with decreased temperature was documented within both experiments - the environmental chamber and the real flight tests. The signals were qualitatively evaluated. A comparison of the temperature and damage influence on the measured signal shows the clear distinction between those two situations. Impact damage detection using RAPID revealed that slight temperature variations (around 1-2 °C) do not significantly affect the resulting pseudo image, though the temperature variations caused some noise. ToF shifts determined at the maximum peak of a 50 kHz A mode were used as a damage-sensitive parameter. Since the time shifts were both positive and negative min-max normalization was used to process the data into the (0,1) range.

10 Summary

This thesis is focused on ultrasonic guided waves, specifically Lamb waves, as a structural health monitoring tool for aircraft structures. First, a theoretical base in the field of elastic waves in solids was presented, followed by their utilization in non-destructive testing. The next part of the thesis focused directly on Lamb waves. Fundamentals, basic features, and different propagation aspects in isotropic and anisotropic materials were outlined. Rayleigh-Lamb dispersion equation was derived since the equation was further used for calculations. Generation and detection using piezoelectric wafer active sensors were described, including the possibility of Lamb wave tuning.

Literature linked to damage detection approaches that correspond to those in the experimental part was investigated. Special attention was paid to dispersion curves determination since the phase velocity dispersion curve construction based on experimental data was proposed.

Experiments were performed on test specimens representing typical aircraft structures, and typical damages were introduced to those structures. DCB test was exploited as an accompanying experiment to investigate the thickness effect on Lamb wave time of flight. Then, impact damage detection was examined. Plates with constant thickness were used for experiments representing a simple structure, followed by plates with variable thickness, and finally, by skin-stringer joint representing a complex structure. ToF delays served as damage indices utilized by the RAPID algorithm to get the pseudo image of the damage. The algorithm was also successfully used for impact damage detection in a sandwich structure with measurements in slightly different temperatures. Another typical high-potential aircraft structure is an adhesively bonded joint, which may suffer from delamination or debonding. Therefore, a fatigue test was performed. Delamination and debonding propagation showed very complex behaviour in this structure. Analytical relations describing delamination length and time delay were established. RAPID algorithm was also used to visualize damage. In general, qualitative and quantitative analyses were performed to understand the Lamb wave propagation in those structures and evaluate the introduced damage. In general, ToF was exploited as a damage-sensitive parameter. Therefore, the effect of changing temperature was investigated within two supportive experiments. The difference between temperature-influenced signals within a wide range of temperatures and damage-influenced signals was outlined. Moreover, measurements in real operational conditions of an ultralight aircraft were obtained.

11 Discussion

The main pillars of the thesis stand in experimental investigation, specifically in:

- Methodology of phase velocity dispersion curve construction
- Damage detection in typical aerospace composite structures
- Thermal and operational conditions examination

The method of phase velocity determination has been proposed. Several velocity values using the only signal were obtained since the frequency spectra have a particular frequency bandwidth. Segments of the phase velocity dispersion curves were constructed, and experimental results were compared to calculations. This methodology was applied to both the isotropic and anisotropic materials. Segments of the phase velocity dispersion curves were compared to calculations using the Rayleigh-Lamb equation for the aluminium alloy sheet and the GUIGUW SW for the thermoplastic composite plate. Rayleigh–Lamb equation was solved numerically for the given frequencies. The proposed methodology was then successfully employed within other experiments described throughout the thesis. It can be concluded that the methodology has two conditions. Three transducers are needed - one actuator and two sensors placed at two close positions. In our experiments, sensors were mostly placed at a distance of up to 10 mm. The frequency spectra of those two signals are assumed not to be shifted. In case of a significant frequency shift, the methodology did not work.

A comprehensive Lamb-wave propagation analysis was performed on DCB specimens in two static configurations and during the DCB test. A suitable actuation frequency was found to be 40-50 kHz. The clear shape of the wave packet enabled easy time shift determination of the corresponding wave packet peak during the DCB test. Lamb wave velocity of the specific mode in the delaminated part and the full thickness part of the DCB specimen was key to determine. A simple equation was proposed to evaluate the relation of those two velocities, time delay and delamination length. The equation is theoretically valid for both the phase and group velocities. Which velocity is used corresponds to the determined time delay. However, evaluation was performed only for the phase velocity.

Impact damage is one of the most common types of damage in aircraft composite structures. Especially barely visible impact damages may cause serious consequences. Therefore, a significant part of the thesis was dedicated to this topic. Three kinds of structures made of thermoplastic composites were subjected to impact damages. The initial analyses were performed on simple plates with constant thickness using the SW Access (by Acellent), which is a black box. However, the SW process the same length of the time domain signals for all actuator-sensor paths, and with this approach, the pseudo image did not correctly visualize all impact damages. It was found that the signals from all the actuator-sensor paths need to be

processed. Therefore, the RAPID algorithm was used to visualize the damage through arbitrary DI. First, the correlation coefficient was exploited as a DI. The correlation was applied to extracted signals measured before and after the impact. The frequency of 80 kHz, where A0 mode was dominant, was chosen. However, all impacts were not correctly visualized either. Therefore, time delays of maximum peaks of the corresponding A0 modes were normalized and used as DI. All impacts were successfully localized using this approach. The same methodology was performed on plates with variable thickness. It was verified that Lamb waves adaptively propagate within the variable thickness sections. Time delays indicating impacts were several times smaller than for the constant thickness plate. However, the values were normalized, and all introduced impacts were correctly localized. Smaller time delays were probably caused by the material, which contained several glass layers. Apart from the A0 model, S0 mode at the frequency of 180 kHz was also successfully utilized. Nevertheless, the time delays of the S0 mode were about ten times smaller than in the case of the A0 mode. Therefore, the A0 mode was preferred.

Methodology for impact damage detection was intended to be applied to complex structures, such as skin-stringer joints. However, the structural complexity did not allow simple extraction of A0 mode as for the case of plates. A qualitative analysis using a number of sensors was performed because of the lack of equipment to obtain the full wavefield data. A partial conclusion was drawn on how the specific mode propagates through the joint. For the given transducer configuration, the A0 mode should be used for impact damage detection in the skin parts of the structure, while the S0 mode in the stringer part. Four out of six impacts were correctly localized. The area of the two unidentified impact damages was significantly smaller than the other four. The limitation probably lies in the minimum detectable impact area utilizing the given transducer configuration or propagation itself in such a complex structure.

Another investigated complex structure was an adhesively bonded composite joint subjected to the fatigue test. Delamination and debonding propagated from the centre of the bonded section to both sides. The similarity with the DCB test was assumed. As DCB specimen was delaminated, the wave adapted with decreased velocity to the half-thickness (delaminated) part. As the bonded part of the joint debonded/delaminated, the wave splits into both delaminated/debonded sections with decreased velocity. Assumed time delays were measured in the case of A0 mode and time advances in the case of S0 mode. However, S0 time shifts were negligible compared to A0 mode time shifts. Time delays were related to the delamination lengths determined by the UT A-scan. The slope of the linear relationship was linked to the adherend in which the delamination/debonding occurred. Those findings were verified by metallographic analysis. Moreover, RAPID algorithm was successfully utilized to assess the presence of the damage. The bonded joint was divided into three subsections, and the results were combined into one image. The methodology was identical to the one used for

impact damage detection in plates. A0 model at the frequency of 70 kHz was extracted, and time delay was used as a damage-sensitive parameter. The equation used for delamination length calculation in DCB specimen did show significant errors, probably because of incorrect velocity values. The velocities were determined for the case of pure debonding in the adhesive. In fact, damage propagated partly in adhesive and partly in the first or the second adherend. Delamination "jumped" by the transply cracking into another lamina. Therefore, the velocity could not be determined unambiguously.

In conclusion, ToF shift is a common damage-sensitive parameter utilized within all conducted experiments. Either as an input parameter to calculate DI or a direct parameter related to damage extent. Most experiments utilized ToF delay of more damage-sensitive A0 mode. In all cases, extraction of the specific, identified wave packet was essential. Velocity determination and signals obtained using sensors placed identically on both surfaces contributed to the mode identification.

Additional experiments to evaluate temperature and operational effects were conducted. Laboratory controlled tests in a climatic chamber within a wide range of temperatures showed apparent velocity increase with decreased temperature. However, the signals showed a significant frequency shift. Therefore, the methodology of the phase velocity dispersion curves determination has not been utilized. Only ToF of the corresponding peaks were related to the temperature. The structure was also subjected to impact damages. Time delay variations were caused not only by damage itself but also by small temperature variations. In this case, RAPID algorithm successfully imaged the impacts. Several flight tests were conducted to evaluate operational conditions such as temperature, vibrations, and other unknown effects. Sensors were mounted on a fuselage skin, and measurements at different altitudes; hence temperatures were performed. It was found that the used equipment is immune to the noisy environment. Signals were clear, ready to be post-processed. It was possible to distinguish signals influenced by the temperature from those influenced by damage. These partial conclusions lead to the area of future work concerning temperature compensation and conducting impact damages within a wider range of temperatures.

All experiments were performed with the Acellent ScanGenie II. This device proved to be effective in operational conditions. One reason is probably low pass filtering, which on the other hand, enables non-linear measurements. Incorporated SW for damage detection did not prove any significant results and therefore was not utilized. Exported signals were analysed in the SW Origin Pro. PZT SmartLayer single sensors or Steminc disc transducers were utilized, and both showed similar responses.

12 Conclusion

The thesis deals with practical applications of ultrasonic guided waves for damage detection in typical aerospace composite structures. Based on the literature review, four objectives have been stated to cover the current needs within the structural testing. In this chapter, brief conclusions are stated for each goal.

1. **Propose a fast method for dispersion curves construction based on experimental data**

Determination of the phase velocity based on the experimental data was proposed. A segment of a dispersion curve for the desired frequency range can be constructed fast using only three transducers (one actuator and two sensors). Frequency filtering of broadband signals enabled phase velocity calculation using the time lag and distance of the two close sensors. Therefore, as a great advantage, one broadband wave packet provided multiple velocity values. Even distorted signals may be successfully exploited using a part of the wave packet for evaluation. The methodology was verified for both isotropic and anisotropic structures and was limited only to the frequency-shifted signals.

2. **Improve existing impact damage detection algorithm**

Damage detection and localization of various composite aircraft structures were evaluated using the RAPID. It was found that commonly used methods utilizing, e.g., correlation coefficient, do not work uniformly for all the cases. Therefore, the substantial analysis revealed that the ToF delay parameter of the A0 mode at lower frequencies is highly sensitive to impact damage rather than the S0 mode. Utilizing ToF delay of the extracted A0 modes as a damage-sensitive parameter within RAPID improved the capability of impact damage localization. Moreover, delamination/debonding propagation in the adhesively bonded joint was successfully imaged within the fatigue test.

3. **Improve diagnostic capabilities for delamination detection by exploiting velocity-thickness relation**

In specific cases, delamination propagates in the midplane of the structure. For such cases as, e.g., DCB specimen, a simple equation was derived to calculate the precise delamination length. The relation exploited measured time delay and velocities for the full and half-thickness of the structure. The corresponding velocities were utilized based on the extracted time lag (phase or group time delay). The limitation of this equation was the thickness uniformity requirement.

4. **Evaluate the performance of the method under the environmental and operational conditions**

Several types of damages were successfully assessed using the UGW method. However, all of them were evaluated in similar conditions. Therefore, thermal dependency and operational conditions were also examined.

Unique data were obtained under environmental and operational conditions. First, CFRP sandwich structure was exposed to the temperature range of -50 to +50 °C, and the dependency of ToF and temperature was determined. Temperature variations during the following impact damage measurements were identified. Therefore, time shifts were normalized using min-max normalization to be used in the RAPID.

Several real flight tests using UL aircraft Eurostar EV 97 have been conducted to understand how signals are influenced by real operational conditions, especially vibrations and temperature (altitude). All signals were clear and ready to be post-processed. Altitude effects were in agreement with theory and results obtained in a climatic chamber.

It has been shown that temperature-influenced and damage-influenced signals may be easily distinguished. Future work regarding conditions when temperature compensation needs to be involved will be focused. Either for simple relations between the time shift and damage extent or utilizing the RAPID. Based on the results, the simple relationship between the time shift and the damage extent shall be compensated for any temperature variations. On the other hand, the RAPID algorithm worked for small temperature variations without any special compensation.

List of figures

List of tables

References

[1]   C. Boller, "Why SHM? A Motivation," NATO Lecture Series STO-MP-AVT-220, Structural Health Monitoring of Military Vehicles: STO Educational Notes; NATO STO: Brussels, Belgium, 2014.

[2]   V. Giurgiutiu, "Introduction," Structural Health Monitoring with Piezoelectric Wafer Active Sensors, pp. 1–19, 2014.

[3]   V. Giurgiutiu, "Introduction," Structural Health Monitoring of Aerospace Composites, pp. 1–23, 2016.

[4]   E. Lindgren, "USAF Research laboratory perspective on structural health monitoring in support of risk management," AFRL-RX-WP-JA-2018-0317, 2018, [Online]. Available: https://apps.dtic.mil/sti/pdfs/AD1065027.pdf (accessed March 15, 2022).

[5]   J. Rouchon, "Fatigue and damage tolerance evaluation of structures: the composite materials response," 22nd Plantema Memorial Lecture, 2009, [Online]. Available: https://core.ac.uk/download/pdf/53034052.pdf (accessed March 15, 2022).

[6]   E. Greenhalgh, Ed., "Failure Analysis and Fractography of Polymer Composites," Oct. 2009.

[7]   S. O. Neidigk, D. P. Roach, R. L. Duvall, T. M. Rice, "Detection and Characterization of Hail Impact Damage in Carbon Fiber Aircraft Structures," FAA Airworthiness Assurance Center, Albuquerque, NM, USA, Tech. Rep. DOT/FAA/TC-16/8, 2017.

[8]   H. Ren, X. Chen, and Y. Chen, "Structural Health Monitoring and Influence on Current Maintenance," Reliability Based Aircraft Maintenance Optimization and Applications, pp. 173–184, 2017.

[9]   B.Y. Kolesnikov and L. Herbeck, "Carbon Fiber Composite Airplane Fuselage: Concept and Analysis," ILA International Conference, Berlin, p. 2, 2004.

[10]   D. D. Kreculj and B. P. Rašuo, "Impact damages modeling in laminated composite structures," Tehnika, vol. 69, no. 6, pp. 969–976, 2014.

[11]   A. J. Fawcett and G. D. Oakes, "Boeing composite airframe damage tolerance and service experience," Proceedings of the FAA workshop for composite damage tolerance andmaintenance. Chicago, IL: National Institute for Aviation Research, 2006, pp.1–32.

[12]   S. Gordon, R. Boukhili, and N. Merah, "Impact behavior and finite element prediction of the compression after impact strength of foam/vinylester-glass composite sandwiches," Journal of Sandwich Structures & Materials, vol. 16, no. 5, pp. 551–574, Jul. 2014.

[13] A. Marques, A. Mocanu, N. Tomić, S. Balos, E. Stammen, A. Lundevall, S. Abrahami, R. Günther, J. de Kok, and S. Teixeira de Freitas, "Review on Adhesives and Surface Treatments for Structural Applications: Recent Developments on Sustainability and Implementation for Metal and Composite Substrates," Materials, vol. 13, no. 24, p. 5590, Dec. 2020.

[14] Safibra, "FBG monitoring systems," [Online]. Available: http://www.safibra.cz/en/fbg-sensors-and-units (accessed Aug. 22, 2018).

[15] M. Růžička, M. Dvořák, N. Schmidová, L. Šašek, and M. Štěpánek, "Health and usage monitoring system for the small aircraft composite structure," ISCPMS 2016, Proceedings of the 2nd International Symposium on Current Progress in Mathematics and Sciences, Jul. 2017.

[16] S. Gopalakrishnan, M. Ruzzene, and S. Hanagud, "Computational Techniques for Structural Health Monitoring," Springer Series in Reliability Engineering, 2011.

[17] J. L. Rose, "Introduction," Ultrasonic Guided Waves in Solid Media, pp. 1–15, 2014.

[18] S. W. Doebling, C. R. Farrar, M. B. Prime, and D. W. Shevitz, "Damage identification and health monitoring of structural and mechanical systems from changes in their vibration characteristics: A literature review," May 1996.

[19] R. Lammering, S. Duczek, and U. Gabbert, "Motivation," Research Topics in Aerospace, pp. 3–9, Aug. 2017.

[20] S. Abbas, F. Li, and J. Qiu, "A Review on SHM Techniques and Current Challenges for Characteristic Investigation of Damage in Composite Material Components of Aviation Industry," Materials Performance and Characterization, vol. 7, no. 1, p. 20170167, Jun. 2018.

[21] R. Ruzek, P. Kudrna, M. Kadlec, V. Karachalios, and K. I. Tserpes, "Strain and damage monitoring in CFRP fuselage panels using fiber Bragg grating sensors. Part II: Mechanical testing and validation," Composite Structures, vol. 107, pp. 737–744, Jan. 2014.

[22] N. Hirano, H. Mamizu, A. Kuraishi, T. Itoh, N. Takeda and K. Enomoto, "Detectability Assessment of Optical Fiber Sensor Based Impact Damage Detection for Composite Airframe Structures, " EWSHM - 7th European Workshop on Structural Health Monitoring, La Cité, Nantes, Jul 2014, pp. 41-48.

[23] P. Shrestha, J.-H. Kim, Y. Park, and C.-G. Kim, "Impact localization on composite structure using FBG sensors and novel impact localization technique based on error outliers," Composite Structures, vol. 142, pp. 263–271, May 2016.

[24] A. Lamberti, G. Luyckx, W. Van Paepegem, A. Rezayat, and S. Vanlanduit, "Detection, Localization and Quantification of Impact Events on a Stiffened Composite Panel with

Embedded Fiber Bragg Grating Sensor Networks," Sensors, vol. 17, no. 4, p. 743, Apr. 2017.

[25] M. Kreuzer, "Strain measurement with fiber Bragg grating sensors," HBM, 2006, [Online]. Available:http://micronoptics.ru/uploads/library/documents/FBGS_StrainMeasurement_mo.pdf (accessed Nov 6, 2018).

[26] M. Wishaw, D. P. Barton, "Comparative Vacuum Monitoring: A New Method of In-Sity Real Time Crack Detection and Monitoring," [Online]. Available: https://www.ndt.net/apcndt2001/papers/1129/1129.htm (accessed Nov 6, 2018).

[27] M. Příbán, "Metoda akustické emise 1, Obecná část – základní principy," Česká společnost pro NDT, Brno, 2014.

[28] Z. Převorovský, "SHM konstrukcí z kompozitů s využitím akustické emise (AE) a nelineární ultrazvukové spektroskopie (NEWS)," [Online]. Available: http://www.csm-kompozity.wz.cz/Prevorovsky.pdf (accessed Nov 6, 2018).

[29] C. P. Fritzen, "Vibration-Based Structural Health Monitoring – Concepts and Applications," Key Engineering Materials, vol. 293–294, pp. 3–20, Sep. 2005.

[30] Standard Practice for Guided Wave Testing of Above Ground Steel Pipework Using Piezoelectric Effect Transduction, ASTM E2775-16, 2016.

[31] P. Hora and O. Červená, "Determination of Lamb wave dispersion curves by means of Fourier transform," Applied and Computational Mechanics, vol. 6, no. 1, 2012.

[32] M. Šofer, P. Ferfecki, and P. Šofer, "Numerical solution of Rayleigh-Lamb frequency equation for real, imaginary and complex wavenumbers," MATEC Web of Conferences, vol. 157, p. 08011, 2018.

[33] P. Šofer, M. Šofer, M. Raček, D. Cekus, and P. Kwiatoń, "Partial Energy Transfer Model of Lamb Waves Scattering in Materially Isotropic Waveguides," Applied Sciences, vol. 11, no. 10, p. 4508, May 2021.

[34] R. Hedl, J. Finda, and G. Parthasarathy, "Optimization of PZT actuator/sensor array for monitoring of aircraft fuselage panel using ultrasonic Lamb waves," Proc. NDE for Safety / Defektoskopie, 2010.

[35] Structural damage index mapping system and method by Hedl, R. and Finda, J. and Adamek, (2012), U.S. Patent 8831895 [Online]. Available: https://patents.justia.com/patent/8831895 (accessed March 15, 2022).

[36] B. A. Auld and R. E. Green, "Acoustic Fields and Waves in Solids: Two Volumes," Physics Today, vol. 27, no. 10, pp. 63–64, Oct. 1974.

[37] J. D. Achenbach, "Withdrawn: Introduction," Wave Propagation in Elastic Solids, pp. 1–9, 1975.

[38] L. W. Schmerr Jr.1, S.-J. Song, Ultrasonic Nondestructive Evaluation Systems Models and Measurements, Springer, 2007.

[39] O. Novotný, "Seismic surface waves: Lecture notes for post-graduate studies," Salvador, Bahia: Instituto de Fisica Instituto de Geociencias, 1999.

[40] R. P. Feynman, R. B. Leighton, M. Sands, "Feynmanovy přednášky z fyziky: revidované vydání s řešenými příklady," 2. vydání. Praha: Fragment, 2013. ISBN 978-80-253-1642-9.

[41] D. W. Steeples, "Shallow Seismic Methods," Hydrogeophysics, pp. 215–251.

[42] V. Giurgiutiu, "Guided Waves," Structural Health Monitoring with Piezoelectric Wafer Active Sensors, pp. 293–355, 2014.

[43] N. Rauter, B. Hennings, M. N. Neumann, A. Asmus, and R. Lammering, "Wave Propagation in Elastic Solids: An Analytical Approach," Research Topics in Aerospace, pp. 17–62, Aug. 2017.

[44] X. Yu, P. Manogharan, Z. Fan, and P. Rajagopal, "Feature-guided waves (FGW) in plate structures with 90° transverse bends," AIP Conference proceedings, Aug. 2015.

[45] D. Fan and M. Lowe, "Investigation on Feature Guided Waves," [Online]. https://www.imperial.ac.uk/media/imperial-college/research-centres-and-groups/non-destructive-evaluation/public/ZF-feature-guided-wave_Feb2010.pdf (accessed Nov. 9, 2021).

[46] R. Regazzo a M. Regazzová, "Ultrazvuk - základy ultrazvukové defektoskopie," Praha: BEN, 2013. ISBN 978-80-73000-4666-8.

[47] P. Žbánek, J. Blahušek, J. Matoušek, T. Zavadil, "Ultrazvuková metoda – stupeň I, II", Praha, ATG, 2017.

[48] A. Hecht, "Time of Flight Diffraction Technique (TOFD) - An Ultrasonic Testing Method for all Applications?", Sept. 1997. [Online]. Available: https://www.ndt.net/article/tofd/hecht/hecht.htm (accessed Jan. 13, 2022).

[49] Ch. U. Grosse, H. W. Reinhardt, "The resonance method – Application of a new nondestructive technique which enables thickness measurements at remote concrete parts," 1996, [Online]. Available: https://www.ndt.net/article/grosse2/grosse2.htm (accessed Jan. 13, 2022).

[50] P. Bělský and M. Kadlec, "Non-destructive Methods for Damage Assessment of Composite Sandwich Structures," MATEC Web of Conferences, vol. 188, p. 01008, 2018.

[51] M. A. H. Hishamuddin, S. M. Mohd Zin, and E. M. Yusup, "Non-Destructive Measurement and Evaluation of Surface Cracks Using Ultrasonic Rayleigh Waves – A Review," Journal of Physics: Conference Series, vol. 2129, no. 1, p. 012038, Dec. 2021.

[52]   V. Samaitis, E. Jasiūnienė, P. Packo, and D. Smagulova, "Ultrasonic Methods," Springer Aerospace Technology, pp. 87–131, 2021.

[53]   Olympus. "Multi-mode Adhesive Bond Testing", [Online]. Available: https://www.olympus-ims.com/cs/resources/white-papers/multi-mode-adhesive-bond-testing/ (accessed Aug. 20, 2018).

[54]   G. Hübschen, "Ultrasonic techniques for materials characterization," Materials Characterization Using Nondestructive Evaluation (NDE) Methods, pp. 177–224, 2016.

[55]   Dharmendra and S. Pandey, "Ultrasonics: A Technique of Material Characterization," Acoustic Waves, Sep. 2010.

[56]   B. J. Tucker, D. A. Bender, D. G. Pollock and M. P. Wolcott, "Ultrasonic Plate Wave Evaluation of Natural Fiber Composite Panels, " Wood and fiber science: journal of the Society of Wood Science and Technology, vol. 35, no. 2, pp. 266-281, Apr. 2003.

[57]   M. J. S. Lowe, "Wave propagation| Guided Waves in Structures," Encyclopedia of Vibration, pp. 1551–1559, 2001.

[58]   Rose, J.L., Waves in Plates. Ultrasonic Guided Waves in Solid Media, pp. 77–106, 2014.

[59]   Z. Ma and L. Yu, "Lamb wave defect detection and evaluation using a fully non-contact laser system," Health Monitoring of Structural and Biological Systems XIII, Apr. 2019.

[60]   N. Hosoya, A. Yoshinaga, A. Kanda, and I. Kajiwara, "Non-contact and non-destructive Lamb wave generation using laser-induced plasma shock wave," International Journal of Mechanical Sciences, vol. 140, pp. 486–492, May 2018.

[61]   J.-C. Krapez, F. Taillade, T. Lamarque, and D. Balageas, "Shearography: A Tool for Imaging Lamb Waves in Composites and their Interaction with Delaminations," Review of Progress in Quantitative Nondestructive Evaluation, pp. 905–912, 1999.

[62]   J. L. Rose, "The Semi-Analytical Finite Element Method," Ultrasonic Guided Waves in Solid Media, pp. 135–154, 2014.

[63]   D. Schmidt, M. Sinapius "Mode Selective Actuator – Sensor - Systems," Research Topics in Aerospace, pp. 401–430, Aug. 2017.

[64]   Giurgiutiu, "Piezoelectric Wafer Active Sensors – PWAS Transducers," Structural Health Monitoring with Piezoelectric Wafer Active Sensors, 2014.

[65]   G. B. Santoni, L. Yu, B. Xu, and V. Giurgiutiu, "Lamb Wave-Mode Tuning of Piezoelectric Wafer Active Sensors for Structural Health Monitoring," Journal of Vibration and Acoustics, vol. 129, no. 6, pp. 752–762, Feb. 2007.

[66]   V. Giurgiutiu, "Tuned Lamb Wave Excitation and Detection with Piezoelectric Wafer Active Sensors for Structural Health Monitoring," Journal of Intelligent Material Systems and Structures, vol. 16, no. 4, pp. 291–305, Apr. 2005.

[67] I. Mueller and C.-P. Fritzen, "Failure Assessment of Piezoelectric Actuators and Sensors for Increased Reliability of SHM Systems," Structural Health Monitoring from Sensing to Processing, Sep. 2018.

[68] J. L. Rose, "Dispersion Principles," Ultrasonic Guided Waves in Solid Media, pp. 16–35, 2014.

[69] F. Raddatz and M. Sinapius, "Time-of-Flight Calculation in Complex Structures," Research Topics in Aerospace, pp. 331–357, Aug. 2017.

[70] S. Pant, J. Laliberte, M. Martinez, and B. Rocha, "Derivation and experimental validation of Lamb wave equations for an n-layered anisotropic composite laminate," Composite Structures, vol. 111, pp. 566–579, May 2014.

[71] C. Willberg, G. Mook, U. Gabbert, and J. Pohl, "The Phenomenon of Continuous Mode Conversion of Lamb Waves in CFRP Plates," Key Engineering Materials, vol. 518, pp. 364–374, Jul. 2012.

[72] R. Gorgin, Y. Luo, and Z. Wu, "Environmental and operational conditions effects on Lamb wave based structural health monitoring systems: A review," Ultrasonics, vol. 105, p. 106114, Jul. 2020.

[73] F. Lanza di Scalea and S. Salamone, "Temperature effects in ultrasonic Lamb wave structural health monitoring systems," The Journal of the Acoustical Society of America, vol. 124, no. 1, pp. 161–174, Jul. 2008.

[74] M. Scheerer and D. Lager, "D.Validation of Temperature Compensation Techniques for Impact Damage Detection and Localization Using Ultrasonic Sparse Arrays, " EWSHM - 7th European Workshop on Structural Health Monitoring, La Cité, Nantes, Jul 2014, pp. 387-394.

[75] J. Moll, C. Kexel, S. Pötzsch, M. Rennoch, and A. S. Herrmann, "Temperature affected guided wave propagation in a composite plate complementing the Open Guided Waves Platform," Scientific Data, vol. 6, no. 1, Oct. 2019.

[76] Boon, M.J.G.N., Zarouchas, D., Martinez, M., Gagar, D., Rinze, B., Foote, P., "Temperature and load effects on acoustic emission signals for structural health monitoring applications, " EWSHM - 7th European Workshop on Structural Health Monitoring, La Cité, Nantes, Jul 2014, pp. 41-48.

[77] S. Abbas, F. Li, Y. Zhu, and X. Tu, "Experimental investigation of impact of environmental temperature and optimal baseline for thermal attenuation in structural health monitoring based on ultrasonic guided waves," Wave Motion, vol. 93, p. 102474, Mar. 2020.

[78] M. Salmanpour, Z. Sharif Khodaei, and M. Aliabadi, "Guided wave temperature correction methods in structural health monitoring," Journal of Intelligent Material Systems and Structures, vol. 28, no. 5, pp. 604–618, Jul. 2016.

[79] A. J. Croxford, J. Moll, P. D. Wilcox, and J. E. Michaels, "Efficient temperature compensation strategies for guided wave structural health monitoring," Ultrasonics, vol. 50, no. 4–5, pp. 517–528, Apr. 2010.

[80] Y. Lu and J. E. Michaels, "A methodology for structural health monitoring with diffuse ultrasonic waves in the presence of temperature variations," Ultrasonics, vol. 43, no. 9, pp. 717–731, Oct. 2005.

[81] J. L. Rose, "Introduction to Guided Wave Nonlinear Methods," Ultrasonic Guided Waves in Solid Media, pp. 378–401, 2014.

[82] M. F. Müller, J.-Y. Kim, J. Qu, and L. J. Jacobs, "Characteristics of second harmonic generation of Lamb waves in nonlinear elastic plates," The Journal of the Acoustical Society of America, vol. 127, no. 4, pp. 2141–2152, Apr. 2010.

[83] C. Bermes, J.-Y. Kim, J. Qu, and L. J. Jacobs, "Nonlinear Lamb waves for the detection of material nonlinearity," Mechanical Systems and Signal Processing, vol. 22, no. 3, pp. 638–646, Apr. 2008.

[84] V. K. Chillara and C. J. Lissenden, "Review of nonlinear ultrasonic guided wave nondestructive evaluation: theory, numerics, and experiments," Optical Engineering, vol. 55, no. 1, p. 011002, Aug. 2015

[85] K. Wang, M. Liu, Z. Su, S. Yuan, and Z. Fan, "Analytical insight into 'breathing' crack-induced acoustic nonlinearity with an application to quantitative evaluation of contact cracks," Ultrasonics, vol. 88, pp. 157–167, Aug. 2018.

[86] Y. Yang, C.-T. Ng, A. Kotousov, H. Sohn, and H. J. Lim, "Second harmonic generation at fatigue cracks by low-frequency Lamb waves: Experimental and numerical studies," Mechanical Systems and Signal Processing, vol. 99, pp. 760–773, Jan. 2018.

[87] R. Wang, Q. Wu, F. Yu, Y. Okabe, and K. Xiong, "Nonlinear ultrasonic detection for evaluating fatigue crack in metal plate," Structural Health Monitoring, vol. 18, no. 3, pp. 869–881, Jul. 2018.

[88] N. P. Yelve, M. Mitra, P. M. Mujumdar, and C. Ramadas, "A hybrid method based upon nonlinear Lamb wave response for locating a delamination in composite laminates," Ultrasonics, vol. 70, pp. 12–17, Aug. 2016.

[89] R. Soleimanpour and C.-T. Ng, "Scattering analysis of nonlinear Lamb waves at delaminations in composite laminates," Journal of Vibration and Control, p. 107754632199014, Feb. 2021.

[90] J. L. Rose, "Guided Waves in Layered Structures," Ultrasonic Guided Waves in Solid Media, pp. 209–244, 2014.

[91] P. Bocchini, A. Marzani, and E. Viola, "Graphical User Interface for Guided Acoustic Waves," Journal of Computing in Civil Engineering, vol. 25, no. 3, pp. 202–210, May 2011.

[92] L. Wang and F. Yuan, "Group velocity and characteristic wave curves of Lamb waves in composites: Modeling and experiments," Composites Science and Technology, vol. 67, no. 7–8, pp. 1370–1384, Jun. 2007.

[93] D. Waltisberg and R. Raišutis, "Group velocity estimation of Lamb waves based on the wavelet transform", Ultragarsas (Ultrasound), vol. 63, no. 4, pp. 35–40, 2008

[94] Z. Lašová and R. Zemčík, "Determination of group velocity of propagation of Lamb waves in aluminium plate using piezoelectric transducers," Applied and Computational Mechanics, vol. 11, no. 1, 2017.

[95] B. Hernandez Crespo, C. Courtney, and B. Engineer, "Calculation of Guided Wave Dispersion Characteristics Using a Three-Transducer Measurement System," Applied Sciences, vol. 8, no. 8, p. 1253, Jul. 2018.

[96] L. Zeng, L. Huang, X. Cao, and F. Gao, "Determination of Lamb wave phase velocity dispersion using time–frequency analysis," Smart Materials and Structures, vol. 28, no. 11, p. 115029, Oct. 2019.

[97] L. Draudvilienė and L. Mažeika, "Investigation of the spectrum decomposition technique for estimation of the group velocity Lamb waves," Ultrasound, vol. 66, no. 3, Oct. 2011.

[98] L. Draudvilienė and L. Mažeika, "Measurement of the group velocity of Lamb waves in aluminium plate using spectrum decomposition technique," Ultrasound, vol. 66, no. 4, Jan. 2012.

[99] L. Draudviliene, H. Ait Aider, O. Tumsys, and L. Mazeika, "The Lamb waves phase velocity dispersion evaluation using a hybrid measurement technique," Composite Structures, vol. 184, pp. 1156–1164, Jan. 2018.

[100] M. Salas, O. Focke, A. S. Herrmann, and W. Lang, "Wireless actuation of piezo-elements for the structural health monitoring of carbon-fiber-reinforced-polymers," Mechatronics, vol. 34, pp. 128–136, Mar. 2016.

[101] C. Dürager, A. Heinzelmann, and D. Riederer, "A wireless sensor system for structural health monitoring with guided ultrasonic waves and piezoelectric transducers," Structure and Infrastructure Engineering, vol. 9, no. 11, pp. 1177–1186, Nov. 2013.

[102] S. Pant, Lamb Wave Propagation and Material Characterization of Metallic and Composite Aerospace Structures for Improved Structural Health Monitoring (SHM), Ph.D. dissertation, Dep. Aerosp. Eng., Carleton Univ., Ottawa, Ontario, Canada, 2014.

[103] C. Tao, H. Ji, J. Qiu, C. Zhang, Z. Wang, and W. Yao, "Characterization of fatigue damages in composite laminates using Lamb wave velocity and prediction of residual life," Composite Structures, vol. 166, pp. 219–228, Apr. 2017.

[104] M. D. Seale, B. T. Smith, and W. H. Prosser, "Lamb wave assessment of fatigue and thermal damage in composites," The Journal of the Acoustical Society of America, vol. 103, no. 5, pp. 2416–2424, May 1998.

[105] M. Bonet, B. Eckstein, R. Loendersloot, and P. Wierach, "Identification of Barely Visible Impact Damages on a Stiffened Composite Panel with a Probability-based Approach," Structural Health Monitoring 2015, 2015.

[106] L. Huang, L. Zeng, J. Lin, and Z. Luo, "An improved time reversal method for diagnostics of composite plates using Lamb waves," Composite Structures, vol. 190, pp. 10–19, Apr. 2018.

[107] H. W. Park, S. B. Kim, and H. Sohn, "Understanding a time reversal process in Lamb wave propagation," Wave Motion, vol. 46, no. 7, pp. 451–467, Nov. 2009.

[108] J. K. Agrahari and S. Kapuria, "Effects of adhesive, host plate, transducer and excitation parameters on time reversibility of ultrasonic Lamb waves," Ultrasonics, vol. 70, pp. 147–157, Aug. 2016.

[109] Z. Su, L. Ye, and Y. Lu, "Guided Lamb waves for identification of damage in composite structures: A review," Journal of Sound and Vibration, vol. 295, no. 3–5, pp. 753–780, Aug. 2006.

[110] P. Kudela, M. Radzienski, and W. Ostachowicz, "Impact induced damage assessment by means of Lamb wave image processing," Mechanical Systems and Signal Processing, vol. 102, pp. 23–36, Mar. 2018.

[111] J. L. Rose, "Guided Wave Imaging Methods," Ultrasonic Guided Waves in Solid Media, pp. 402–420, 2014.

[112] J. E. Michaels and T. E. Michaels, "Guided wave signal processing and image fusion for in situ damage localization in plates," Wave Motion, vol. 44, no. 6, pp. 482–492, Jun. 2007.

[113] X. Zhao, H. Gao, G. Zhang, B. Ayhan, F. Yan, C. Kwan, and J. L. Rose, "Active health monitoring of an aircraft wing with embedded piezoelectric sensor/actuator network: I. Defect detection, localization and growth monitoring," Smart Materials and Structures, vol. 16, no. 4, pp. 1208–1217, Jun. 2007.

[114] D. Wang, L. Ye, Y. Lu, and Z. Su, "Probability of the presence of damage estimated from an active sensor network in a composite panel of multiple stiffeners," Composites Science and Technology, vol. 69, no. 13, pp. 2054–2063, Oct. 2009.

[115] Wu, K. Liu, Y. Wang, and Y. Zheng, "Validation and evaluation of damage identification using probability-based diagnostic imaging on a stiffened composite panel," Journal of Intelligent Material Systems and Structures, vol. 26, no. 16, pp. 2181–2195, Sep. 2014.

[116] J. Hettler, M. Tabatabateipour, S. Delrue, and K. Van Den Abeele, "Application of a Probabilistic Algorithm for Ultrasonic Guided Wave Imaging of Carbon Composites," Physics Procedia, vol. 70, pp. 664–667, 2015.

[117] S. Mustapha, L. Ye, X. Dong, and M. M. Alamdari, "Evaluation of barely visible indentation damage (BVID) in CF/EP sandwich composites using guided wave signals," Mechanical Systems and Signal Processing, vol. 7677, pp. 497–517, Aug. 2016.

[118] M. H. Sherafat, R. Guitel, N. Quaegebeur, P. Hubert, L. Lessard, and P. Masson, "Structural health monitoring of a composite skin-stringer assembly using within-the-bond strategy of guided wave propagation," Materials & Design, vol. 90, pp. 787–794, Jan. 2016.

[119] M. H. Sherafat, R. Guitel, N. Quaegebeur, L. Lessard, P. Hubert, and P. Masson, "Guided wave scattering behavior in composite bonded assemblies," Composite Structures, vol. 136, pp. 696–705, Feb. 2016.

[120] P. T. Birgani, K. N. Tahan, S. Sodagar, and M. Shishesaz, "Theoretical modeling of low-attenuation lamb wave modes generation in three-layer adhesive joints using angle beam transducer," Latin American Journal of Solids and Structures, vol. 12, no. 3, pp. 461–476, Mar. 2015.

[121] K. Heller, L. Jacobs, and J. Qu, "Characterization of adhesive bond properties using Lamb waves," NDT & E International, vol. 33, no. 8, pp. 555–563, Dec. 2000.

[122] R. Seifried, L. J. Jacobs, and J. Qu, "Propagation of guided waves in adhesive bonded components," NDT & E International, vol. 35, no. 5, pp. 317–328, Jul. 2002.

[123] P. K. Puthillath, F. Yan, C. J. Lissenden, J. L. Rose, D. O. Thompson, and D. E. Chimenti, "Ultrasonic guided waves for the inspection of adhesively bonded joints," 34th Annual Review of Progress in Quantitative Nondestructive Evaluation, AIP Conference Proceedings, 2008.

[124] H. Matt, I. Bartoli, and F. Lanza di Scalea, "Ultrasonic guided wave monitoring of composite wing skin-to-spar bonded joints in aerospace structures," The Journal of the Acoustical Society of America, vol. 118, no. 4, pp. 2240–2252, Oct. 2005.

[125] E. Siryabe, M. Renier, A. Meziane, and M. Castaings, "The Transmission of Lamb Waves Across Adhesively Bonded lap Joints to Evaluate Interfacial Adhesive Properties," Physics Procedia, vol. 70, pp. 541–544, 2015.

[126] B. Ren and C. J. Lissenden, "Ultrasonic guided wave inspection of adhesive bonds between composite laminates," International Journal of Adhesion and Adhesives, vol. 45, pp. 59–68, Sep. 2013.

[127] D. Wang, L. Ye, Y. Tang, and Y. Lu, "Monitoring of delamination onset and growth during Mode I and Mode II interlaminar fracture tests using guided waves," Composites Science and Technology, vol. 72, no. 2, pp. 145–151, Jan. 2012.

[128] O. Y. Karpenko, M. Haq, A. Khomenko, L. Udpa, and S. Udpa, "Lamb Wave Based Monitoring of Delamination Growth in Mode I and Mode II Fracture Tests," Conference Proceedings of the Society for Experimental Mechanics Series, pp. 33–43, Jul. 2013.

[129] C. Ramadas, A. Hood, K. Balasubramaniam, and M. Joshi, "Ultrasonic Lamb Wave Based Crack Growth Prediction for Estimation of Strain Energy Release Rate," Advanced Materials Research, vol. 585, pp. 24–28, Nov. 2012.

[130] B. Li, L. Ye, Z. Li, Z. Ma, and H. Kalhori, "Quantitative identification of delamination at different interfaces using guided wave signals in composite laminates," Journal of Reinforced Plastics and Composites, vol. 34, no. 18, pp. 1506–1525, Jul. 2015.

[131] Standard test method for mode I interlaminar fracture toughness of unidirectional fiber-reinforced polymer matrix composites, ASTM D5528-13, 2013.

[132] Airbus Material Specification / Carbon Fiber Reinforced Thermoplastic Materials, AIMS 05-09-002, 1998.

[133] P. Homola, M. Kadlec, R. Růžek, and J. Šedek, "Fatigue behaviour of tailored blank thermoplastic composites with internal ply-drops," Procedia Structural Integrity, vol. 5, pp. 1342–1348, 2017.

References of author´s publications

[a] J. Cagáň and L. Michalcová, "Impact Damage Detection in CFRP Composite via Electrical Resistance Tomography by Means of Statistical Processing," Journal of Nondestructive Evaluation, vol. 39, no. 2, Apr. 2020.

[b] L. Michalcová, "Delamination growth analysis in mode I by means of Lamb waves," Materials Today: Proceedings, vol. 5, no. 13, pp. 26470–26475, 2018.

[c] L. Šedková, J. Šedek, "Defect detectability in composite plates with variable thickness using Lamb waves", the 58th International Scientific Conference Experimental Stress Analysis (EAN), 2020.

[d] L. Šedková, V. Vlk, and J. Šedek, "Delamination/disbond propagation analysis in adhesively bonded composite joints using guided waves," Journal of Structural Integrity and Maintenance, vol. 7, no. 1, pp. 25–33, Jan. 2022.

[e]   L. Šedková, O. Vích, "Temperature and damage-affected Lamb wave signals in a composite sandwich plate" Proceedings of the 10th European Workshop on Structural Health Monitoring – EWSHM 2022, Palermo, Italy.

[f]   O. Vích, L.Šedková, "Influence of operational and environmental conditions on Lamb wave signals" Proceedings of the 10th European Workshop on Structural Health Monitoring – EWSHM 2022, Palermo, Italy.

List of publications related to the thesis

1.   L. Šedková, V. Vlk, and J. Šedek, "Delamination/disbond propagation analysis in adhesively bonded composite joints using guided waves," Journal of Structural Integrity and Maintenance, vol. 7, no. 1, pp. 25–33, Jan. 2022.

2.   L. Šedková, O. Vích, "Temperature and damage-affected Lamb wave signals in a composite sandwich plate" Proceedings of the 10th European Workshop on Structural Health Monitoring – EWSHM 2022, Palermo, Italy.

3.   O. Vích, L.Šedková, "Influence of operational and environmental conditions on Lamb wave signals" Proceedings of the 10th European Workshop on Structural Health Monitoring – EWSHM 2022, Palermo, Italy.

4.   L. Šedková, J. Šedek, "Defect detectability in composite plates with variable thickness using Lamb waves", the 58th International Scientific Conference on Experimental Stress Analysis (EAN), 2020.

5.   L. Michalcová, "Delamination growth analysis in mode I by means of Lamb waves," Materials Today: Proceedings, vol. 5, no. 13, pp. 26470–26475, 2018.

6.   L. Michalcová, R. Hron, "Quantitative Evaluation of Delamination in Composites Using Lamb Waves," IOP Conference Series: Materials Science and Engineering, vol. 326, p. 012006, Mar. 2018.

7.   L. Michalcová, P. Bělský, P. Kucharský, and L. Rechcígel, "Fatigue disbonding analysis of wide composite panels by means of Lamb waves," Nondestructive Characterization and Monitoring of Advanced Materials, Aerospace, Civil Infrastructure, and Transportation XII, Mar. 2018.

8.   L. Michalcová, Možnosti monitorování kompozitní konstrukce s využitím Lambových vln. Transfer (internal corporate bulletin). 2017.

List of other publications

1. L. Michalcová, M. Kadlec, "Carbon/epoxy composite delamination analysis by acoustic emission method under various environmental conditions," Engineering Failure Analysis, vol. 69, pp. 88–96, Nov. 2016.

2. L. Michalcová, P. Bělský, and L. Petrusová, "Composite panel structural health monitoring and failure analysis under compression using acoustic emission," Journal of Civil Structural Health Monitoring, vol. 8, no. 4, pp. 607–615, Aug. 2018.

3. J. Cagáň, L. Michalcová, "Impact Damage Detection in CFRP Composite via Electrical Resistance Tomography by Means of Statistical Processing," Journal of Nondestructive Evaluation, vol. 39, no. 2, Apr. 2020.

4. J. Cagáň, J. Pelant, M. Kyncl, M. Kadlec, and L. Michalcová, "Damage detection in carbon fiber–reinforced polymer composite via electrical resistance tomography with Gaussian anisotropic regularization," Structural Health Monitoring, vol. 18, no. 5–6, pp. 1698–1710, Dec. 2018.

5. V. Mára, L. Michalcová, M. Kadlec, J. Krčil, and P. Špatenka, "The effect of long-time moisture exposure and low temperatures on mechanical behavior of open-hole Cfrp laminate," Polymer Composites, vol. 42, no. 7, pp. 3603–3618, Apr. 2021.

6. L. Michalcová, M. Kadlec, "Crack Growth Monitoring of CFRP Composites Loaded in Different Environmental Conditions Using Acoustic Emission Method," Procedia Engineering, vol. 114, pp. 86–93, 2015.

7. L. Michalcová, R. Růžek, "Fatigue test of an integrally stiffened panel: Prediction and crack growth monitoring using acoustic emission," Procedia Structural Integrity, vol. 2, pp. 3049–3056, 2016.

8. R. Růžek, L. Michalcová, "Structural health monitoring of a wing panel splice joint using acoustic emission" EWSHM - 8th European Workshop on Structural Health Monitoring, Bilbao, Spain, Jul 2016.

9. J. Šedek, L. Michalcová, "Fatigue crack growth reconstitution in the specimen representing longitudinal joint of an integral panel", the 57th International Scientific Conference on Experimental Stress Analysis (EAN), 2019.

10. V. Mára, J. Krčil, L. Michalcová, and E. Čižmárová, "The Failure of Carbon Fiber Reinforced Composite Analyzed by Acoustic Emission," Defect and Diffusion Forum, vol. 405, pp. 205–211, Nov. 2020.

11. L. Michalcová, "Analýza delaminací v uhlíkových kompozitech za různých zkušebních podmínek metodou akustické emise", *Transfer* (internal corporate bulletin), 2016.

Note: L. Michalcová = L. Šedková